Reconstructing $\bar{\nu}_e$ Energy Spectrum and Ground State Branching Fraction of Laser Trapped ^{92}Rb

by

James Cameron McNeil

B.Sc. Simon Fraser University, 2015

A THESIS SUBMITTED IN PARTIAL FULFILLMENT OF THE
REQUIREMENTS FOR THE DEGREE OF

MASTER OF SCIENCE

in

THE FACULTY OF GRADUATE AND POSTDOCTORAL STUDIES

(Physics)

THE UNIVERSITY OF BRITISH COLUMBIA

(Vancouver)

October 2019

The following individuals certify that they have read, and recommend to the Faculty of Graduate and Postdoctoral Studies for acceptance, the thesis entitled:

Reconstructing $\bar{\nu}_e$ Energy Spectrum and Ground State Branching Fraction of Laser Trapped ^{92}Rb

submitted by James Cameron McNeil in partial fulfillment of the requirements for the degree of MASTER OF SCIENCE in Physics.

Examining Committee:

Dr. John Behr
Supervisor

Dr. Hasinoff
Additional Examiner

Abstract

The anti-electron neutrino $\bar{\nu}_e$ energy spectra from the fission product ^{92}Rb is of interest for reactor neutrino physics and short baseline neutrino oscillation experiments. A study of the beta-neutrino correlation parameter a_1 was performed in laser trapped neutral ^{92}Rb, constraining the strong ground-state to ground-state (GS) first-forbidden $0^- \to 0^+$ rank-0 nuclear matrix element ratio ξ_o/ω. The first-forbidden rank-0 correlation parameter depends non-linearly on beta energy W with $a_1(\xi_o, \omega, W)$ for a decay end-point of W_o. Two distinct analysis were performed via: 1) recoils coincident with atomic shake-off electrons (SOE); and 2) recoils coincident with the beta and atomic SOE. In the former case-1, no distinction can be made between transitions to the GS or excited states and we find the two possible solutions $(\overline{\xi_o/\omega})^{RSOE^+}_{RSOE^-} = ^{+0.437}_{-0.512} \pm \binom{0.005}{0.008}_{stat} \pm \binom{0.01}{0.01}_{sys}$ with $a_1(W \to W_o) \to^{0.30}_{0.36}$, respectively. In the later case-2, however, GS events are isolated through kinematic constraints on the reconstructed transition Q_{exp}-value, with two possible solutions being $(\overline{\xi_o/\omega})^{BRSOE^+}_{BRSOE^-} = ^{+0.541}_{-0.739} \pm \binom{0.008}{0.018}_{stat} \pm \binom{0.01}{0.01}_{sys}$ with $a_1(W \to W_o) \to^{0.50}_{0.58}$, respectively. These are all significantly different from the naively expected $|\xi_o/\omega| \gg 1$, and $a_1(W \to W_o) = 1$. From the beta-recoil 3-momenta, the $\bar{\nu}_e$ energy spectra was also reconstructed for decays through the GS, and eventually compared with theory. We also present our future proposal to measure the GS branching ratio from the reconstructed Q_{exp}-value distribution.

Lay Summary

Event excesses observed in neutrino energy spectra in the 5-7 MeV range from nuclear fission reactors may suggest there is an incomplete understanding of the main β-decaying progeny in this energy range, the dominant of which being ^{92}Rb. In this experiment we directly reconstruct E_ν of ^{92}Rb using energy and momentum conservation from measured momenta of the beta and recoiling daughter. β-decays to the daughter's strong ground state transition are kinematically isolated in total transition energy Q-value to separate β-decays to highly excited states. This ground state isolation enables us to both measure the affiliated E_ν spectra, and perform angular correlation measurements between the beta and neutrino momenta to constrain parameters driving the ground state transition. We also propose measuring the ground state transition branching fraction from the reconstructed experimental Q-value, which are relevant for constraining theoretical predictions in reactor neutrino experiments.

Preface

I, James Cameron McNeil, declare that this thesis titled, "Reconstructing $\bar{\nu}_e$ Energy Spectrum and Ground State Branching Fraction of Laser Trapped ^{92}Rb" and the work presented in it are my own, with the contributions of others detailed in the acknowledgments section. My contribution included developing the analysis code specific to this experiment, development/characterization of the in-vacuum mirrors and position sensitive electron detector, all detector calibrations, conditioning our electrostatic hoops to operate at high-voltage, and led the experiment prior to and during data acquisition.

Contents

List of Tables

List of Figures

List of Abbreviations

p^+	Proton
n^0	Neutron
$\beta^\pm$	Beta electron/positron
$\bar{\nu}_e, \nu_e$	Anti-electron, electron neutrino
DAQ	Data Acquisition System
TOF	Time-Of-Flight
SOE	Shake-Off Electron (atomic)
MCP	Micro-Channel Plate
eMCP	Electron MCP
rMCP	Recoil MCP
rMCP	rMCP hit satisfying DLA timing sum in x and z
DLA	Delay-Line Anode
WSA	Wedge-Strip-Anode
PMT	Photo-Multiplier Tube
UPMT	Upper-PMT(Scintillator)
LPMT	Lower-PMT(Scintillator)
DSSD	Double-Sided Silicon Strip Detector
$E - \Delta E$	Scintillator-DSSD beta telescope detector
GS	Ground State to Ground State Transition
HV	High Voltage

Physical Constants

TDC Dispersion	$\delta t_{TDC} = 0.097\,656\,25\,\text{ns}/\text{ch}$
Speed of Light	$c = 299.792\,458\,\text{mm}/\text{ns}$
$\hbar c$	$\hbar c = 197.326\,963\,1(49)\,\text{MeVfm}$
Fine Structure Constant	$\alpha = 1/137.035\,999\,150(33)$
Electron Rest Mass	$m = 0.510\,998\,910(13)\,\text{MeV}$
Unit Nucleon Rest Mass	$u = 931.494\,095\,4\,\text{MeV}/\text{nucleon}$
^{92}Rb Nucleon number	$A = 92$
^{92}Rb Parent atomic Number	$Z = 37$
^{92}Rb Parent mass Difference	$\Delta M = -74.772\,\text{MeV}$
^{92}Rb Parent mass	$M = \Delta M + uA + mZ = 85.642\,\text{MeV}$
^{92}Sr Daughter atomic number	$Z_r = Z + 1 = 38$
^{92}Sr Daughter mass difference	$\Delta M_r = -82.867\,\text{MeV}$
^{92}Sr Daughter mass (neutral)	$M_r = \Delta M_r + uA + mZ_r = 85.634\,\text{MeV}$
^{92}Sr Daughter RMS-radius	$R_r^{RMS} = 4.2949\,\text{fm}$
^{92}Sr Daughter radius	$R_r = \sqrt{5/3}R_{RMS} = 5.5447\,\text{fm}$
Q-value	$Q = \Delta M - \Delta M_r = 8.095\,\text{MeV}$
Beta End-point	$E_o = Q + m = 8.606\,\text{MeV}$

List of Symbols

f	Lepton phase space integral	a.u.
ft	Phase-space corrected lifetime	s
g_V	Vector coupling constant	a.u.
g_A	Axial-vector coupling constant	a.u.
B_F	Fermi strength function	a.u.
B_{GT}	Gamow-Teller strength function	a.u.
I	Nuclear spin	$\hbar\omega$
$I_{i/f}$	Initial/final nuclear spin	$\hbar\omega$
τ	Iso-spin operator	a.u.
$T_{i/f}$	Initial/final iso-spin	a.u.
π	Parity: spatial transformation operation $\vec{x} \rightarrow -\vec{x}$	a.u.
I_β	Beta transition intensity	a.u.
S_β	Beta transition strength	a.u.
E_f	Daughter excited state energy	MeV
E_β	Beta total energy ($W = E_\beta/m$, $W_o = E_o/m$)	MeV
E_ν	Neutrino energy	MeV
p_β	Beta momentum	MeV/c
p_ν	Neutrino momentum	MeV/c
p_r	Recoil momentum	MeV/c
K_r	Recoil kinetic energy	eV
ϕ_r	Recoil azimuthal angle (w.r.t +x-axis in xz-plane)	rads.
θ_r	Recoil angle (w.r.t +y-axis)	rads.
$a_{\beta\nu}$	$\beta - \nu$ correlation parameter	a.u.
θ	$\beta - \nu$ momenta angle	rads.
Ω_θ	$\beta - \nu$ solid-angle	a.u.
F_*, F	Uncorrected,corrected Fermi Function	a.u.
R	Finite recoil mass correction	a.u.
L_o	Finite recoil volume correction	a.u.
C	Beta-recoil phase-space convolution correction	a.u.

$\mathcal{M}$	Degree of transition forbiddenness	a.u.
$\mathcal{R}$	First-forbidden transition rank	a.u.
ξ_o	Time-like rank-0 first-forbidden nuclear matrix element	a.u.
ω	Space-like rank-0 first-forbidden nuclear matrix element	a.u.
$NORM$	Arbitrary normalization of theory to data	a.u.
ϵ_m	Simulated mask transmission efficiency function	a.u.
ϵ_{fd}	Simulated finite recoil event density function	a.u.
ϵ_{LR}	Left/Right rMCP efficiency function	a.u.
ϵ_{UD}	Up/Down rMCP efficiency function	a.u.
I_{Rnd}^{Bck}	Time-random(TOF) background distribution	counts
I_{Hoop}^{Bck}	HV Hoop background distribution	counts
+2, 3, 4	All respective recoil charge states	a.u.
+2, 3, 4	Respective TOF-bounded recoil charge states	a.u.

Acknowledgements

Chapter 1

Introduction

In reactor neutrino osculation experiments two anomalies are observed: 1) a 6% deficit in anti-electron neutrino $\bar{\nu}_e$ flux, and 2) a bump-like excess in 5-7 MeV $\bar{\nu}_e$-energy range of nearly 10% [1] at multiple short-baseline experiments including Daya Bay[2], Reno [3], and Double Chooz [4]. The model's fit were β^--conversion Huber model[5], but this excess was also observed in the Mueller Model[6]. These β^--conversion models are known to have some shortcomings such as the forbidden shape corrections often not incorporated despite the significant fraction of neutrinos in the 5-7 MeV energy range being from several first-forbidden non-unique decays [1]. The shape corrections are largely unconstrained as many of the nuclear matrix elements governing the forbidden transitions are experimentally unconstrained. The role of forbidden transitions was revisited by Hayen who attempted to parametrize them with shell-model calculations from the dominant contributors, and this has reduced the significance of the bump feature in the $\bar{\nu}_e$ spectra[7]. The flux deficit may suggest an eV scale sterile neutrino that the known standard model $\bar{\nu}_e$ mix with, while the bump like feature may result from an incorrect/incomplete model of the reactor fuel/cycle. Unconstrained systematics from missing data, biased branching fractions (Pandemonium Effect), or forbidden transition beta shape corrections may each contribute to this model disagreement[1].

A limited set of first-forbidden ground-state to ground-state (GS) transitions with large Q-values have dominant contributions to the $\bar{\nu}_e$ spectral shape in the 5-7 MeV range (^{96}Y,^{92}Rb, ^{142}Cs, ^{97}Y, ^{93}Rb, ^{100}Nb, ^{140}Cs, ^{95}Sr) collectively accounting for 48% of the total $\bar{\nu}_e$ flux in this energy range [1]. Estimates of ^{92}Rb first-forbidden $0^- \rightarrow 0^+$ GS transition alone contributes conservatively up to 16% of the total flux in this energy range, driven by comparatively small

$\log(ft) = 5.75$ assuming a GS branching of 95% (2012 Nuclear Data Sheet). Total absorption spectrometer experiments performed with ^{92}Rb have consistently yielded smaller GS branching fractions of 91(3)%[8],[9], which would slightly reduce its contribution to the $\bar{\nu}_e$ excess on the order of a few percent[1] within this energy range. Accurate and independent determination of the GS branching fraction is thus important to correctly constrain the expected population of high energy $\bar{\nu}_e$ neutrinos, particularly in the case of ^{92}Rb. On the order of 1100 other beta decays contribute at the sub-percent levels ($< 2\%$) and do not significantly impact the spectrum shape in the $5 - 7$ MeV region.

In the case of ^{92}Rb a continuum of highly excited states is believed to be fed on the tail of a Giant resonance with very low transition intensities making direct GS branching ratio extremely challenging to measure. Total absorption spectrometers use high-Z scintillators, unlike conventional Ge detectors, and thus nearly completely absorb the gamma-ray energy within the detector volume, but they suffer from known systematic uncertainties. Amongst the systematics are: 1) "inner" bremsstrahlung, in which photons are radiated during the decay of the nuclei; and 2) "outer" bremsstrahlung, in which the photons are radiated by the beta interacting with detector material. In our experiment described below the gamma-ray photons from excited states and bremsstrahlung are not detected, but they are inferred from missing transition energy with respect to the strong GS beta transition energy (Q-value). We will rely on simulations to constrain the missing energy distribution from bremsstrahlung photons, in order to separate the population resulting from transitions to excited states in the data, which will be necessary for GS branching measurement in the final analysis.

The reality of short-baseline neutrino oscillation experiments coupled with power reactors is that they often utilize a mix of fuel ^{235}U, ^{238}U, ^{239}Pu, and ^{241}Pu, complicating the analysis of the fission progeny beta decay chains contributing to the $\bar{\nu}_e$ flux. A more significant problem for the power reactor experiments is that the relative proportion of these fuels is generally assumed to be constant over the fuel cycle, which need not be true in general, and would be extremely difficult to measure directly. A great deal of recent experimental progress has been made in understanding the time dependent antineutrino flux from the dominant ^{235}U, and ^{239}Pu fuels by the RENO collaboration [10]. The above model

deviations and experimental challenges have motivated the PROSPECT reactor $\bar{\nu}_e$ experiment. PROSPECT is designed to both search for extremely short baseline ($\sim$ 7.9 m) neutrino oscillations [11] expected assuming eV scale sterile neutrino, as well as utilize the highly enriched ^{235}U research reactor core at Oakridge National Lab for precision studies of $\bar{\nu}_e$ spectra [12]. With limited statistics PROSPECTs $\bar{\nu}_e$ spectra are in good agreement with both the Huber model and Daya-Bay excess observed in the 5-7 MeV range [12].

Given the importance of constraining ^{92}Rb GS branching, we developed a complementary method utilizing direct Q-value measurements through momentum resolved coincident beta-recoil kinematics. The TRINAT neutral atom trap at TRIUMF is employed to cool and confine ^{92}Rb using a Magneto-Optic-Trap (MOT), complete with recoil ion Time-Of-Flight (TOF) spectrometer, and opposing $E - \Delta E$ beta detectors. About 100k ^{92}Rb atoms are nominally trapped at mK temperatures within $1mm^3$ to provide a backing free, zero momentum initial state. We will show below that the strong first-forbidden $0^- \rightarrow 0^+$ GS branching yields a large Q-value resonance at 8.1 MeV, with a low energy tail resulting from transitions to excited states. In the weak decay of a $0 \rightarrow 0$ transition, the outgoing beta and neutrino momenta (angularly displaced by θ) are angularly constrained by a $\cos\theta$ dependence, weighted by an angular correlation parameter $a_{\beta\nu}$, and can be extracted from the recoil kinetic energy (K_r) spectrum. In the first forbidden rank-0 GS transition, $a_{\beta\nu}$ acquires a beta energy dependence, and a dependence on the two nuclear matrix elements ξ_o, ω mediating the decay. With the GS events kinematically isolated in transition Q-value, direct measurement of the ratio ξ_o/ω is performed via $a_{\beta\nu}$ where we find $|\xi_o/\omega| < 1$, and $a_{\beta\nu} \neq 1$. The 3-body decay kinematics and constrained beta-recoil momenta also enable direct reconstruction of the GS $\bar{\nu}_e$ energy spectra for eventual comparison with theoretical predictions.

The thesis below is organized sequentially beginning with relevant theory, followed by experimental sections detailing the setup, and detector calibrations. The experimental results section details our analysis of the $a_{\beta\nu}$ parameter in recoil atomic shake-off electron coincidence (Recoil-SOE), and triple coincident analysis (Recoil-SOE-Scintillator) for multiple recoil charge states. We detail our evaluation of the Q-value, GS rank-0 nuclear matrix element ratio ξ_o/ω, and reconstructed $\bar{\nu}_e$ spectra. We conclude with a comparison between the $a_{\beta\nu}$ with, and without GS isolation.

Chapter 2

Theory

2.1 Nuclear Beta decay

In nuclear $\beta^{\pm}$-decay, the weak force mediates the semi-leptonic decay of valence quarks (u, d) contained in protons (uud) and neutrons (udd) within atomic nuclei through the virtual $W^{\pm}$ vector-boson, where $u, d \rightarrow d, u$, respectively such that

$$
\begin{aligned}
p^+ &\rightarrow n^0 + \beta^+ + \nu_e, \\
n^0 &\rightarrow p^+ + \beta^- + \bar{\nu}_e.
\end{aligned}
\tag{2.1}
$$

The charged weak interaction currents mediating the decay have been experimentally determined to be Vector and Axial-Vector (V-A) [13]. If $|\psi_i\rangle$ and $|\psi_f\rangle$ are the initial and final nuclear wave-functions then the vector component of the decay is parameterized by the Fermi strength function $B_F = |\langle \psi_f | \tau | \psi_i \rangle|^2$ where τ is the isospin transformation matrix $(p \leftrightarrow n)$, while the axial-vector current is encoded in the Gamow-Teller (GT) strength function $B_{GT} = |\langle \psi_f | \sigma\tau | \psi_i \rangle|^2$ where σ is the Pauli spin matrix. In a pure Fermi transitions, the change in nuclear spin(I)/parity(π) satisfy ($\Delta I = 0/\Delta\pi = 0$ with $I_i = I_f = 0$), while the pure GT transition encodes the spin/parity dependent transitions ($\Delta I = 0, \pm 1/\Delta\pi = 0, +1$ no $0 \rightarrow 0$). The lepton phase-space (f) rapidly increases with available energy in the decay, while the transition lifetime (t) decreases, making the phase space corrected lifetime ft-value a value of comparison between differing nuclear transitions. The beta phase-space is also perturbed by the coulomb interaction with the nuclear system impacting transition lifetimes and will be discussed further below. If $M_{fi} = \langle \psi_f | M | \psi_i \rangle$ is the general transition matrix element, then the transition strength $|M_{fi}|^2 \propto g_V^2 B_F + g_A^2 B_{GT}$ and will scale inversely with the transition ft-value with a larger strength corresponding to smaller ft-value, and vice-versa such that

$$
ft = \frac{2 \ln 2 \pi^3 \hbar^7}{m^5 c^4} \cdot \frac{1}{g_V^2 B_F + g_A^2 B_{GT}}.
\tag{2.2}
$$

The above holds for *allowed* transitions where there is no change in the nuclear parity in the initial and final states. In *forbidden* transitions, however, nuclear parity transformation is permitted where the Fermi and GT operators are scaled by operators which transform under parity, and this will be discussed below.

2.2 ^{92}Rb Level Scheme

The tabulated level scheme of ^{92}Rb from 2012 Nuclear Data Sheet is illustrated in Figure(2.1), demonstrating strong first-forbidden ground state $0^- \rightarrow 0^+$ feeding, along with several weak branchings to excited state transitions. The excited state Gamow-Teller (GT) transitions $(0^- \rightarrow 1^-)$ along with additional excited states not listed aid in diluting GS decay strength.

^{92}Rb Q = 8.104 MeV

0^- $\tau_{1/2} = 4.48\,s$

	BR(%)	BR(%)	log(ft)
1^-	0.26		3.97
1^-	0.47 / 0.17		6.02 / 8.13
1 / 1	0.33	0.22	6.49 / 6.55
$2^{(+),1}$ / 0^+	0.31	0.54	7.15 / 9.39
2^+ / 0^+ / 2^+	0.141		7.95 / 10.19
2^+	0.11	0.43	9.77
2^+	1.00		9.63
0^+		95.2	5.751
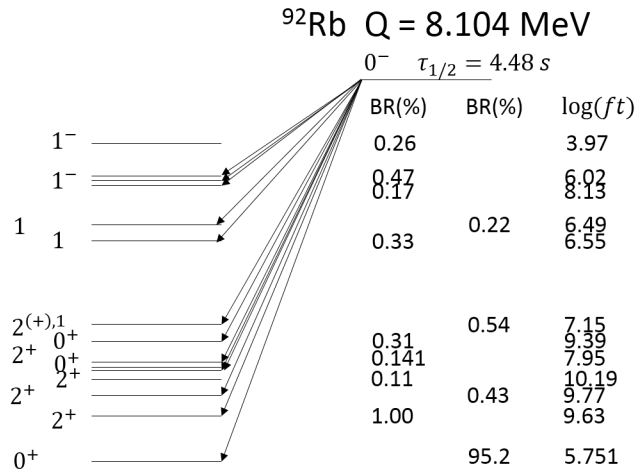
Figure 2.1: ^{92}Rb level scheme (Compiled 2012 Nuclear Data Sheet)

In the ^{92}Rb beta-decay a continuum of excited states are believed to be fed in the ^{92}Sr daughter of energy E_f above the GS on the tail of a so-called giant resonance. Giant multi-pole resonances result from collective coherent-motion of nucleons often within excited, or deformed nuclei. One example is the giant dipole resonance resulting from collective uni-axial oscillations of protons with respect to the neutron population. A toy model of a beta-transition strength $S_\beta(E_\beta)$ function is shown in Figure(2.2a), with the giant resonance largely above the Q-value. The low energy tail of the resonance, however, has states which leak into the energetically allowed region ($E_f < Q$) and are fed through beta-decay. If the level density of the daughter's excited states is sufficiently low

between E_f and $E_f + \Delta E$, then for the given transition ft-value the beta transition intensity $I_\beta(E_f)$ satisfy

$$f(Q - E_f, Z_r) \cdot T_{1/2}/ft = I_\beta(E_f) \tag{2.3}$$

where $T_{1/2}$ is the parent lifetime, and $f(Q_\beta - E_f, Z_r)$ the beta phase-space integral [14]. The beta phase-space integral f with transition end-point $W_o = Q/m$

$$f(Q - E_f, Z_r) = \int_1^{(Q-E_f)/m} F(W, Z_r)W\sqrt{W^2 - 1}(W_o - W)^2 dW \tag{2.4}$$

encodes the phase-space accessible to the beta of energy $W = E_\beta/m$ along with the modification to the beta wave-functions through the Coulomb interaction with the daughter's (Z_r) charged nuclear wave-functions via the Fermi function $F(W, Z_r)$ (detailed below). In ^{92}Rb, the total absorption experiments mentioned above report a smaller GS branching of 91 % than that reported in the tabulated levels (95 %), reducing the GS beta transition intensity $I_\beta(E_f = 0)$. Since the GS ft-value scales inversely with $I_\beta(E_f)$, the $\log ft$ should correspondingly increase by $\log(0.95/0.91) = 0.04$ to that reported in in Figure(2.1).

However, when the level density of the daughter's excited states is large then an average beta transition intensity is sampled between E_f and $E_f + \Delta E_f$ with the average beta transition strength $S_\beta(E_x)$ for E_x on this interval satisfying

$$S_\beta(E_x)f(Q - E_x, Z_r) \cdot T_{1/2} = \sum_{E_f \in \Delta E} I_\beta(E_f)/\Delta E. \tag{2.5}$$

As shown in Figure(2.2c) the phase-space integral can either enhance, or suppress excited state transition intensities relative to the low-lying states by equation(2.5) in $\beta^\pm$-decay, respectively. In the case of β^--decay, even with the suppression of excited state transition intensity, there can still be considerable decay strength to such states. The result is a dense continuum of highly excited states with very low transition intensity which often have complicated γ-decay feeding to lower-lying states. Since these initial excited states are weakly populated and feed multiple low lying states, it becomes increasingly difficult to resolve such transitions directly, making absolute branching fractions difficult to constrain. Total γ-absorption experiments sacrifice γ-energy resolution from large detector volumes with the goal of collecting all the photon energy from which branching fractions can be extracted.
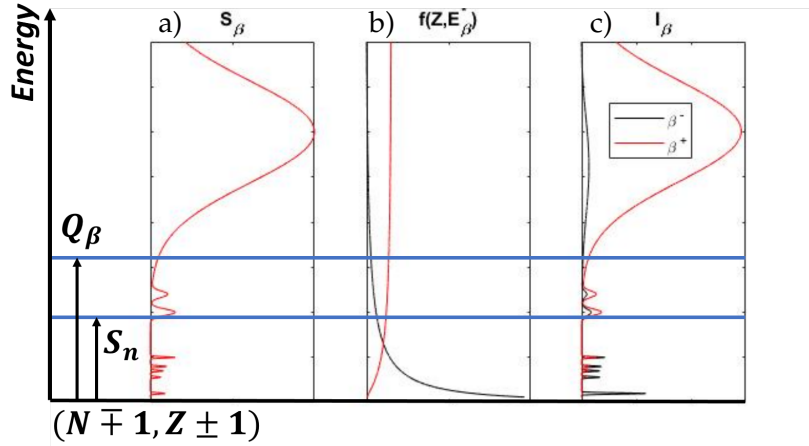
Figure 2.2: Toy model of a Giant-Resonance where a continuum of highly excited and fragmented states become accessible via β-decay with beta a) transition strength function $S_\beta(E_x)$, b) phase-space function $f(Q - E_x, Z_r)$, and c) transition intensity $I_\beta(E_f)$.

In ^{92}Rb one consequence of both the large beta-decay $Q = 8.1$ MeV and, likely, the daughter's dense excited state level-set above the neutron separation energy of $S_n = 7.287$ MeV, is the opening up of prompt beta-delayed neutron emission channels. In principle such events could distort the low energy recoil kinetic energy K_r spectrum by driving events to larger K_r, although that requires scintillator thresholds to be made sufficiently small to accept the correspondingly low energy beta's from the ^{92}Rb parent decay. Significant efforts were undertaken to lower our beta detection thresholds to increase our sensitivity to the highest energy neutrinos by reducing the thickness and Z of our in-vacuum mirrors which the beta's must penetrate prior to detection; these effects will be detailed below.

2.3 Recoil Kinematics & Angular Correlation $a_{\beta\nu}$

In the beta decay of nuclei of mass M, the 3-body final state yields energetic beta (mass m), ν-neutrino, and low energy recoiling daughter (mass M_r). The 4-momentum vectors of the β, ν, and recoil are defined by $(E_\beta, \vec{p}_\beta)$, $(E_\nu, \vec{p}_\nu)$, and $(K + M_r, \vec{p}_r)$ for the recoil of kinetic energy K_r, respectively. In the weak decay parity violation is maximal at the lepton vertex ensuring only chiral-left handed neutrinos, or chiral-right handed anti-electron neutrinos are produced in $\beta^\pm$-decay, respectively. The consequence of such helicity constraints on the outgoing neutrino produce the angular correlation (angle θ) between the beta and the neutrino 3-momenta. In the nuclear spin-0 system ($I_f = I_i = 0$), the

probability of a beta with energy between $[E_\beta, E_\beta + \delta E_\beta]$ and within $[\theta, \theta + \delta\theta]$ is $dN = P(E_\beta, \theta)dE_\beta d\Omega_\theta$ such that

$$dN = F(E_\beta/m, Z_r, R_r)p_\beta E_\beta p_\nu^2 \left[1 + a_{\beta\nu}\left(\frac{p_\beta}{E_\beta}\right)\cos\theta\right]dE_\beta d\Omega_\theta \qquad (2.6)$$

with $F(E_\beta/m, Z_r, R_r)$ a modifying Fermi function (detailed below), Ω_θ the unit solid angle of the beta-neutrino angular phase-space, and $a_{\beta\nu}$ the beta-neutrino correlation parameter. From momentum conservation $p_r^2 = (\vec{p}_\beta + \vec{p}_\nu)^2$

$$[p_r^2 - (p_\beta^2 + p_\nu^2)]/2 = p_\beta p_\nu \cos\theta \qquad (2.7)$$

where after differentiating both sides it follows that $p_\beta p_\nu d\Omega_\theta = p_r dp_r$. If E_o is the beta end-point energy and Q the transition kinetic energy available to the beta then $E_o = Q + m = E_\beta + E_\nu + K_r$. Since the recoil $K_r \ll E_\beta, E_\nu$ then $E_o - E_\beta \cong E_\nu \cong p_\nu$ where the last equality assumes negligible neutrino mass. Given the recoil is non-relativistic with the recoil $K_r = p_r^2/2M_r$, it follows that $M_r dK_r = p_r dp_r$. After substitution of the above into equation(2.6) we find the recoil K distribution[15]

$$\frac{dN}{dK_r} = \int_{m_e}^{E_o} dE_\beta \frac{M_r}{2} F(Z_r, E_\beta/m, R_r)\cdot$$
$$\cdot \left[E_\beta(E_o - E_\beta) + \frac{a_{\beta\nu}}{2}(2M_r \cdot K_r + m^2 - E_\beta^2 - (E_o - E_\beta)^2)\right]. \qquad (2.8)$$

The recoil K spectrum has a linear dependence on K_r, up to a modifying E_β dependent Fermi function $F(E_\beta/m, Z_r, R_r)$ from the beta wave function interacting with the nuclear environment. One of the most basic Fermi functions $F_*(W, Z_r, R_r)$ for β^--decay is given by

$$F_*(W, Z_r, R_r) = 2(\gamma + 1)(2p_\beta R_r)^{2(\gamma-1)}e^{\pi\alpha Z_r W p_\beta}\frac{|\Gamma(\gamma + i\alpha Z_r W p_\beta)|^2}{|\Gamma(1 + 2\gamma)|^2} \qquad (2.9)$$

with $\gamma = \sqrt{1 - (\alpha Z_r)^2}$. The Fermi-function F_* parameterizes solutions to the Dirac equation for the outgoing beta wave-function at finite recoil radius R_r, where solutions are non-divergent. Corrections to the outgoing beta wave-function must be applied as it interacts with the nuclear wave-functions requiring recoil mass correction $R(W, Z_r, M_r)$, finite nuclear volume correction $L_o(W, Z_r)$, and phase-space convolution correction $C(W, Z_r)$ with modified Fermi function given by

$$F(W, Z_r, R_r) = F_*(W, Z_r, R_r) \cdot R(W, Z_r, M_r) \cdot L_o(W, Z_r) \cdot C(W, Z_r). \qquad (2.10)$$
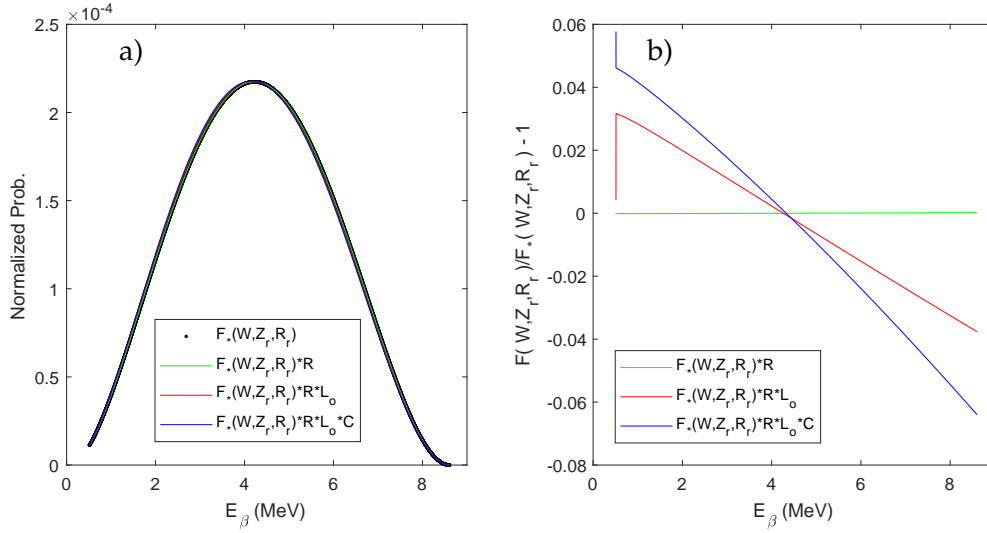
Figure 2.3: (left) ^{92}Rb allowed β spectrum with fractional corrections (right) to the Fermi-function from higher order corrections R_o, L_o, C_A.

The parameters R, L_o, C have unique dependencies depending on whether the vector or axial-current mediate the nuclear transition, as outlined by Wilkinson [16]. Warburton [17] pointed out that in a $0^- \rightarrow 0^+$ decay the two operators, γ^5 (time-like), and $\sigma \cdot r$ (space-like) drive the axial-current of the decay, thereby requiring the axial-current parameterization of R, L_o, C in equation(2.10) to be applied in this analysis. The corresponding beta energy spectrum parameterized by the phase space differential df/dW above in equation(2.4) for the ^{92}Rb GS decay is shown in Figure(2.3a), with the sequentially implemented corrections to the basic Fermi function F_* above overlaid. The fractional correction of each successive component modifying the Fermi function in equation(2.10) is shown in Figure(2.3b), demonstrating energy dependent corrections which are maximally of order 5%. The modifications to F_* in applying these corrections drive beta decay intensity to lower E_β as the outgoing beta wave-function exchanges momenta with the nuclear volume.

2.4 Forbidden Transitions

2.4.1 Correlation Parameter

It was shown above that the matrix element mediating the allowed axial-current in the weak decay was $\sigma\tau$. In first-forbidden decays, the hadronic and leptonic currents are further modified from the allowed theory by additional transition operators including

$$r, [r, \sigma]^{\mathcal{R}}, \quad \mathcal{R} = 0, 1, 2 \tag{2.11}$$

from the leptonic weak currents acquiring spatial dependencies and,

$$\gamma^5, \alpha \tag{2.12}$$

from the hadronic weak currents[18]. Computing the matrix elements in forbidden transitions is much more difficult compared to the allowed transitions, which only depend on spin/isospin, as they now acquire a dependence on the radial wave-functions of the nuclear system; particularly for systems with large radii and Z. We will closely follow the notation of Warburton[17][18]. In this formulation nuclear spin I and isospin T are considered to be good quantum numbers with initial and final nuclear wave-functions $|I_i, T_i\rangle$ and $|I_f, T_f\rangle$. The tensor rank $\mathcal{R}$ accessible to the forbidden transitions are integer values between

$$|I_f - I_i| \leq \mathcal{R} \leq |I_f + I_i|. \tag{2.13}$$

In introducing the above transition operators, the phase space accessible to the outgoing leptons in the allowed decay of equation(2.4) is modified by powers of $(p/W)^{\mathcal{M}}$ where $\mathcal{M}$ is the degree of forbiddenness of the transition. Re-expressing the *allowed* form of dN in equation(2.6) where if df is the lepton phase-space unit element

$$df = F(W, Z_r, R_r) p_\beta W (W_o - W)^2 dW \tag{2.14}$$

and $C_o(W, \theta)$ the lepton phase-space convolution function

$$C_o(W, \theta) = 1 + a_{\beta\nu} \left(\frac{p_\beta}{W} \right) \cos\theta, \quad then \tag{2.15}$$

$$dN = df \cdot C_o(W, \theta) d\Omega_\theta \tag{2.16}$$

Warburton[17] proposed to expand the lepton phase-space convolution function $C_o(W, \theta) \rightarrow C'_o(W, \theta)$ in powers of $(p/W)^{\mathcal{N}}$ for $\mathcal{N} = 0, 1, 2$ with $C'_o(W, \theta)$ satisfying

$$\left[\sum_{\mathcal{M}, \mathcal{N}, \mathcal{R}} K(\mathcal{M}\mathcal{N}\mathcal{R}) W^{\mathcal{M}} \left(\frac{p_\beta}{W} \right)^{\mathcal{N}} P_{\mathcal{N}}(\theta) \right] \Big/ \left[\sum_{\mathcal{M}, \mathcal{R}} K(\mathcal{M}0\mathcal{R}) W^{\mathcal{M}} \right]. \tag{2.17}$$

Here $P_{\mathcal{N}}(\theta)$ is the $\mathcal{N}$th order Legendre polynomial, and $K(\mathcal{M}\mathcal{N}\mathcal{R})$ independent of W with a more general form in [17] ($A \sim 40$) following Behrens &

Buhring formalism[19]. The formalism for small Z is presented in [18] specifically for the first-forbidden beta-neutrino correlations in ^{11}Be. Important in this first-forbidden formalism is the linearity in rank-$\mathcal{R}$ of the transition with nuclear matrix elements only interfering within their rank, and not outside their rank. We restrict discussion to $\mathcal{N} = 0, 1$ contributing to the leading order terms in equation(2.17)

$$\frac{\sum_{\mathcal{M},\mathcal{R}} K(\mathcal{M}0\mathcal{R})W^{\mathcal{M}} + \sum_{\mathcal{M},\mathcal{R}} K(\mathcal{M}1\mathcal{R})W^{\mathcal{M}} \left(\frac{p_\beta}{W}\right)\cos(\theta)}{\sum_{\mathcal{M},\mathcal{R}} K(\mathcal{M}0\mathcal{R})W^{\mathcal{M}}}$$

which reduces to the familiar convolution expression

$$C_o'(W,\theta) = 1 + a_1(W)\left(\frac{p_\beta}{W}\right)\cos(\theta). \tag{2.18}$$

The distinction from $a_{\beta\nu}$ in the allowed decay is the forbidden correlation parameter $a_1(W)$ acquires an energy dependence where [17][18]

$$a_1(W) = \frac{\sum_{\mathcal{M},\mathcal{R}} K(\mathcal{M}1\mathcal{R})W^{\mathcal{M}}}{\sum_{\mathcal{M},\mathcal{R}} K(\mathcal{M}0\mathcal{R})W^{\mathcal{M}}}. \tag{2.19}$$

Further restricting our discussion to the ^{92}Rb first-forbidden $0^- \rightarrow 0^+$ rank $\mathcal{R} = 0$ transition the requisite coefficients $K(\mathcal{M}\mathcal{N}0)$ are

$$(\mathcal{N} = 0): K(000) = \xi_o^2 + \frac{1}{9}\omega^2, \quad K(-100) = -\frac{2}{3}\mu_1\gamma_1 \cdot \xi_o\omega \tag{2.20}$$

$$(\mathcal{N} = 1): K(010) = \xi_o^2 - \frac{1}{9}\omega^2 \tag{2.21}$$

where $\gamma_1 = \sqrt{1 - (\alpha Z_r)^2}$ with α the fine structure constant and $\mu_1 = \lambda_1 = 1$ [19]. Expanding equation(2.19) and normalizing with respect to ω

$$a_1(W,\xi_o,\omega) = \frac{\left(\left(\frac{\xi_o}{\omega}\right)^2 - \frac{1}{9}\right)}{\left(\left(\frac{\xi_o}{\omega}\right)^2 + \frac{1}{9}\right) - \frac{2}{3}\left(\frac{\xi_o}{\omega}\right) \cdot \frac{\gamma_1}{W}}. \tag{2.22}$$

Naively if either of the matrix elements are small then $a_1 = 1$, which cannot be assumed in ^{92}Rb. Inserting equation(2.22) into the recoil K_r spectrum in equation(2.8) one can perform a two parameter fit to the experimental spectrum floating the nuclear matrix element ratio ξ_o/ω and arbitrary normalization *NORM*. The nuclear matrix elements of interest theoretically encoding the rank $\mathcal{R} = 0$ axial-current can be broken into the time-like M_o^T, and space-like M_o^S components where their relation to ξ_o, and ω satisfy

$$\xi_o = (M_o^T + \xi M_o^{S'}) + \frac{1}{3} M_o^S W_o, \qquad M_o^T \propto \left\langle I_f, T_f | \gamma^5 \tau | I_i, T_i \right\rangle, \tag{2.23}$$

$$\omega = M_o^S \propto \left\langle I_f, T_f | \boldsymbol{\sigma} \cdot \boldsymbol{r} \tau | I_i, T_i \right\rangle. \tag{2.24}$$

Here $\xi = \alpha Z / 2 R_r$ and $M_o^{S'} = \epsilon_o^{S'} M_o^S$ where $\epsilon_o^{S'} \cong 0.7$ but can be determined from integrating radial wave-functions weighted by $(2/3) I(1, 1, 1, 1, r)$ as per [19]. It follows that the time-like to space-like matrix element ration is linear in ξ_o / ω with

$$\frac{M_o^T}{M_o^S} = \frac{\xi_o}{\omega} - \left(\xi \epsilon_o^{S'} + \frac{1}{3} W_o \right). \tag{2.25}$$

2.4.2 More information about 0^- to 0^+ transitions, particularly ^{92}Rb

Spectrum shape

In the parameterization used by Ref.[20], the two main operators contributing to $0^- \to 0^+$ transitions have different β energy spectra, hence different ν spectra. One operator has an allowed spectrum, while the other is multiplied by the shape factor

$$C(E_\beta) = p_\beta^2 + E_\nu^2 + 2(p_\beta / E_\beta)^2 E_\nu E_\beta, \tag{2.26}$$

which would make fewer high-energy neutrinos by about 5% if it dominated the transition. We are finding it very hard to make the correspondence between the notations to let us contrain this particular linear combination of operators from the $\beta - \nu$ correlation, which would be simpler than trying to fit the E_β spectrum. Nevertheless, this has been a strong motivation for us to independently measure the ν spectrum.

The "ξ approximation" doesn't work

A review by Hayes and Vogel [21] has much useful information about forbidden beta decay and reactor neutrinos. For the high β Q-values of interest, a useful approximation does not hold. The "ξ approximation" asserts that the β energy spectra are close to allowed if the Coulomb energy of the emitted β is much larger than its total energy at the nuclear radius, $\alpha Z / R \gg E_0 / m$. In ^{92}Rb decay $\alpha Z / R = 19.2$ while $E_0 = 16.8 m_\beta$, so this inequality does not hold at all. It's still notable that the measured β energy spectrum for ^{92}Rb decay has close to an allowed shape [22] within the accuracy of the measurement.

Chapter 3

Experiment

3.1 TRIUMF-ISAC
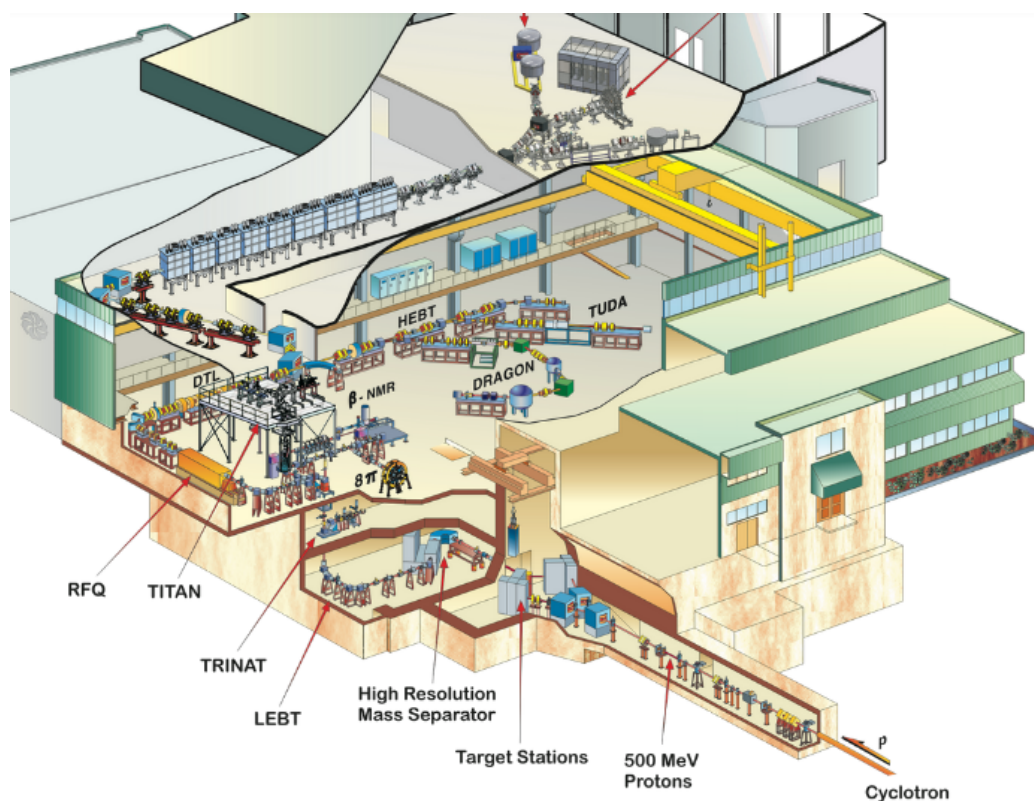
Figure 3.1: Isotope Separator and Accelerator facility as of 2003 at TRIUMF (see ISAC). The main cyclotron is off to the page towards bottom-right of the image. The TRINAT experiment is correctly indicated above the ISAC pre-separator room (LEBT).

The main cyclotron at TRIUMF supplies a 500 MeV proton beam with a 9.8 μA beam current incident on a uranium carbide (UCx) target within the ISAC target modules [23]. With the proton beam on target, the uranium undergoes nuclear spallation producing many secondary daughter species, most of which are unstable, decaying through either α, β, γ-decay, proton/neutron emission,

or electron capture processes. Progeny diffuse from the hot bulk target material and effuse through a hot cylindrical "ionizer" lined with rhenium, a metal with a high work function. Alkali progeny in particular leave their valence electron at the ionizer metal surface, so are "surface ionized" and then extracted with an applied electric potential. The extracted beam is then purified with a magnetic spectrometer separating species in A/q to select for ^{92}Rb prior to delivery to the TRINAT experiment.

It should be noted during our original 2017 test run the magnetic spectrometer was run with slits-in for improved beam purity, but this led to unstable beam due to electrostatic charging from the high particle flux of 10^8/sec produced from the ISAC targets. The TRINAT experiment selectively traps only ^{92}Rb and so isotopic purity is not a significant constraint. Consequently, these slits were retracted in the subsequent 2018 run yielding a largely stable supply of radioactive beam for the data presented in this thesis.

3.2 TRINAT
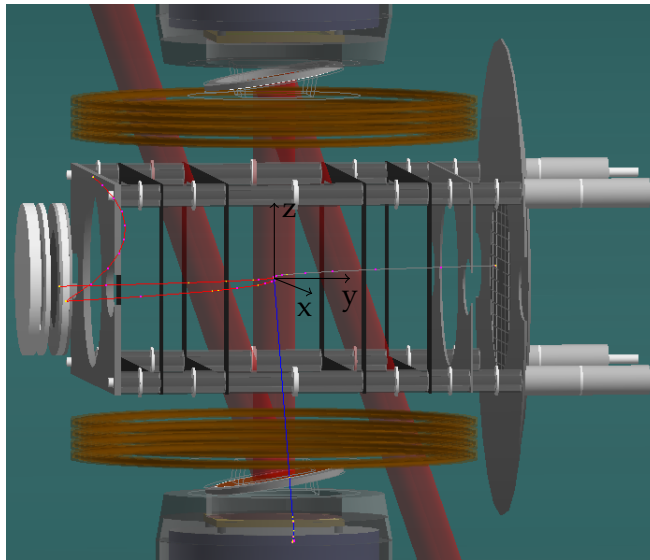
Figure 3.2: TRIUMF Neutral Atom Trap (TRINAT) with electrostatic hoops for recoil charge state separation with opposing recoil-ion (rMCP) and shake-off electron (SOE) detectors, and orthogonally orientated, symmetric $E - \Delta E$ β-telescopes along the vertical $\pm z$-axis. The vertical trapping beam path is indicated in red reflected from 70 nm thin gold mirrors backed by 4 μm Kapton. (Horizontal trapping beams are not shown). ^{92}Rb is trapped in a Magneto-Optic-Trap (MOT) at the center of the apparatus where it β-decays with outgoing tracks of the β^- (blue), recoiling ^{92}Sr daughter (grey), and atomic SOE (red) shown.

The TRINAT experiment consists of two adjacent Magneto-Optic-Traps (MOT), the first within the collection chamber, and the second within the experimental chamber. Ion beams from the ISAC targets typically are delivered at 15-20 keV incident on an Zirconium neutralizing foil. The foil is heated to just above a phase transition in the lattice structure to optimize release from the neutralizer [24]. The neutral ^{92}Rb then diffuses out into the vacuum and thermalize on a glass cell with special polymer coating to aid in cooling the atoms before trapping. The thermalized neutral ^{92}Rb atoms are collected in the collection MOT prior to transfer to the experimental chamber. A resonantly detuned push beam is then used to transport the atoms from the collection trap to the measurement trap at the center of the experimental chamber as shown in Figure(3.2) where they subsequently decay [25]. The TRINAT experimental chamber consists of rectangular electrostatic hoops for recoil ion charge-state separation by time-of-flight(TOF) along the $+y$-axis, with opposing recoil ion detector (rMCP) and shake-off-electron (SOE-eMCP) detectors. These detectors are microchannel plate (MCP) based analog amplifiers for single ion/electron event triggering with ∼ns timing resolution. Position sensitive delay-line-anode (DLA), and wedge-and-strip detectors (WSA) back the rMCP, and eMCP, respectively.

Two opposing symmetric $E - \Delta E$ β-telescopes along the $\pm z$-axis face the trap. Each β-telescope consists of a trap-facing (ΔE) Double-sided Silicon Strip Detector (DSSD) backed by a plastic (E) scintillator. The β-telescopes are separated from the vacuum by a thin 229 *um* Be foil. The vertical trapping beams of the MOT are necessarily brought in at 19° from the $\pm z$-axis and reflected along the $\pm z$-axis via high-reflectivity (93 %) pellicle mirrors mounted at 9.5° to normal incidence on the trap facing side of the Be foils within the vacuum. The pellicles consist of 70 nm thin Au film deposited on 4 μm thick Kapton film, which was stretched and epoxied (vacuum compatible Masterbond EP30-2 epoxy) to a beveled stainless-steel ring (National Photo Color Inc.), and mounted within our β-collimator assembly. In the previous ^{37}K experiment the in-vacuum mirrors consisted of a thin high reflector ($TiO_x + SiO_x$) dielectric stack deposited on 273 μm of SiC, which led to non-negligible β-scattering and energy deposition, particularly for low energy β's in the mirrors prior to detection in the $E - \Delta E$ detectors, necessitating 400 keV scintillator threshold and 40 keV DSSD thresholds. The goal of the pellicle mirrors in this experiment is to drive the scintillator thresholds down to our DSSD thresholds to ensure the majority of the highest energy $\bar{\nu}_e$ events are accepted by the DAQ system.

3.3 Recoil Events

Full details of the rMCP spatial and temporal calibration, and the recoil event selection are detailed in the subsections below.

3.3.1 Recoil Event Selection
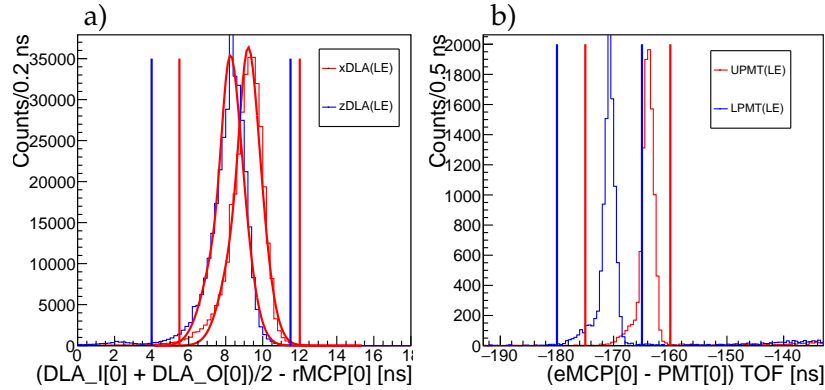
Figure 3.3: a) rMCP-DLA timing sum gate for recoil-event selection (*rMCP*) utilizing the x (red), and z (blue) DLA detector planes with Leading Edge (LE) constant-fraction trigger. b) SOE-Scintillator eMCP-PMT TOF spectrum of the Recoil-SOE-SCINT coincident events using the upper (red), and lower (blue) scintillators with indicated timing bounds chosen to suppress false coincidence events.

The recoil detector consists of a Z-stack (3-plate) microchannel plate (MCP) backed by a xz-position sensitive delay line anode (DLA). The rMCP hit timing signals are picked off the front-MCP electrode high-voltage feedthrough. The MCP is an analog amplifier consisting of lead-glass with micro-channels in a hexagonal unit cell with parallel channels having an axis oriented at 20° to the plates' normal. Incident charged particles on the MCP channels excite surface secondary-electrons within the channel. With a large bias of 1 kV/mm across the MCP plate, incident charge particles scatter off the channel surface successively producing secondary electrons which themselves produce subsequent secondary electrons, producing electron multiplication resulting in an electron shower out the rear of the MCP channel. A drift space is placed between the plates to allow for space charge repulsion and spreading of the electron shower over several channels of the following MCP. The rMCP consisted of an impedance matched Z-stack over three plates (diam. 86.7 mm, active diam. 77 mm, width 1 mm, chnl. spacing 32 μm, chnl. angle $\theta_{CH} = 20°$, chnl. diam. $D_{CH} = 25\mu$m). An amplification of 10^{11} is nominally achieved, distributed over the Z-stack MCP. The first MCP plate in the Z-stack facing the trap is mounted

such that the micro-channel is $\theta_{CH} = 20°$ to the normal incidence in the xy-plane. This aids in reducing pulse-height dependent efficiency effects along the z-axis, which will be important in future polarized ^{37}K experiments requiring a quantization axis along this axis. The subsequent two plates in the Z-stack are incrementally oriented at 60° and 120°, to average out potential orientation dependent microchannel non-linearities of individual plates over the detector surface.

The final electron shower out of the rear of the 3rd MCP plate then expands as a cone prior to collection on the DLA. The DLA consists of two orthogonal planes (xz) of counter-wound pairs of copper wires. The counter-wound wire pairs have opposing polarity such that induced potentials from the deposited charge propagate in opposing directions required for absolute 1-dimensional position reconstruction. Timing signals are extracted from the x_1, x_2, and z_1, z_2 DLA anodes, with their difference $x_1 - x_2$, and $z_1 - z_2$ having a direct proportion to the x, and z-position hit coordinates, respectively. A 2D metal grid mask in-front of the MCP permanently blocks some of the MCP channels, providing an in-situ spatial calibration of the timing differences with hit coordinates in the x and z-planes, and this will be discussed below.

Due to the low signal thresholds placed on our DLA (4 timing channels) and rMCP (1 timing channel) constant fraction discriminators, random electronic noise and discharges can fire each channel independently. In the case of the counter-wound copper wires of the DLA, the net transit time is independent of impact position in the x and z-dimension independently with respect to the timing signal of the rMCP ion hit. This is a consequence of the counter-wound wires having comparable length and the charge deposited over a localized number of turns on the DLA. Consequently, candidate recoil events recorded as the first event entering acquisition in the DLA $(x_1, x_2, z_1, z_2[0])$ and rMCP[0] must satisfy the timing sum criteria where $(x_1[0] + x_2[0])/2 - rMCP[0]$, and $(z_1[0] + z_2[0])/2 - rMCP[0]$ with timing bounds (5.5,12.0) ns (red), and (4.0,11.5) ns (blue) as shown in Figure(3.3a), respectively. Events with timing sums outside of these windows are considered time random false triggers. The TDC linear channel dispersion of δt_{TDC} from our DAQ was assumed in this analysis. This DLA-rMCP summing criterion on $rMCP$ events significantly aided in suppressing false triggers present in the event stream of the recoil detector. The FWHM

of the DLA-rMCP summing criterion is $\sim$ 2ns in x and z-dimensions and represents their convolved nominal timing resolution.

In the Recoil-SOE-SCINT event stream the timing is obtained from the rMCP[0] and the PMT[0] timing differences, as the restricted solid angle of the scintillator aides in suppressing false coincidences from decays originating from the electrostatic hoops present in the Recoil-SOE coincident data stream; this will be discussed later. One property of this triple coincident data-stream is the requirement of one or more atomic SOE. The largely mono-energetic SOE's (eV scale) are accelerated by the $\vec{E}$-field and impinge on the eMCP, yielding a clean SCINT-SOE TOF resonance as shown in Figure(3.3b) providing an additional constraint on true recoil events. SCINT-SOE TOF gates using the UPMT (red) with TOF within (-175,-160) ns, and LPMT (blue) within (-180,-165) ns are shown in Figure(3.3b) and applied to our Recoil-SOE-SCINT coincident data. Similarly, a correlated event timing resolution of $\sim$ 2ns FWHM in the eMCP-PMT coincidence is achieved with UPMT and LPMT detectors.

3.3.2 Absolute Event Timing

In the case of the Recoil-SOE coincident events, the TOF is determined from the timing difference between the rMCP[0] and the eMCP[0], which neglects the SOE TOF through the vacuum, along with electronic delays of the respective signals into acquisition. Efforts were made to trace delays from detectors into acquisition as drawn schematically in Figure(A.1); however, in the end there remained some unknown delays. Fortunately, a subset of Recoil-SOE events result from the accumulation of neutral ^{92}Rb, along with its progeny, on the surface of the rMCP. These subsequently beta decay where the beta fires the rMCP and the atomic SOE and/or secondary electrons drift through the $\vec{E}$-field and trigger the eMCP. The result is a prompt Recoil-SOE coincident TOF resonance as shown in Figure(3.5) centered at -6 ns. The second broad TOF resonance centered at 14 ns relative to the prompt events is of unknown origin, but may result from the rMCP firing later after the ejected recoil impacts the rMCP. We define the Recoil-SOE TOF as

$$\text{(rMCP - eMCP) TOF} = \text{(rMCP[0] - eMCP[0])} - (\Delta\text{rMCP} - \Delta\text{eMCP}) - \delta_{rMCP}^{eMCP}$$

where the timing delays are listed in Table(3.1). Note there are differences between the measured delays in Figure(A.1) and those implemented in this analysis in Table(3.1).
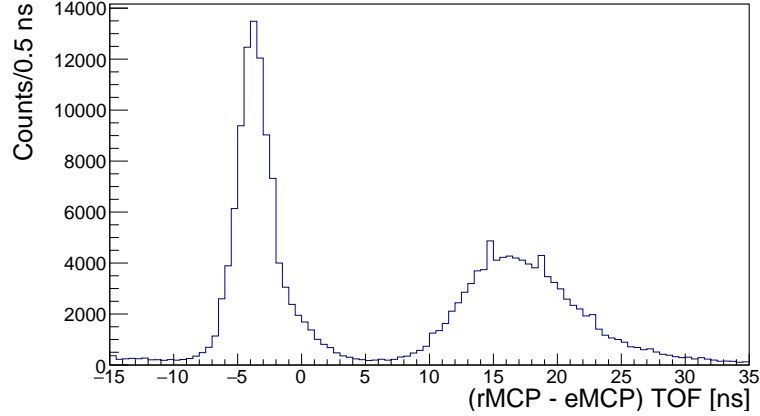
Figure 3.4: Recoil-SOE coincident TOF spectrum.

Table 3.1: Timing Offsets

Measured Offsets	[ns]	Added Offset [ns]	[ns]
ΔeMCP	54.5	δ_{rMCP}^{eMCP}	2.0
ΔrMCP	83.7	δ_{UPMT}^{rMCP}	-36.0
ΔUPMT	184.0	δ_{LPMT}^{rMCP}	-38.5
ΔLPMT	188.6	δ_{UPMT}^{eMCP}	-34.0
		δ_{LPMT}^{eMCP}	-37.0
		δ_{LPMT}^{UPMT}	0.0

Similar to the Recoil-SOE coincidence, a prompt coincidence exists in Recoil-SOE-SCINT. For these the beta incident on the scintillator fire the PMT, scattering or producing bremsstrahlung photons, which may subsequently fire the rMCP. Figure(3.5a,b) displays triple coincident (eMCP - PMT) TOF vs. (rMCP - PMT) TOF using the upper, and lower scintillator, respectively where

$$(\text{eMCP - PMT}) \text{ TOF} = (\text{eMCP[0] - PMT[0]}) - (\Delta\text{eMCP} - \Delta\text{PMT}) - \delta_{PMT}^{eMCP}$$

$$(\text{rMCP - PMT}) \text{ TOF} = (\text{rMCP[0] - PMT[0]}) - (\Delta\text{rMCP} - \Delta\text{PMT}) - \delta_{PMT}^{rMCP}.$$

The subset of events triggered by beta's and photons correlated with true decay SOE are shown at rMCP-PMT = 0 and eMCP-PMT = 0 ns. The diagonal line of events are TOF random false coincidences between the four event channels with the resonance centered at (1400,1400) ns corresponding to false coincidences with the dominant **+1** recoil charge state where there is no SOE. The line of

events along eMCP-PMT = 0 ns correspond to true coincidences from decays originating at the trap where the mono-energetic SOE produce a constant SOE-SCINT TOF.
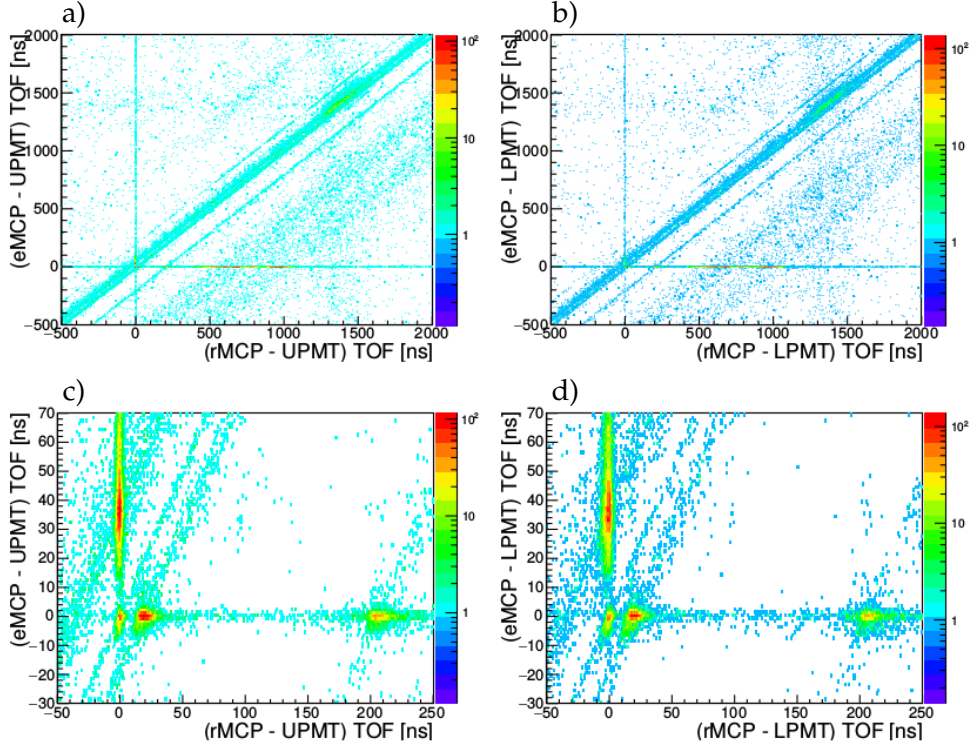
Figure 3.5: Recoil-SOE-SCINT coincident TOF spectrum with the a,c) upper, and b,d) lower scintillators, respectively. The expanded region of a,b) in c,d) show the centering in TOF about (eMCP - PMT, rMCP - PMT) = (0,0) [ns].

3.3.3 rMCP Spatial Calibration

Preliminary xz-calibration is performed in Figure(3.6a) with xz-correlated *Fourpt* 4-point mapping algorithm. Given four defined mask calibration points (X_1, Z_1, $X_2, Z_2, X_3, Z_3, X_4, Z_4$), and corresponding measured points ($x_1, z_1, x_2, z_2, x_3, z_3$, x_4, z_4) a mapping function F can be parameterized for any point (x,z) contained therein such that $F : (x,z) \rightarrow (X,Z)$

$$
\begin{aligned}
x \rightarrow X &= c_1 + c_2 x + c_3 y + c_4 x \cdot z \\
z \rightarrow Z &= d_1 + d_2 x + d_3 z + d_4 x \cdot z
\end{aligned}
\tag{3.1}
$$

where the constants c_1, c_2, c_3, c_4 and d_1, d_2, d_3, d_4 are uniquely determined. The inversion function F was computed in Mathematica and not shown here for

brevity.
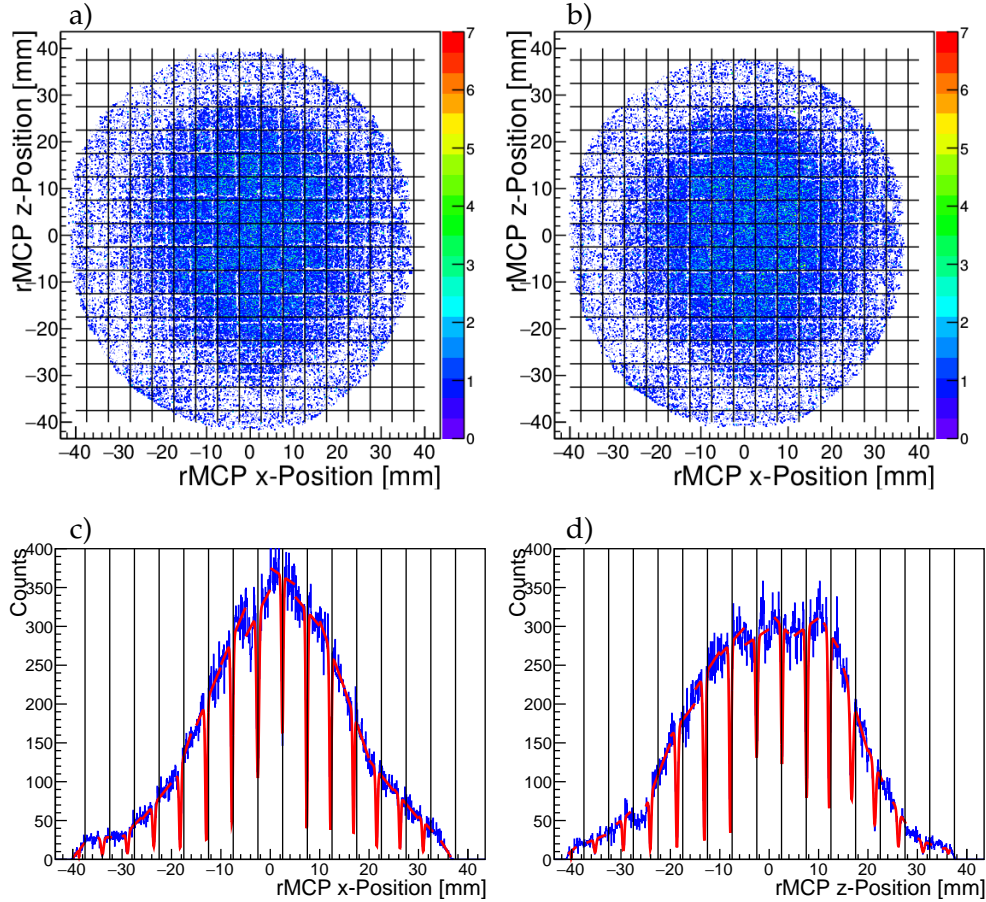
Figure 3.6: a) Rough recoil hit position calibration of the rMCP from delay-line-anode (DLA) timing signals. b) Hit position following correlated XZ-mapping via Fourpt mapping algorithm. Projections of b) are shown in c) x, and d) z with overlaid fits to local minima to determine piecewise-linear spatial scaling in x/z required for final calibration.

Preliminary calibration was applied to 4-points over the MCP surface in Figure(3.6a) and applied to all recoil events over the detector surface with results shown in Figure(3.6b). Projections of Figure(3.6b) in the x, and z planes are shown in Figure(3.6c,d), respectively. This procedure was necessary to remove the xz-linear correlation; however, non-linearities remained as can be seen in the x and z-projections where the vertical lines indicate true mask position centroids. Gaussian fits convoluted with a linear function were applied to each of these minima in projected recoil counts with the results overlaid on the projections. The remaining non-linear deviation in the x and z coordinates over

the MCP surface was taken to be approximately piecewise linear between adjacent Gaussian-fit minima in x and z, with corrected recoil 2D event distribution shown in Figure(3.7). The point-like regions with event deficits (roughly 6 visible) likely resulted from HV-discharges within the vacuum during HV conditioning and experiment, and locally damaged the MCP channels.

Two sets of event types will be analyzed below, the first being recoil shake-off-electron coincidence ($rMCP$-SOE) representing the largest dataset since events are collected in 4π. The second event type will be triple coincident Recoil-SOE-Scintillator ($rMCP$-eMCP-PMT) events, which has the advantage of better signal isolation against backgrounds through the narrow timing gate that can be applied between the beta trigger and arriving SOE, but is limited by the solid angle of our scintillator/collimator. We employ the same recoil summing criterion above on the $rMCP$ event in both event types.
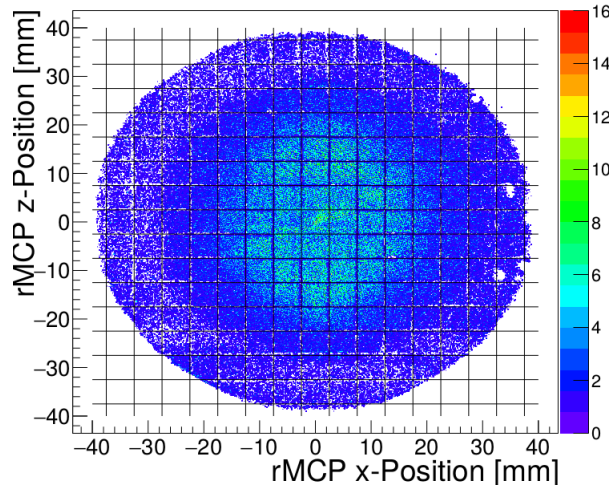
Figure 3.7: Corrected recoil hit position after uncorrelated piecewise-linear scaling in x, and z from fits performed in Figure(3.6c,d) respectively.

3.4   Non-Uniform $\vec{E}(\vec{r})$ Field

The $\vec{E}$-field oriented along the +y-axis is applied to separate the the recoiling daughter charge states in TOF. The proximity of the beta detectors to the trap was necessary to maximize beta collection efficiency, without interfering with collection of the recoiling ions. The requirement that the anti-Helmholtz coils and grounded beta-collimator be so close to the HV electrostatic hoops in our

geometry introduces unavoidable $\vec{E}$-field nonlinearities, and complicates the otherwise trivial exercise of reconstructing the recoil momentum in a uniform field.

Given the known geometry, the electric potential applied to each electrode was optimized using COMSOL 3D finite-element simulations to ensure near-uniform $\vec{E}$-field in the drift volume of the experimental chamber, particularly along the central drift axis (y-axis). Due to the proximity of the effectively grounded magnetic-field coils needed for trapping and the HV electrostatic hoops, field non-linearities are predominantly furthest from the trap region nearest to the coils as shown in Figure(3.8a) for $\vec{E}(0, y, 38mm)$. Conversely, further from the coils the field $\vec{E}(38mm, y, 0)$ is reasonably uniform with maximal deviations $O(20V/cm)$ over the bulk of the drift axis. Non-linearities near hoop #1 (y = 75.5 cm) and the rMCP (y = 97 mm) resulted from non-optimal voltage settings in the experiment which are shown in Figure(3.8b). Naturally, the field non-linearities along the y-axis are further suppressed where $\vec{E}(0, y, 0)$ deviations are maximally $O(10V/cm)$ over the entire ion drift length.

Due to the $\vec{E}$-field non-linearities, corrections must be applied event-by-event to map the observed hit position $X' = (x', z', t')$ to the ideal hit position $X = (x, z, t)$ had the field been perfectly uniform at $E_o = 998.5$ V/cm along the $+y$-axis. COMSOL was used to simulate the recoiling ^{92}Sr daughter both in the true non-uniform $\vec{E}$-field and the uniform field, thus comparing the hit position X' and X, respectively given identical initial recoil momentum. In this way we map a given recoil ion event from the data X' in the non-uniform field into the coordinate space of the same event X in a uniform field to easily extract the true recoil kinematics of the decay.

In β^--decay, nearly 80% of recoils are in the **+1** charge state, having emitted no extra atomic SOE. The abrupt change in the parent nuclei and atomic orbitals, however, can kick out valance electrons yielding **+2** and higher recoil charge states. The COMSOL-generated arrays for each charge state consist of square hit positions $\{X_{ij} = (x_{i,j}, z_{i,j}, t_{i,j})\}_i$ with position index $i = 1, 2, 3, 4$ (spaced by 4 mm) in a uniform field at time index $t_{i,j} = t_j$ (every 4 ns) and corresponding hit positions $\{X'_{i,j} = (x'_{i,j}, z'_{i,j}, t'_{i,j})\}_i$ in non-uniform field as shown in Figure(3.9). Recoil events $X' = (x', z', t')$ contained within the volume defined by
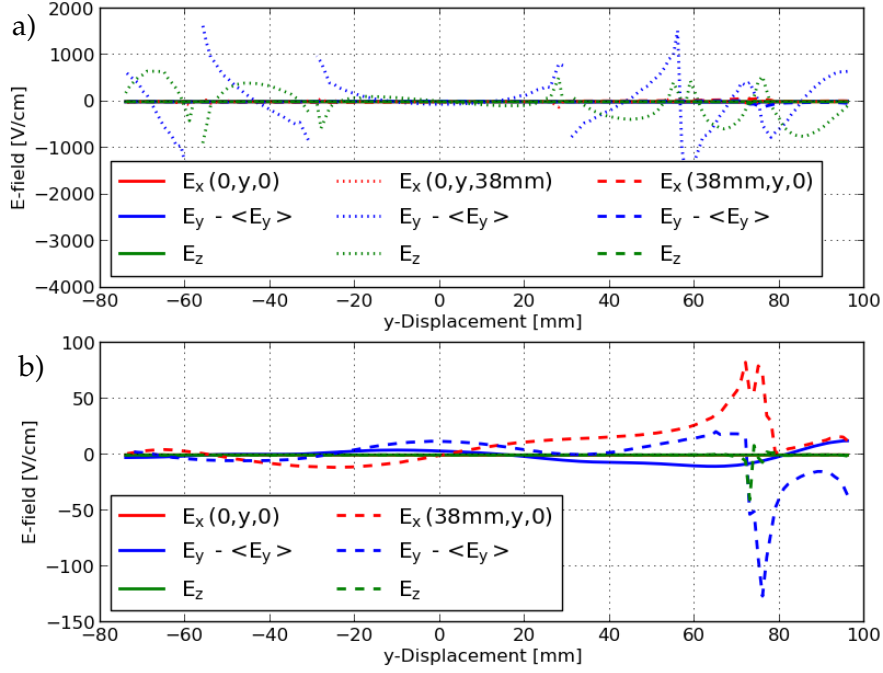
Figure 3.8: a) COMSOL simulated $\vec{E}$-field component values as a function of displacement from the trap center in the y-axis (rMCP at y = +97 mm) for given translational offsets in x, and z. $\langle E_y \rangle$ is the simulated mean field strength of 998.5 V/cm along the y-axis. b) Expanded view of minimally deviating field component profiles.

$\{X'_{i,j}, X'_{i,j+1}\}_i$ passing our selection criteria are then used to compute the set of coordinates $\{X'_i = (x'_i, z'_i, t')\}_i$ at time t' where for $\alpha'_{i,j} = (t' - t'_{i,j})/(t'_{i,j+1} - t'_{i,j})$ it follows that

$$x'_i = x'_{i,j} + \alpha'_{i,j} \cdot (x'_{i,j+1} - x'_{i,j}), \quad z'_i = z'_{i,j} + \alpha'_{i,j} \cdot (z'_{i,j+1} - z'_{i,j}). \quad (3.2)$$

The *Fourpt* algorithm above was then implemented to map $(x', z') \rightarrow (x, z)$ and $t' \rightarrow t$ where for $\left\langle \alpha'_{i,j} \right\rangle_i = \sum_{i=1}^{4} \alpha'_{i,j}/4$

$$t \simeq t_j + \left\langle \alpha'_{i,j} \right\rangle_i (t_{j+1} - t_j). \quad (3.3)$$

The recoil event coordinate transformation will be demonstrated later when discussing the experimental results. It should be noted that in both a uniform and nonuniform $\vec{E}$-field the transformation from hit coordinate X, X' to their respective recoil momentum coordinates is one-to-one.
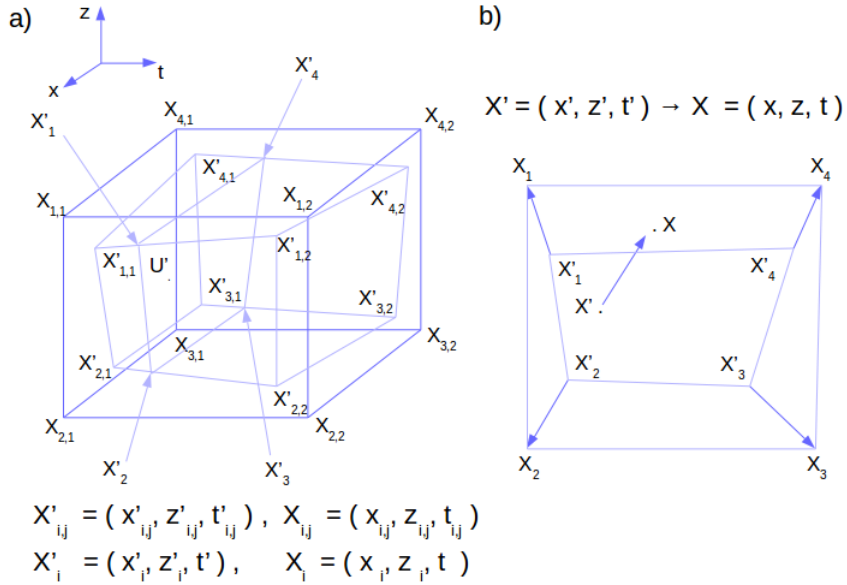
Figure 3.9: Mapping recoil hit coordinates in non-uniform $\vec{E}$-field X' to coordinates X in uniform field via COMSOL-based mapping of simulated recoil events. a) Simulated recoil hit coordinate space unit cell in the non-uniform field (S'), and uniform field (S). b) Illustrated *Fourpt* stretching transformation mapping recoil hit coordinate $(x', z') \rightarrow (x, z)$.

3.5   Recoil Kinetic Energy and Momenta

The recoiling nucleus is non-relativistic, due to its mass M_r compared to those of the outgoing beta and neutrino, and thus classical kinematics can be applied in determining the recoil kinetic energy (K_r). Assuming a uniform collection $\vec{E} = E_y \hat{y}$ field, which is necessarily the case for a recoil hit in the transformed coordinate space $X = (\Delta x, \Delta z, TOF)$, the kinetic energy K_r for charge state q is

$$K_r = \frac{M_r}{2} \left[\frac{r^2}{TOF^2} + \left(\frac{l_y}{TOF} - \frac{qE_y TOF}{2M_r} \right)^2 \right]. \tag{3.4}$$

Here, $r = \sqrt{(\Delta x)^2 + (\Delta z)^2}$ and l_y is the distance from the trap to the rMCP front face ($TOF \rightarrow c \cdot TOF$ for expression with dimensional consistency). The recoil momentum $\vec{p}_r = (p_{rx}, p_{ry}, p_{rz})$ is also simply parameterized as

$$p_{rx} = M_r \cdot \frac{\Delta x}{TOF}, \quad p_{rz} = M_r \cdot \frac{\Delta z}{TOF}, \quad and \quad p_{ry} = \frac{M_r l_y}{TOF} - \frac{1}{2} qE_y TOF. \tag{3.5}$$

It is important to note that following the beta decay of ^{92}Rb the recoiling ^{92}Sr is non-resonant with the MOT trap beams and necessarily is unperturbed by the laser light of the trap and its associated magneto-optic forces.

3.6   Scintillator Energy Calibration
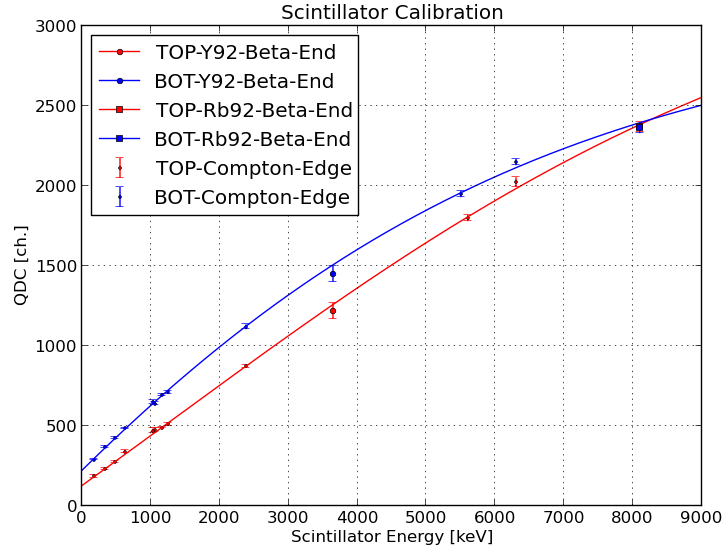
Figure 3.10: Top and bottom scintillator calibration using a combination of gamma-ray Compton edges and β endpoints. A significant non-linear response in the lower scintillator can be traced to a defective PMT base. Additionally, the 3.5 cm thick scintillators are thin enough that a small fraction of the most energetic beta's can leave the volume before depositing their full energy, or generate bremsstrahlung photons which escape detection. The result is less charge deposition at the largest beta energies and this may be another source of non-linearity in the detector response.

Scintillator media are nominally designed to be linear with the number of photons generated by energetic particles scaling with the energy deposited within its volume. Similarly, photo-multiplier amplification systems used to collect these photons and control electronics are also designed to have linear responses. The coupled scintillators and electronic systems, however, require calibration to build maps between the integrated charge reported from the photo-multiplier and a calibrant of known energy. Additionally, any physical system will have non-linearities at some level, which need to be accounted for to obtain an accurate calibration. The scintillator calibration performed here utilized a variety of measurements from γ-ray Compton edges, along with β-endpoint energies and cosmic muon events. When γ-ray photons of energy E_γ scatter off atomic electrons in the scintillator its final state energy E'_γ depends on the scattering angle θ,

$$E'_\gamma = \frac{E_\gamma}{1 + \frac{E_\gamma}{m_e}(1 - \cos\theta)}. \tag{3.6}$$

Table 3.2: Scintillator calibration parameters from fits to calibrants in Figure(3.10) using the saturation equation(3.8).

Scintillator	I_0 [ch.]	I_1 [ch.]	E_1 [keV]	δE_1 [keV]
UPMT	-2536.89	6138.26	1290.61	4873.30
LPMT	-6185.41	9241.54	-3782.23	4632.66

The maximum energy E_{Compt} deposited in the scintillator occurs for complete back-scatter events ($\theta = 180°$)

$$E_{Compt} = E_\gamma - E'_\gamma = \frac{2E^2}{2E + m_e} \tag{3.7}$$

manifesting as an abrupt edge in the scintillator energy spectra due to energy deposition above this being kinematicly forbidden. Several γ-ray sources were held adjacent to the scintillator including ^{133}Ba (356,302,384.0 keV with relative intensity 0.62, 0.18, 0.089), ^{22}Na (511_{anni}, 1274 keV), ^{137}Cs (661.7 keV), ^{92}Rb (814.98 keV), ^{60}Co (1173, 1332 keV), ^{40}K (1461 keV), ^{208}Pb (2615 keV), ^{92}Sr (1383.93 keV) ^{92}Y (3643 keV) providing calibration points as shown in Figure(3.10) dominantly below 2.5 MeV.

Ben Fenker (PhD-Thesis) performed GEANT-4 simulations of cosmic muon interacting in our scintillators noting a minimum energy deposition of 5600,5500 keV in the top, and bottom detectors with the most probable energy loss of 6300 keV. Cosmic muons are identifiable in our geometry by coincident hits in the top and bottom scintillators in the absence of recoil and SOE events with results shown in Figure(3.10). Additional calibration points were needed above 2.5 MeV to better constrain our calibration requiring us to use both the ^{92}Y and ^{92}Rb endpoints at 3643 and 8094 keV.

An important observation in our calibrations shown in Figure(3.10) was that both the upper UPMT (red) and lower LPMT (blue) scintillators appeared to have notable non-linearities. Although the scintillator and photo-tube in general have largely linear responses with energy deposition, non-linearities in the response can be present in general at some level. Although the upper scintillator (UPMT) appears largely linear, an apparent non-linearity in the detector response appears around 8 MeV. In the LPMT the non-linearity was significantly worse. The LPMT was noted to require significantly lower bias to the dynode

stack with only 1350 V (compared to the nominal 2100 V in previous experiments) so as not to saturate its response and ensure the 8.1 MeV ^{92}Rb endpoint remained on our QDC scale. We have attempted to phenomenologically model the non-linear response in both the LPMT and UPMT assuming a saturation response, which we parameterize in QDC-channel I vs. E

$$I(E) = I_0 + \frac{I_1}{1 + e^{-(E-E_1)/\delta E_1}}. \tag{3.8}$$

and fit to the data in Figure(3.10) from the respective detectors to provide our detector calibration. E_1 represents the saturation energy scale with characteristic width δE_1 and saturation value $I_0 + I_1$. The calibration parameters from equation(3.8) are shown in table(3.2).
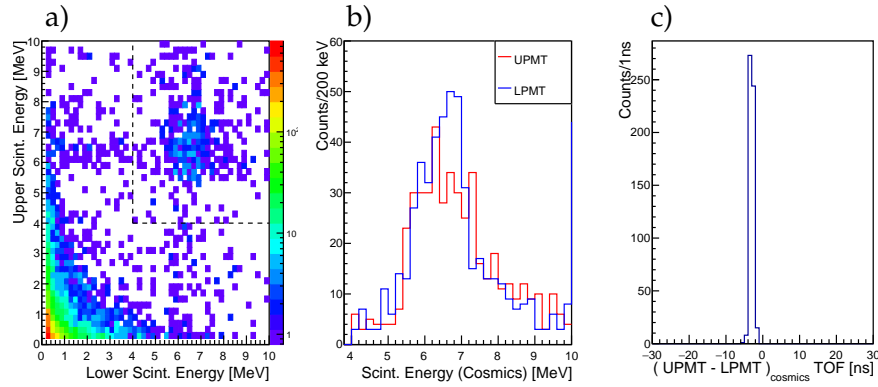
Figure 3.11: a) UPMT-LPMT coincident events in the absence of recoil's and SOE's with cosmic muon in the dashed region having corresponding energy spectrum projections in b) and relative timing difference in c), respectively.

With our scintillators calibrated, cosmic muon coincidences are shown in the correlated top vs. bottom scintillator energy in Figure(3.11a) with energy projections within the dashed lines in b) and timing difference in c). The timing difference between the upper and lower scintillators is defined by

(UPMT - LPMT) TOF = (UPMT[0] - LPMT[0]) - (ΔUPMT - ΔLPMT) - δ^{UPMT}_{LPMT}

with measured and imposed timing offsets defined in Table(3.1). The 2 ns lead on the UPMT timing signal compared to the LPMT timing signal is consistent with the transit time of a relativistic muon punching through both scintillators.

3.7 $\bar{\nu}_e$ **Energy Spectrum and** Q_{exp}**-value Reconstruction**

Since the ^{92}Rb is nominally highly localized within the trap and cooled to mK temperatures, the initial state of the parent atom can be considered at rest prior to decay. With the initial recoil momentum $\vec{p}_r$ established above and the $\vec{p}_\beta$ momentum given by $\sqrt{E_\beta^2 - m^2}$, momentum conservation $\vec{p}_r + \vec{p}_\nu + \vec{p}_\beta = 0$ is invoked to reconstruct E_ν (assuming negligible rest mass)

$$E_\nu = \sqrt{p_r^2 + p_\beta^2 + 2 \cdot p_r p_\beta \cos \theta_{\beta r}} \qquad (3.9)$$

where $\theta_{\beta r}$ is the β-recoil angle. In the final analysis the DSSD strip detector, along with the absolute trap position and known p_r will be used to determine $\theta_{\beta r}$ to properly reconstruct E_ν. Due to the significant complexity of calibrating the DSSD strip-by-strip against GEANT4 simulations and building the analysis code to reject false events, a simplified analysis was performed where we assume the beta enters the upper/lower scintillator parallel to the $\pm$z-axis, respectively. If θ_r is the angle made between $\vec{p}_r$ and the y-axis and ϕ_r the azimuthal angle from the x-axis in the xz-plane, then for the initial recoil momenta unit vector $(\hat{x}, \hat{z}, \hat{y}) = (\sin \theta_r \cos \phi_r, \sin \theta_r \sin \phi_r, \cos \theta_r)$

$$\cos \theta_{\beta r} = \sin \phi_r \cdot \sqrt{1 - \cos^2 \theta_r} \qquad (3.10)$$

where $\sin \phi_r = \Delta z / r$, and $\cos \theta_r = \delta / \sqrt{r^2 + \delta^2}$, for $\delta = l_y - \frac{1}{2} \cdot \frac{qE_y}{M_r} \cdot TOF^2$.

The Q-value of the β-decay transition accounts for the total change in kinetic energy between final and initial states, with rest mass M_f and M_i such that $Q = M_i - M_f$. We define the effective experimental Q_{exp}-value here as the sum over beta, neutrino, and recoil kinetic energy

$$Q_{exp} = E_\beta + E_\nu + K_r - m. \qquad (3.11)$$

In the GS transition $Q_{exp} = Q$, while in the decay through excited states $Q_{exp} < Q$, as the energy carried off by the gamma cascade is not measured. In the case of ^{92}Rb, the strong GS transition will thus produce a resonance in Q_{exp} at the 8.1 MeV Q-value of the decay. In the case of decays to excited states of the daughter, however, the gamma-cascade carry off a significant fraction of the available energy, while also perturbing the recoil momentum and incorrectly reconstruct E_ν, yielding a broad distribution of events with $Q_{exp} < Q$.

3.8   Photo-Ions
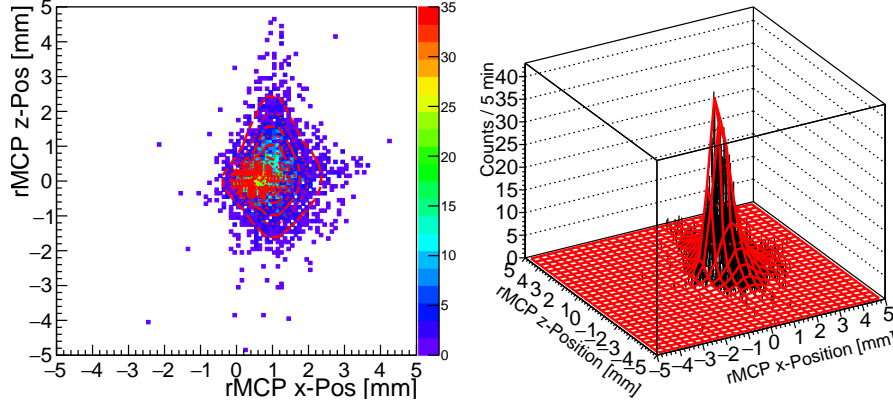
Figure 3.12: Photo-Ion event distribution fit with superposition of three Gaussian ellipsoids per 5 min of acquisition to check for small time dependent trap drift in the xz-plane.

Photo ions are used to monitor the time dependent trap drift, since constraining the initial position of the decay is essential to reconstruct the initial recoil momenta. A diode pumped 355 nm UV pulsed (0.5 ns) laser is used to singly ionize a subset of the trapped atoms. The rep rate is 10 kHz with 100 μs between pulses and essentially negligible proportion of coincident beta decay events with PD trigger. The UV beam enters the vacuum through optical ports at $35°$ to the z-axis in the xz-plane, and is retro-reflected from an external mirror back along the incident path. Photo-ion (PI) events are selected from coincident PD-eMCP-$rMCP$ event triggers with 5 min of integration shown in Figure(3.12). Three Gaussian ellipsoids were fit simultaneously to the xz-distribution to model the inner (I) strongly trapped population , and outer (O_1, O_2) halo-type populations distributed along the x, z-axis, respectively

$$N_o + \sum_{k=I,O_1,O_2} A_k \cdot exp\left[-\left(\frac{x' - x'_k}{\sqrt{2}w_{xk}}\right)^2 - \left(\frac{z' - z'_k}{\sqrt{2}w_{zk}}\right)^2 \right] \tag{3.12}$$

where (A_k) are the amplitudes, (x'_k, z'_k) the centroids and (w'_k, w'_k) the widths of the $k = I, O_1, O_2$ fit distributions. The inner distribution is defined as that with the largest amplitude, while the outer halo distributions have the two smallest amplitudes. The three distinct distributions of atoms may be connected with the recent replacement of the vertical trapping mirrors (along z-axis) with Au-coated pellicle mirrors. Visual observation of the beam profile upon reflection

from the pellicle appeared uniform within 10 cm of the surface, but had notable intensity non-uniformities at 1m from the surface likely from thickness nonlinearities of the supporting Kapton membrane. Combined thickness nonlinearities were measured by National Photo Color to be 5λ ($\lambda = 770$ nm) over a 2 cm beam diameter, while a typical optical mirror on a solid substrate has $\lambda/10$ flatness. Intensity nonlinearities over the trapping region may perturb the trap population.
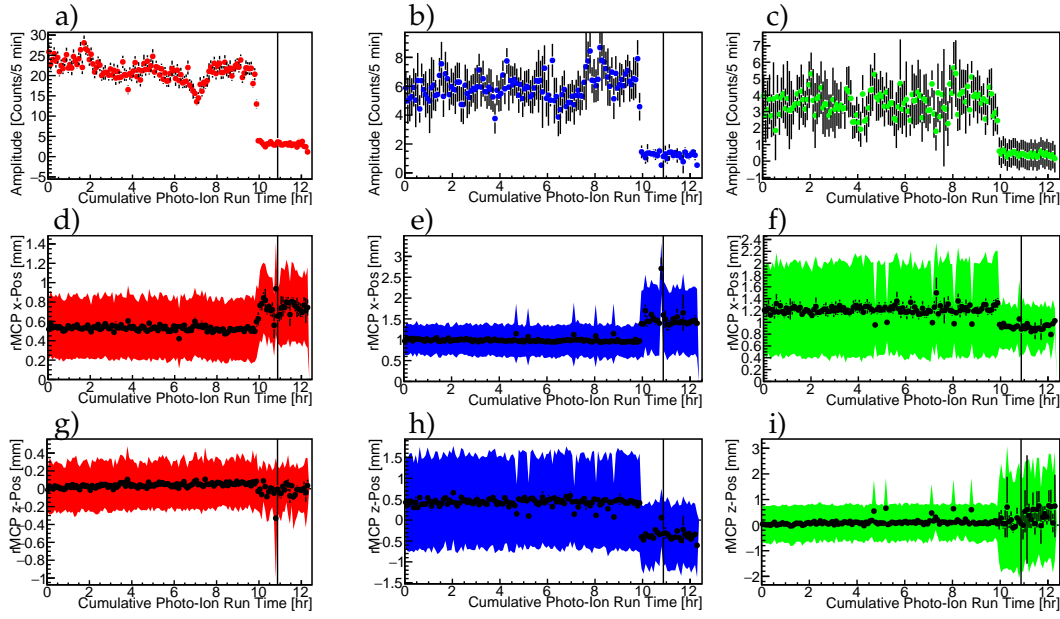
Figure 3.13: Photo-Ion distribution a),b),c) amplitude, d),e),f) x-centroid and width (coloured bounds), and g),h),i) z-centroid and width (coloured bounds) of inner I(red), and outer O_1 (blue), O_2 (green) elliptical-Gaussian fit parameters, respectively, vs. cumulative run time of the 1 kV/cm dataset.

The cumulative time dependent fit parameters of equation(3.12) to the photo-ion distribution per 5 min exposure are shown in Figure(3.13) with distribution (a,b,c) amplitudes, centroid (d,e,f) x-component (g,h,i) and z-component (widths being the colored bounds) are shown for the I(red), O_1(blue), O_2(green) distributions, respectively. Measurable time dependent deviation can be seen in all these parameters particularly near the 10 hr mark when we lost the optimal laser-lock, and could not be re-established optimally before the end of data taking. Since we cannot distinguish if a decay originates from either the inner or outer distributions we establish the trap centroid as a weighted average of the centroids by their numerically integrated inner (N_I), and outer (N_{O_i}) fit

distribution populations with trap centroid defined as

$$\vec{r}_{IO} = [N_I \vec{r}_I + N_{O_1} \vec{r}_{O_1} + N_{O_2} \vec{r}_{O_2}]/[N_I + N_{O_1} + N_{O_2}]. \qquad (3.13)$$

Nominally, the $I/O_1/O_2$ trap was displaced transversely from the geometric center with the width of the inner distribution largely stable with width w_{xI}/w_{zI} of 0.30/0.30 mm, even after the laser miss-tune at the 10 hr mark. The outer populations were largely stable in width but appeared to have an inverted response following the 10 hr mark with the w_{xO_1}/w_{zO_1} expanding/shrinking while w_{xO_2}/w_{zO_2} shrinking/expanding. The distribution amplitudes also undergo notable reduction following the 10 hr mark.

The integrated drift corrected PI event distribution in xz-plane is shown in Figure(3.14). Due to the large sample set, the broad outer halo about the trap oriented along the projected MOT beam axes (z, and x-axis) are evident, parameterized by O_1, and O_2 distributions, respectively.
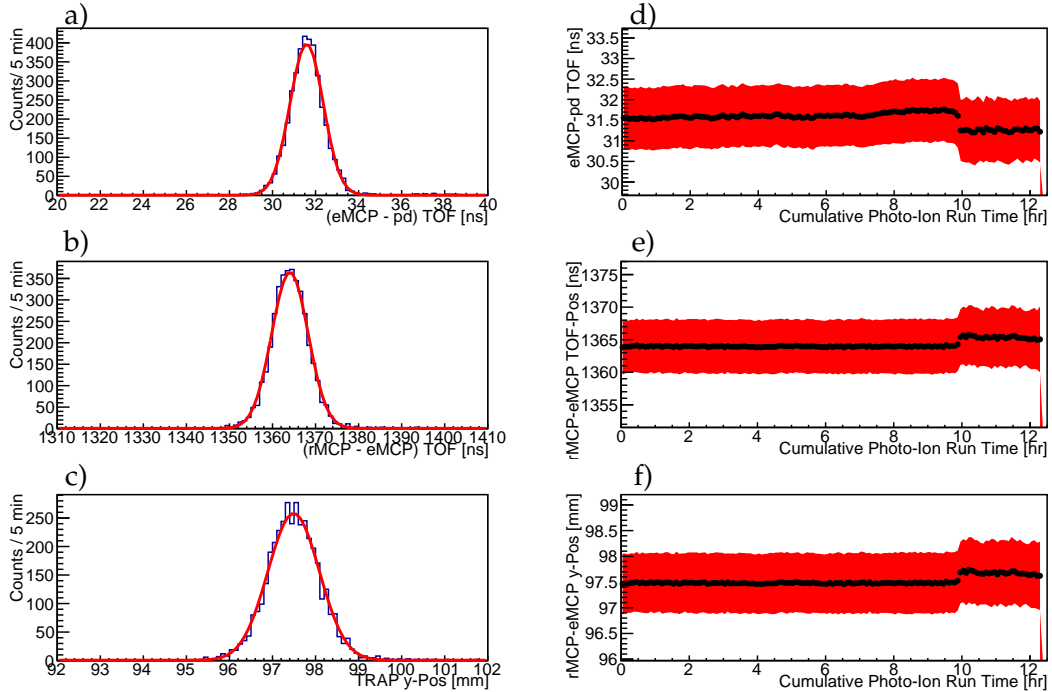
Figure 3.14: Photo-Ion a) SOE-PD TOF, b) Recoil-SOE TOF, c) y-displacement from trap centroid examples per 5 min of acquisition with overlaid Gaussian fits. Cumulative run time dependent Gaussian centroid (black-markers) and width (red-bounds) per 5 min of acquisition are displayed in d), e), and f), for the respective coincidence.

In the TOF dimension the 1d distributions for the photo-electrons, and photo-ions are shown in Figure(3.14a,b), respectively. The respective cumulative run-time TOF centroids (markers), and widths (red bounds) are shown in Figure (3.14d,e) similarly demonstrate a largely stable trap centroid along the y-axis with the exception of following loss of an optimal laser lock around the 10 hr mark. The anti-correlation in TOF of the photo-electrons and photo-ions is consistent with the trap moving further from the rMCP at the 10 hr mark. Given the photo-ions are singularly charged and the $\vec{E}$-field is known, the ion drift length l_y from the rMCP is determined with projection shown in Figure(3.14c) with nominal Gaussian centroid of 97.5 mm and width of 0.6 mm. Similarly, the cumulative run-time distribution centroid (marker), and width (red bounds) along the y-axis from the rMCP is shown in Figure(3.14f). The trap width and centroid along the y-axis were again largely stable with the exception of at the 10 hr mark, with the trap moving roughly 0.1 mm away from the rMCP. The drift-corrected photo-ion distribution integrated over the entire dataset is shown in Figure(A.2), clearly showing the three distinct populations of atoms in the xz-plane as mentioned above with indicated distribution centroid clearly offset from inner I trap population by the populations in the outer halo region.

3.9   Data Acquisition

The TRINAT DAQ hardware event timing schematic is outlined in Figure(A.1). The ΔE strip detectors are not shown as they have not been used in this analysis as of yet. Timing signals from the MCP's (eMCP,rMCP) are picked off the front face of the MCP HV through a preamp and fed into a Constant Fraction (CF) discriminator with the output timing sent to the acquisition. The timing signals from the scintillator PMT's (UPMT,LPMT) are taken from the first dynode in the photo tubes and sent to the CF discriminators with outputs sent to the acquisition. Multiple triggers were available to simultaneously fire the DAQ including A(PMT-singles), C(PMT - eMCP), D(PD - eMCP), E(PD - rMCP), and F(eMCP - rMCP). Trigger A, E, and F were enabled for the 1kV/cm data. Although the **+1** charge state in beta decay is the dominant recoil charge state with no atomic SOE, unfortunately the $\vec{E}$-field was not large enough to collect all recoils in 4π, and necessarily we have avoided this component of the event stream (trigger A). Since all events of interest in this analysis are above the **+1** charge state a SOE trigger from the eMCP is required with double coincident (trigger F) and

triple coincident (trigger A and F) event streams presented in this thesis. In principle, if one was not interested in **+1** charge states, enabling trigger C and F (instead of A and F) would cut down the dead time in the DAQ from the dominant beta-singles event type and increase data rates in the higher charge states.

Chapter 4

Experimental Results

4.1 Recoil-SOE Coincidence

4.1.1 TOF Spectra

Recoil-SOE coincident events directly give the recoil momentum from which an average value of ζ_o/ω can be obtained assuming the $a_1(W)$ correlation parameter defined in section 2.4. This represents the main experimental measurement of this thesis. Recoil-SOE coincident events represent an ideal event stream to maximize statistics, since with sufficiently large $\vec{E}$-field all recoil charge states can be collected in 4π. The distribution of drift corrected impact radius vs TOF is shown in Figure(4.1a) where the **+2, 3, 4**, and higher charge states can be seen partially separated in TOF. Gating on events in TOF within the *(red), (blue), and (green)* regions in Figure(4.1a), we can uniquely separate the *+2(red), 3(blue), and 4(green)* charge states subsets with the indicated 2D rMCP hit position shown in Figure(4.1b). The complication of not having an additional detector coincidence, however, leads to non-negligible false coincidence event distributions that must be understood to extract physics.

Time-random false coincidences can be assessed as nearly uniformly distributed recoil events in TOF over the rMCP detector surface. Deviations from such uniformity in TOF, however, can be seen, particularly near 1000 ns in Figure(4.1). This is more obvious in the radially integrated events of Figure(4.1) within the (teal) bounds, with the results shown in Figure(4.2). A resonance in the recoil TOF background indicates decays from a localized planar surface along the y-axis is contributing to the false coincidence event rate, and this is consistent with an accumulation of ^{92}Rb (and its progeny ^{92}Sr, ^{92}Y) on the HV electrostatic hoops, particularly those nearest to the trap. Decays from the central hoops (#5,6 from rMCP) interior surface facing the y-axis can yield a recoil-SOE which
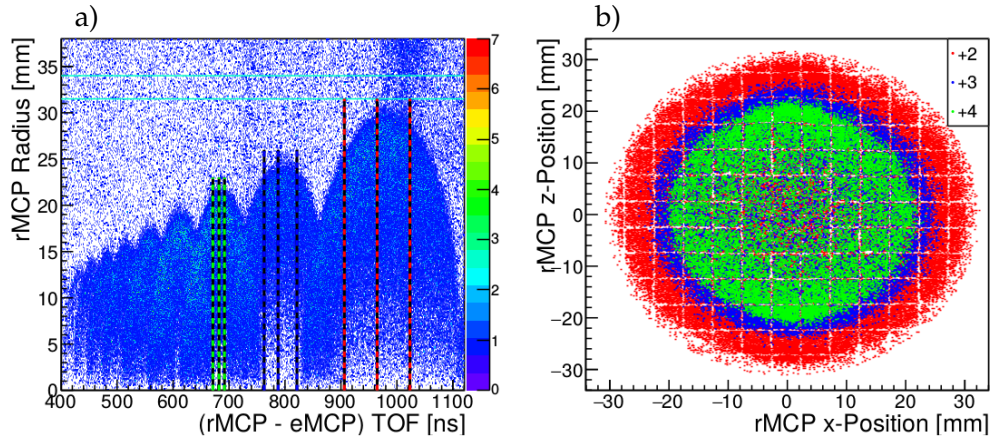
Figure 4.1: Recoil-SOE coincident a) drift corrected ion impact radius vs. TOF, and b) un-corrected recoil hit xz-position for *+2(red), 3(blue), and 4(green)* charge state events in respectively coloured TOF-bounds in (a).

may be ejected from the surface and collected in the respective detector, resulting in two TOF peaks consistent with those at (975,1025) ns, respectively. Decays from the hoops will preferentially occur from the face nearest translationally to the rMCP, namely the surfaces along the $\pm z$-axis compared to the $\pm x$-axis. The rectangular geometry of the HV hoops will necessarily be imprinted on the azimuthally symmetric distribution (about the y-axis) of decays from the trap, and will be discussed later.
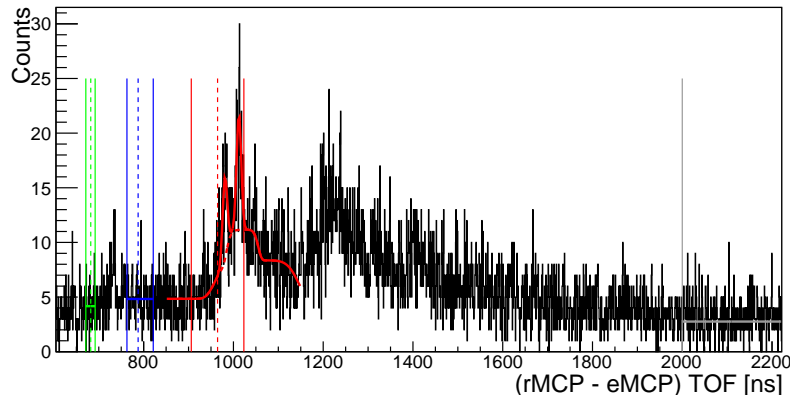
Figure 4.2: Recoil-SOE coincident random background levels vs. TOF integrated over the bounding (teal) lines in Figure(4.1). Fits within the charge state bounds *+2(red), 3(blue), 4(green)* provide a random background rate normalization relative to signal free region (grey) from which time random backgrounds are estimated. The location of the TOF peaks are understood to be real backgrounds and discussed later.

4.1.2 $\vec{E}$-Field Corrections

The technical details of this important correction were discussed in section 3.6. Mapping the recoil-ion hit coordinates X' to X was important to correctly reconstruct the recoil K_r across charge states. This is because each charge state samples different physical regions of the non-uniform $\vec{E}$ field, so each one requires differing degrees of correction. With the TOF isolation of the *+2(red), 3(blue), 4(green)* recoil charge states in *rMCP*-SOE coincidence of Figure(4.1b) a subset of the recoils which traversed the non-uniform $\vec{E}$-field have hit coordinates X' plotted in Figure(4.3a,b,c) (black), respectively. Overlaid are the transformed recoil hit coordinate distributions X had the recoil traversed a uniform $\vec{E}$-field of 998.5 V/cm for the respectively coloured *+2(red), 3(blue), 4(green)* charge states. The subset of the recoils with largest initial momenta transverse to the y-axis sample the fields closer to the hoops, where non-uniformities are larger, and necessarily require larger corrections in mapping X' to X, particularly in the *+2* charge state. The transverse distribution of corrections applied to each charge state in mapping X' to X are shown in Figure(4.3d,e,f), respectively. Two poles appear in the corrections in the $\pm$z-axis from the proximity of ground to the central region of the hoops along the y-axis (where perturbations the recoil trajectory are small) compared to the $\pm$x-axis where ground is much further from the central region.

4.1.3 rMCP Pulse-Height & Detector Efficiency

It is well known that MCP have ion impact angle and energy dependent quantum-efficiency for secondary electron emission, with respect to the MCP channel axis. Generally, the larger the channel angle the smaller these effects can be made, which is why the large $\theta_{CH} = 20°$ channel pitch angle to normal was chosen for this experiment. Below we detail the qualitative pulse height dependencies on our kinematic observables $p_{rx}, p_{rz}, K_r, \phi_r$, and the angle to the MCP channel axis θ_{ch}. Later we conclude the most practical technique to ascertain the relative efficiency mapped into the recoil K_r observable is through a left/right, and up/down counting rate asymmetry, which had non-negligible K_r dependencies, but maximally were on the order 5% in the smallest *+2* charge state.

Recoil event hardware triggers of the rMCP constant fraction discriminator (CFD) operated at a minimal detection threshold of 10 mV imply that pulses below this would not fire our DAQ. The Z-stack rMCP with fields of 1 kV/mm
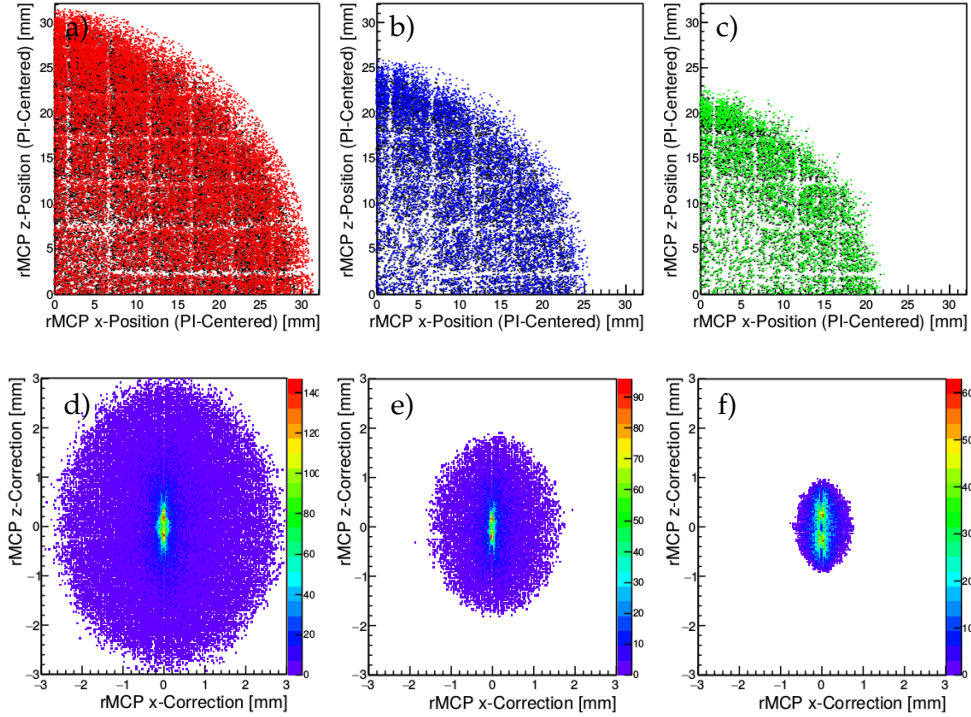
Figure 4.3: Drift corrected recoil xz-coordinate displacement distribution (*X*) following mapping above in Figure(3.9) $X' \rightarrow X$ (mean field of $\langle E_y \rangle = 998.5$ V/cm) of a) +2*(red)*, b) +3*(blue)*, and c) +4*(green)* charge states within TOF bounds in Figure(4.1a). The corresponding un-corrected recoil event distribution (*X'*) are shown as black points in the background for each of the respective charge states. The corresponding distribution of recoil hit xz-displacement corrections in mapping from $X' \rightarrow X$ are shown in d),e),f), respectively.

has the property that their response is largely saturated and independent of recoil impact energy, position, or orientation with respect to incident microchannel axis. Figure(4.4a,b,c) demonstrate the mean recoil MCP pulse height as a function of transverse momentum for charge states *+2, 3, 4*, respectively. Each recoil charge state demonstrate a clear deficit in the mean pulse height for small transverse momentum. This may result from the accumulation of ^{92}Rb and the progeny near the center of the rMCP, which beta decays in 4π, half of which may penetrate multiple MCP microchannels and fire the rMCP continuously over the run-time. Continuous firing of the central population of microchannels may thus locally degrade the gain over the run-time compared to the peripheral regions of the detector where the progeny is distributed over a larger surface area. In the *+2* charge state several locations in transverse momentum reveal pulse height deficits (eg. [-5,7] MeV/c) in the mean pulse height likely from sparks, which have locally damaged the MCP micro-channels reducing

their amplification. The pulse height distributions as a function of transverse momentum in p_{rx} are shown in Figure(4.4d,e,f), and p_{rz} in Figure(4.4g,h,i). A threshold of 50 channel units was imposed to suppress false triggers. No strong pulse height dependencies are immediately obvious in the transverse momentum distributions.
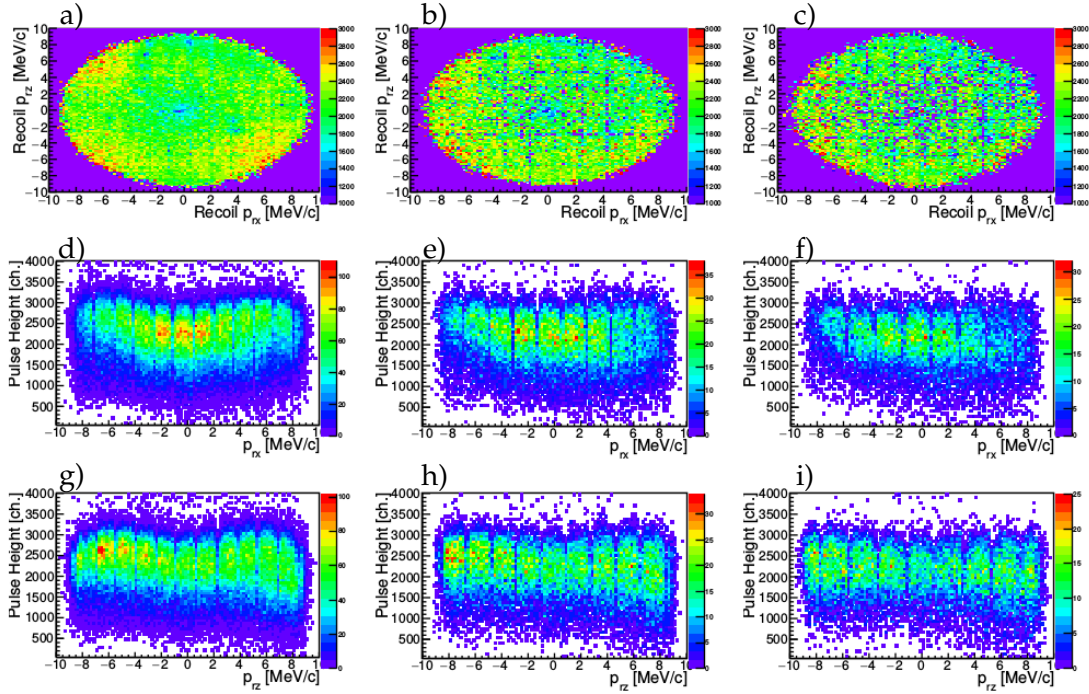
Figure 4.4: Charge state *+2, 3, 4* (left-right) a), b), c) mean rMCP pulse height dependence on transverse recoil momentum with, d), e), f) pulse height vs. p_{rx}, and g), h), i) pulse height vs. p_{rz} distributions, respectively.

Pulse height recoil kinetic energy dependencies of the *+2, 3, 4* charge states are shown in Figure(4.5a,b,c), respectively. Our analysis of the pulse height event dependency below will be restricted to kinematic regions where the azimuthal angular distribution ϕ_r in transverse recoil momenta are contained in $[-45°, 45°]$ and $[135°, 225°]$ to suppress hoop backgrounds as discussed above. Overlaid are the mean pulse height values as a function of recoil K_r. The *+4* charge state has a smaller dependency on K_r, as the impinging ions are closer to normal incidence than the lower charge states, which nominally sample larger detector radii. A simple linear fit was made to the mean pulse height distribution of the *+4* state and overlaid in red, which was used to normalize the mean pulse heights of the *+2, 3, 4* charge states, with results shown in Figure(4.5d,e,f) for the respective charge states. A clear enhancement in the mean pulse height

of the *+2* charge state is observed, which is roughly linear in K_r up to 240 eV and saturates with a 10% enhancement. Since the *+2* charge states sample larger radii, the spread in incident angle to the micro-channel axis is necessarily larger, and so more likely to impact with both smaller (and larger) penetration depths leading to larger (and smaller) pulse height extremes. We defer discussion of relative rMCP detector efficiency to later in this section.
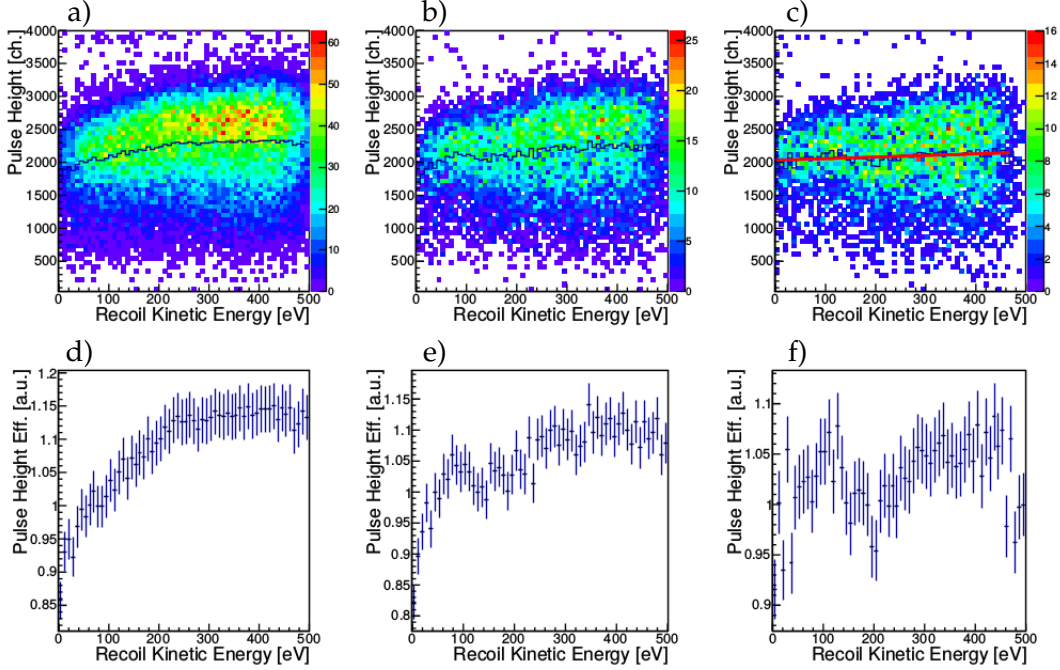
Figure 4.5: rMCP pulse height distribution vs. recoil kinetic energy K_r of charge state *+2*, *3, 4* (left-right) a), b), c) charge states with overlaid mean pulse height. Normalized mean pulse height to the linear fit of that of the *+4* charge state vs K_r are are shown in d), e), f) for the respective charge state.

Assuming the hexagonal array of MCP channels is on average uniform across the rMCP surface, we can examine dependencies both on azimuthal angle and impact angle with respect to the channel axis. The impact angle with respect to the channel axis θ_{ch} is computed from the known recoil impact momentum parameterized as $\vec{p}_r^{HIT} = (p_{rx}^{HIT}, p_{ry}^{HIT}, p_{rz}^{HIT})$ where in a uniform $\vec{E}$-field

$$p_{rx}^{HIT} = p_{rx}, \quad p_{rz}^{HIT} = p_{rz}, \quad p_{ry}^{HIT} = \frac{M_r l_y}{TOF} + \frac{1}{2}qE_y TOF, \tag{4.1}$$

it follows that

$$\theta_{ch} = \arccos\left([p_{rx}^{HIT}\sin\theta_{CH} + p_{ry}^{HIT}\cos\theta_{CH}]/|\vec{p}_r^{HIT}|\right). \tag{4.2}$$

The pulse height dependence on the incident angle to the rMCP channel axis is better illustrated in Figure(4.6a,b,c) with overlaid mean values for the *+2, 3, 4* charge states, respectively. The overlaid mean pulse heights are weighted toward smaller values near $0°$ for ions incident along the channel axis, while larger values are nominally obtained off the micro-channel axis. The maximal spread in θ_{ch} is also clearly reduced with increasing charge state from $\pm 9°, 7°, 6°$ for *+2, 3, 4* charge states, respectively, as the recoil ions impinge on the MCP closer to normal incidence. The azimuthal angular pulse height dependence is shown in Figure(4.6d,e,f) with no strong dependencies over the accepted event range. Given the mean micro-channel angle/orientation, nominal diameter and recoil momentum the ion penetration depth d_{ch} can be computed simply as

$$d_{ch} = D_{CH} / \tan\theta_{ch} \tag{4.3}$$

with results shown in Figure(4.6g,h,i) for charge states *+2, 3, 4*, respectively. Due to the orientation of the micro-channels at θ_{CH}, the recoils will impinge on the channels and achieve differing penetration depths for $p_{rx} > 0$ or $p_{rx} < 0$, potentially leading to a pulse height asymmetry and possibly a bias in our detection efficiency across the MCP surface. The mean pulse height distribution is overlaid in Figure(4.6g,h,i) for $p_{rx} < 0$ in blue, and $p_{rx} > 0$ in red for each charge state. Larger pulse heights are correlated with smaller penetration depths accomplished for $p_{rx} < 0$, compared to the more distributed pulse height distribution for $p_{rx} > 0$, which is evident in each charge state. This is consistent with the channels being oriented with $\theta_{CH} = -20°$ in the xy-plane of the chosen coordinate system. Additionally, for $p_{rx} < 0$ there is a roughly linear drop in mean pulse height with penetration depth into the channel up to 65 μm, while for $p_{rx} > 0$ a flatter distribution is achieved. Again, since the larger charge states nominally impinge on the MCP closer to normal incidence, a smaller maximum penetration depth is achieved, where for *+2, 3, 4* the maximum penetration depths are 130, 110, 100 μm. From the above information it is unlikely that the MCP is fully saturated in its response, although there is no obvious translation of the above into a rMCP detection efficiency that depends on recoil energy K_r.

We parameterize the relative MCP detector efficiency by investigating the left/right and up/down asymmetry in the recoil momentum distribution mapped into the recoil K_r observable. Plotted in Figure(4.7a,b,c) are the recoil K_r distribution's for hemispherical cuts in the transverse momentum space for the *+2, 3,*
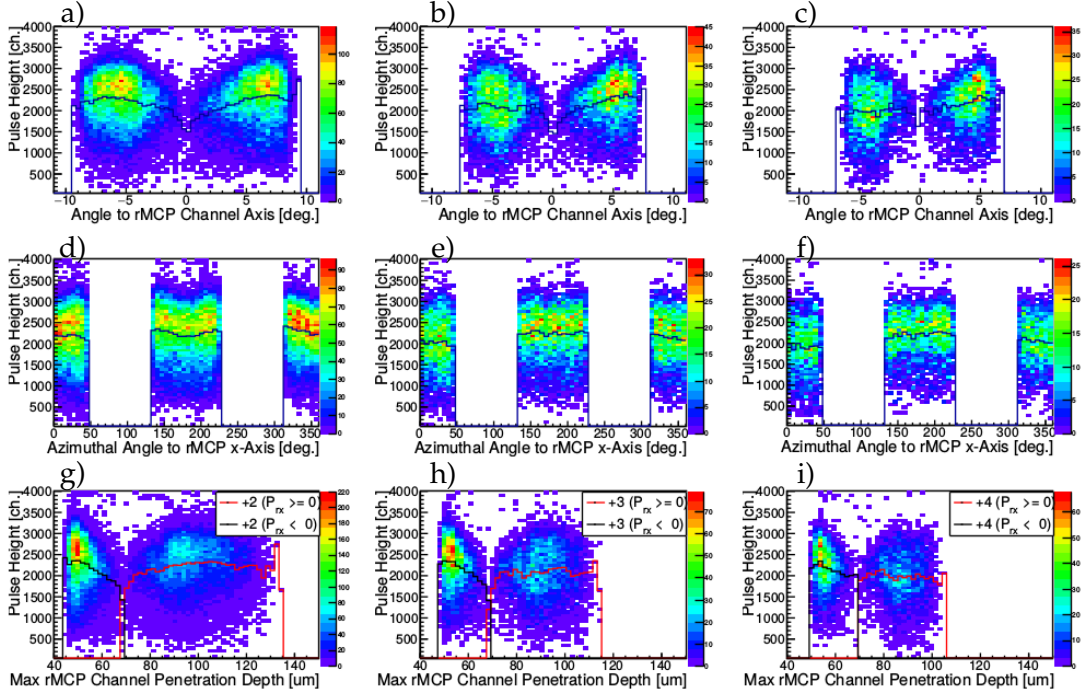
Figure 4.6: rMCP pulse height dependencies for charge states *+2, 3, 4* (left-right) on a),b),c) angle to rMCP channel axis, d),e),f) azimuthal angle in the plane of the rMCP, g),h),i) maximum rMCP channel penetration depth for ($p_{rx} < 0$ black-line), and ($p_{rx} > 0$ red-line).

4 charge states, respectively. Recoil K_r spectra were extracted for $p_{rx} \geq 0$, and $p_{rx} < 0$ in (solid-teal), and (dashed-teal) lines, respectively and similarly for p_{rz} indicated in (magenta). Asymmetries in the event rate x, and z-axis are computed as the ratios

$$\epsilon_{LR}(K_r) = 1 - \frac{dN/dK_r(p_{rx} \geq 0, K_r) - dN/dK_r(p_{rx} < 0, K_r)}{dN/dK_r(p_{rx} \geq 0, K_r) + dN/dK_r(p_{rx} < 0, K_r)}$$
$$\epsilon_{UD}(K_r) = 1 - \frac{dN/dK_r(p_{rz} \geq 0, K_r) - dN/dK_r(p_{rz} < 0, K_r)}{dN/dK_r(p_{rz} \geq 0, K_r) + dN/dK_r(p_{rz} < 0, K_r)}$$

(4.4)

with results displayed in Figure(4.7d,e,f) for each charge states *+2, 3, 4*, respectively. The distributions were fit assuming a linear dependence convolved with an exponential loss in efficiency near the largest recoil K_r. For the *+2* charge state a notable linear reduction in relative efficiency with maximal departures of order 5% at largest recoil K_r in both the left/right and up/down orientations can be observed. Such non-linearities are less significant in the larger charge states consistent with departures from uniform efficiency likely from several of

the convolved dependencies mentioned above.
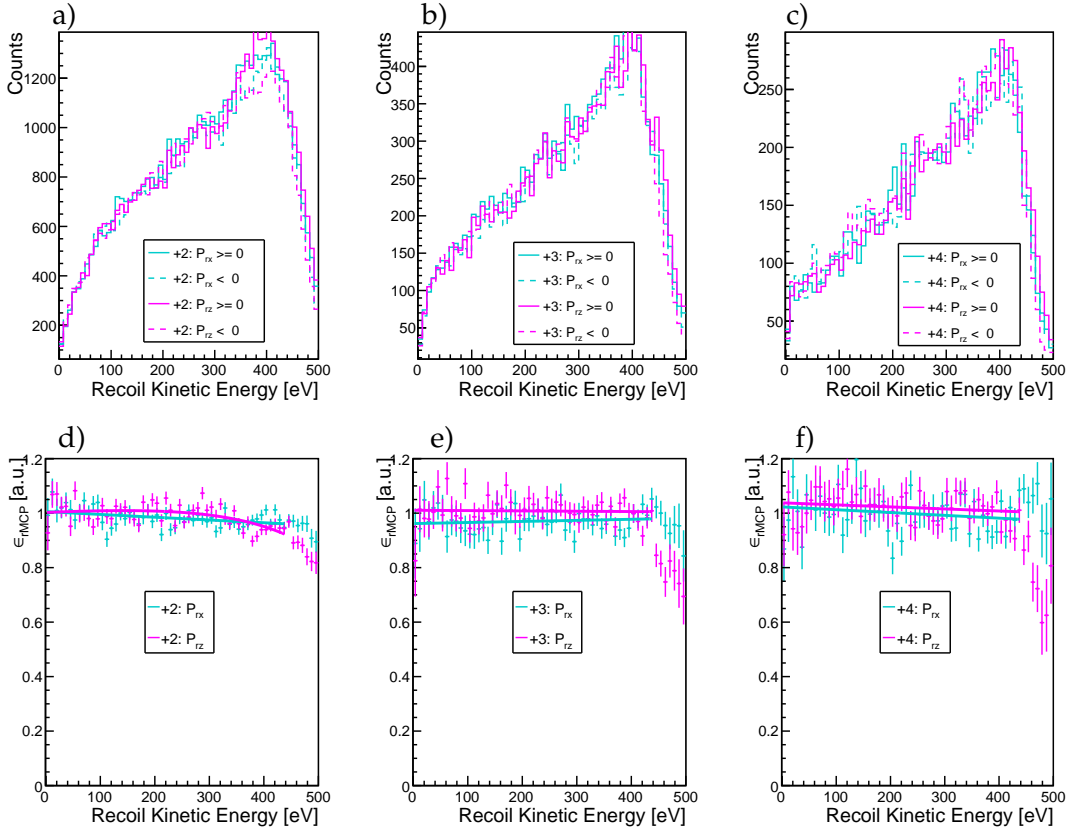
Figure 4.7: Recoil kinetic energy K_r spectrum integrated over indicated detector hemisphere for charge states *+2, 3, 4* in a),b),c), respectively, with (teal) corresponding the left/right and (magenta) up/down hemispheres. The corresponding Left/Right (LR) and Up/Down (UD) counting rate asymmetries parameterize the relative rMCP detection efficiency vs. recoil K_r dependence is shown in d),e),f) with overlaid fit functions parameterizing the relative efficiency $\epsilon_{LR}(K_r)$, $\epsilon_{UD}(K_r)$.

4.1.4 rMCP Detector Response Function

The presence of the calibration mask on the rMCP mentioned above in section 3.5 introduces significant non-linearities in the recoil K_r spectrum compared to the theoretical predictions from equation(2.8) above, and this is parameterized by a mask transmission function $\epsilon_m(K_r)$ shown in Figure(4.8), via a simple Monte-Carlo simulation. Additionally, the finite counting and event density at small recoil radius, and thus small K_r, further introduces non-linearities in this distribution and is parameterized by $\epsilon_{fd}(K_r)$. These detector effects will be used to scale the theoretical predictions of equation(2.8) as will be shown below

when fitting experimental recoil K_r spectra in section 4.1.6.
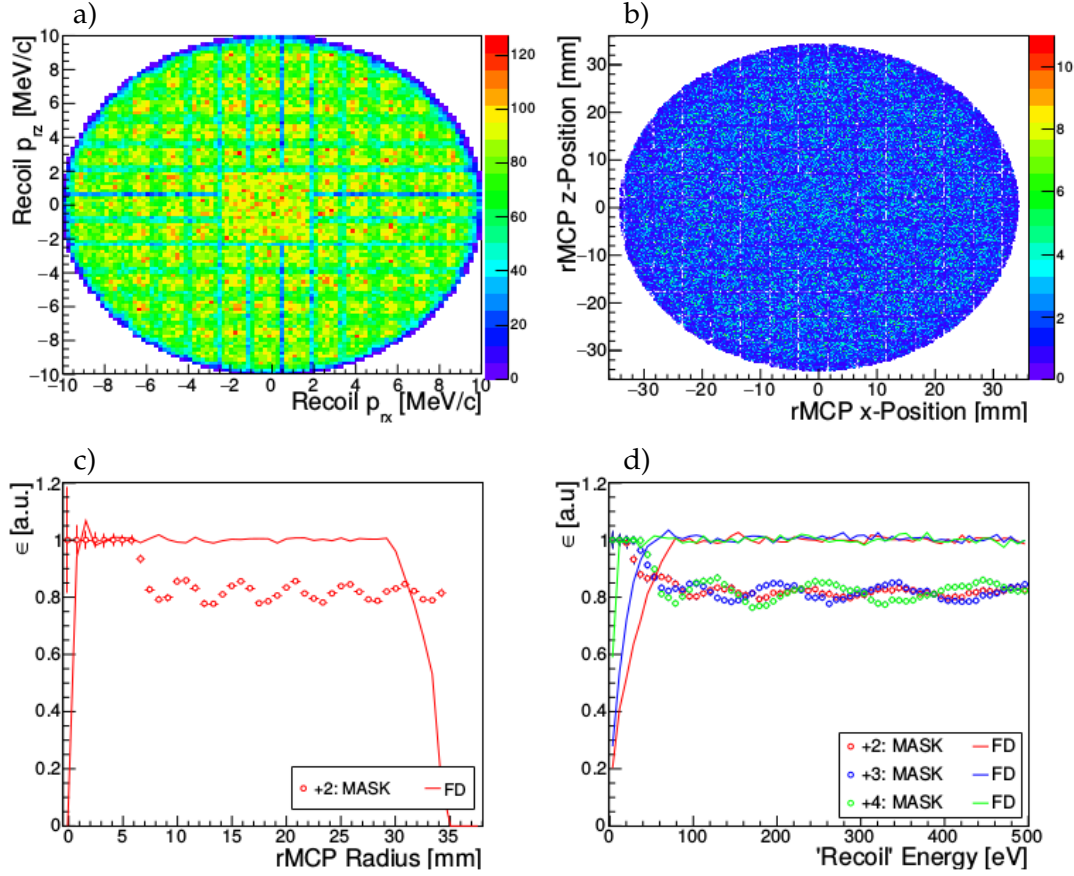
Figure 4.8: Simple MC of recoil ion in recoil-SOE coincidence assuming recoils with uniform randomly distributed momenta which traverse a uniform $\vec{E}$-field of $998.5\hat{y}$ V/cm within the given charge state TOF bounds in Figure(4.1a). The recoil +2 charge state passing these criteria and within the active area of the rMCP have transverse momentum distribution shown in a), and impact hit position distribution shown in b). Azimuthally integrated radial mask transmission efficiency (markers) and finite-density relative event rate effects (lines) of the +2(red) charge state are shown in c). Integrated mask transmission efficiency $\epsilon_m(K_r)$ (markers) and finite-density event rate efficiency $\epsilon_{fd}(K_r)$ (lines) vs. recoil K_r of the +2(red), 3(blue), 4(green) charge states, respectively are shown in d).

To quantify $\epsilon_m(K_r)$ and $\epsilon_{fd}(K_r)$, simulated recoils were generated from a point-like trap centered on the experimentally determined photo-ion (PI) distribution centroid from Section 3.10, with uniform-random momentum in 4π up to 10 MeV/c for each charge state. The simulated recoils traverse a uniform $\vec{E}$-field

of 998.5 V/cm and are incident on a simulated mask/rMCP detector with accepted events in the requisite charge state TOF bounds. The integrated transverse momentum distribution, and rMCP xz-displacement distributions centered on the PI distribution for the +2 charge state are shown in Figure(4.8a,b), respectively. As the trap drifts slightly in the xz-plane over the course of the experimental run-time (Section 3.10) the region of the mask kinematically accessible to the recoils correspondingly changes. The trap drift in effect smears out the mask pattern imprinted on the integrated 2D momenta, and displacement distributions. The simulated mask transmission vs. impact radius of the *+2(red)* charge state is shown in Figure(4.8c) (markers) determined from the ratio of events incident on the mask/rMCP, and the rMCP alone with clear non-linearities from the mask geometry present above 5 mm in radius at nominal transmission of ~80%. The trap drift has the effect of smoothing out the extrema of the integrated mask transmission function vs. impact radius. The finite event density vs. impact radius is also overlaid (line), determined by normalizing the radial recoil event distribution to the local detector circumference and clearly demonstrates the finite event density at small impact radius. The corresponding mask transmission function dependence on recoil kinetic energy $\epsilon_m(K_r)$ is similarly computed for *+2(red), 3(blue), 4(green)* charge states and shown in Figure(4.8d) (markers). Notable non-linearities appear above 20 eV in recoil K_r, which are naturally charge state dependent, as each samples different regions of the mask surface. Overlaid is the finite event density dependent detector efficiency $\epsilon_{fd}(K_r)$ function (line) computed by normalizing the simulated recoil K_r distribution to the steady-state value above 300 eV. Given the form of equation(3.4) it follows that the recoil energy resolution per unit radius $\delta K_r/\delta r \propto (r/TOF^2)$ is linear in hit radius. The inverse proportion to TOF^2 implies the larger charge states with smaller TOF will have a stronger dependency than a smaller charge state with a longer TOF as clearly demonstrated in the simulated $\epsilon_{fd}(K_r)$.

4.1.5 Background Estimation

As discussed above there were two dominant background processes in the recoil-SOE coincidence data stream: the first being from decays which occur uniformly over the apparatus surfaces and throughout the vacuum along the y-axis so as not to produce TOF resonances $I_{Rnd}^{Bck}(K_r)$; the second from decays originating on localized surfaces along the y-axis producing TOF resonances
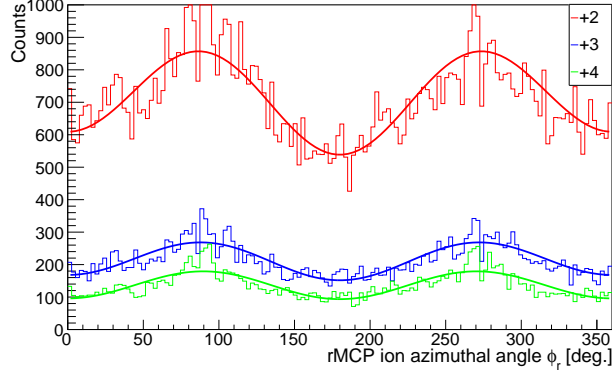
Figure 4.9: Recoil ion azimuthal angular distribution of *+2(red), 3(blue), 4(green)* charge states. Each charge state was fit with the superposition $A + B\cos\phi_r + C\cos^2\phi_r$.

as observed in Figure(4.2), namely from the electrostatic hoops $I^{Bck}_{Hoops}(K_r)$. Both of these distributions have characteristic dependence on the recoil K_r and must be modeled to match theory with the experimental distributions.

The time-random background distribution $I^{Bck}_{Rnd}(K_r)$ is modeled by selecting events well outside of the signal region in TOF window ΔTOF, mapping them uniform randomly into the respective charge state TOF bounds (of width δTOF), then computing the recoil K_r spectrum from its hit coordinates $X' = (x', z', t')$ as above. We then scale this distribution by the ratio of the total integrated intensity of time-random fit backgrounds in Figure(4.2) over δTOF, to that over ΔTOF. In Figure(4.2) the fits chosen for charge states *+3(blue), 4(green)* were linear, as the contribution from the hoops were indistinguishable from time-random distribution. Conversely, the *+2(red)* charge state had notable TOF resonances within δTOF from decays originating on the central hoops #4,5 and must be separated from the time-random background. To do this, two Gaussian's and a step function (dashed) were fit simultaneously to the background in Figure(4.2)(red-line) with the step function defining our time-random event population within the δTOF of the *+2* charge state. With the time-random event distribution constrained for the *+2* charge state the background recoil K_r was similarly obtained.

Background events from the HV hoops are produced when the recoil and SOE are ejected from the surface of the electrode facing the trap and necessarily pass

our event triggers. The proximity of the interior hoop surface along the $\pm z$-axis compared to the surfaces along the $\pm x$-axis with the projected boundary of the rMCP along these axes makes the former the dominant contributor to background events from the hoops. The consequence is an event excess in the recoil angular distribution (about the y-axis) at $90°$ and $270°$ as shown in Figure(4.9) for the *+2(red), 3(blue), 4(green)* charge states, respectively. Although decays from the hoops will be suppressed at smaller detector radii occupied by the larger charge states, the smaller δTOF bounds near the peak in radius vs. TOF required to uniquely identify the charge state makes the hoop backgrounds more significant, as can be seen in the angular distributions of Figure(4.9).

The transverse recoil momentum distributions are shown in Figure(4.10a,b,c) for each of the respective charge states *+2, 3, 4*. The integrated recoil K_r spectra are shown in Figure(4.10d,e,f) over the azimuthally constrained momenta space ϕ_r within $[45°, 135°]$ and $[225°, 315°]$ defining the convolved signal plus hoop background spectra (magenta), while spectra from the remaining momenta space define our signal dominated region (teal) with their difference (black) estimating the hoop background intensity $I_{Hoops}^{Bck}(K_r)$ for the respective charge state. In performing this difference to estimate $I_{Hoops}^{Bck}(K_r)$ we are also by default removing the random background dependence $I_{Rnd}^{Bck}(K_r)$. Overlaid are the smoothed hoop background distributions for the *+2(red), 3(blue), 4(green)* charge states which are used in our analysis below. It will be shown below that such estimates for both $I_{Rnd}^{Bck}(K_r)$ and $I_{Hoops}^{Bck}(K_r)$ provide consistent solutions for ξ_o/ω, independently for each analyzed charge state.

The theoretical recoil kinetic energy distribution dN/dK_r in equation(2.8) must thus be modified as $d\widetilde{N}/dK_r$ to account for the above mentioned detection efficiency effects and our backgrounds in order to compare with the experimentally observed distribution, with $d\widetilde{N}/dK_r$ satisfying

$$\frac{\epsilon_m(K_r)\epsilon_{fd}(K_r)\epsilon_{LR}(K_r)\epsilon_{UD}(K_r)}{NORM} \cdot \frac{dN}{dK_r} + \left[I_{Rnd}^{Bck}(K_r) + I_{Hoops}^{Bck}(K_r) \right]. \qquad (4.5)$$

It should be noted that when fitting equation(4.5) to the data without $I_{Rnd}^{Bck}(K_r)$ there was considerable disagreement between reported values for ξ_o/ω between charge states; well outside the 90% statistical C.L.. Only after including $I_{Rnd}^{Bck}(K_r)$ for each charge state, were the centroids in ξ_o/ω brought back

into agreement, as will be shown below. This lends support that our estimates on $I_{Rnd}^{Bck}(K_r)$ and their kinematic dependencies have been correctly modeled for each charge state.
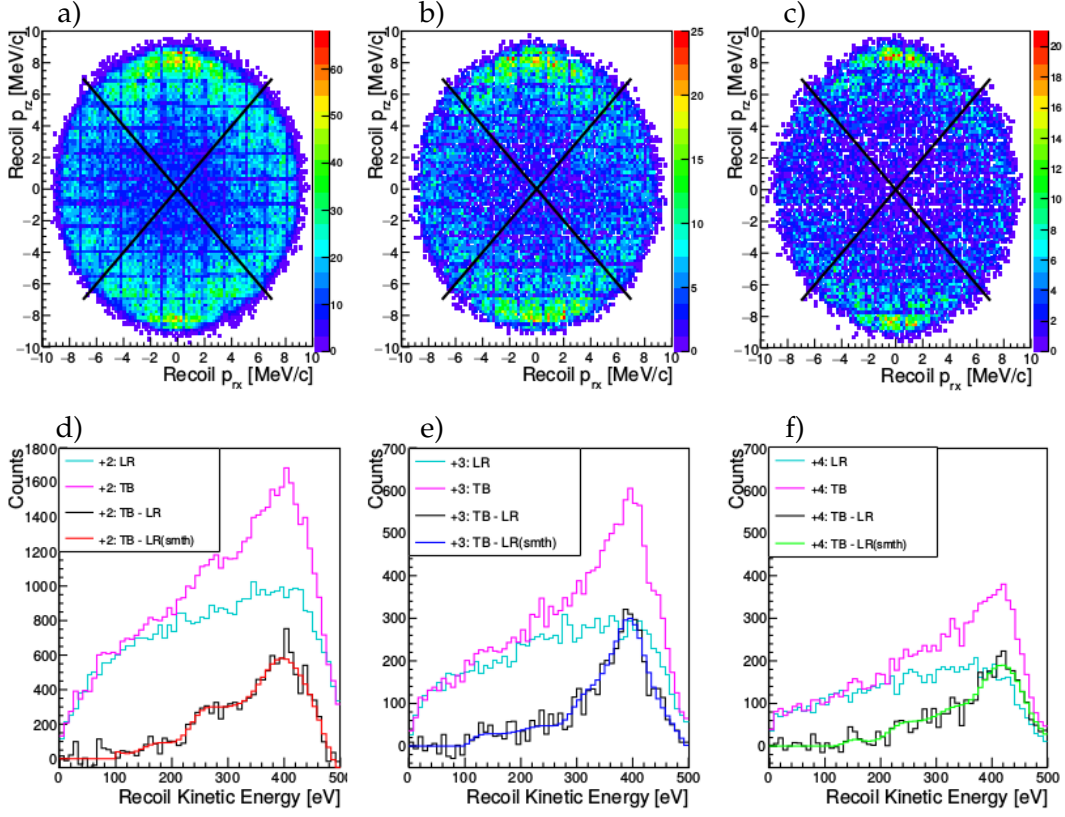
Figure 4.10: a),b),c) Transverse recoil momentum distribution of *+2, 3, 4* charge states (left-right), respectively. d),e),f) Recoil kinetic energy K_r spectra for respective charge states extracted from $\pm x$ quadrants (teal), $\pm z$ quadrants (magenta) with difference (black) an estimate of background levels dominantly from decays from hoop surfaces in the $\pm z$ orientation relative to the $\pm x$ orientation. The overlaid black diagonal lines are the chosen boundaries for such quadrants.

4.1.6 Recoil-SOE Kinematic Spectra and Averaged ξ_o/ω

Integrated $rMCP$-SOE coincident K_r spectra are shown in Figure(4.11a,b) with spectra obtained without corrections from the non-uniform $\vec{E}$-field, and with corrections, respectively for each of the *+2(red), 3(blue), 4(green)* charge states. Notably, the uncorrected spectra are systematically skewed to smaller K_r with the distribution peaking near 380 eV, particularly in the *+2* charge state where it is known that the maximal recoil K_r is 430 eV. Overlaid are the respective backgrounds $I_{Rnd}^{Bck}(K_r)$ as well as $I_{Hoops}^{Bck}(K_r)$ in the case of the fully corrected spectra
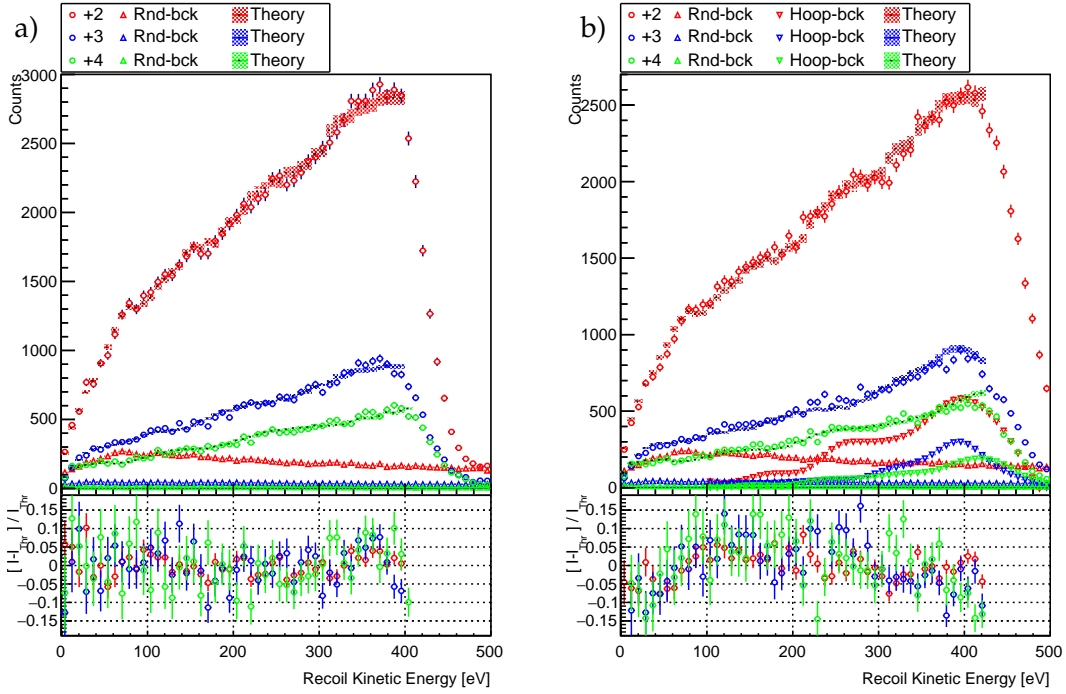
Figure 4.11: Recoil kinetic energy K_r spectrum for *+2(red), 3(blue), 4(green)* charge states a) before non-uniform $\vec{E}$-field ion impact coordinate X' correction (assuming uniform field of $E_y = 998.5$ V/cm), and b) following correction in mapping $X' \to X$ where recoils would traverse such a uniform $\vec{E}$-field. Included are expected random backgrounds and projected hoop backgrounds necessary for $\xi_o/\omega < 0$ model fits. (See Appendix A for $\xi_o/\omega > 0$ model fits.)

for each of the charge states. In the corrected spectra each charge state peaks as expected near 430 eV.

Each of the recoil charge state K_r spectra in Figure(4.11) were fit assuming the modified dependence in equation(4.5). Since the combined branching to excited states is of order 9%, we assume the GS transition is the dominant contributor to the observed recoil K_r spectrum, with the first-forbidden correlation parameter defined in equation(2.22). Two parameter χ^2 minimization was performed by floating the nuclear matrix element ratio ξ_o/ω of the GS transition and arbitrary normalization *NORM* with χ^2/dof distributions plotted in Figure(4.12a,b,c) for the uncorrected K_r spectra (setting $I^{Bck}_{Hoops}(K_r) = 0$), and in Figure(4.12d,e,f) for the fully corrected K_r spectra with boundaries defining the 90% statistical C.L. The fit output is overlaid in Figure(4.11a,b) with residuals displayed at the bottom of each plot for *+2(red), 3(blue), 4(green)* charge states. In the corrected spectra fit residuals show an event excess at low recoil K_r which might result from
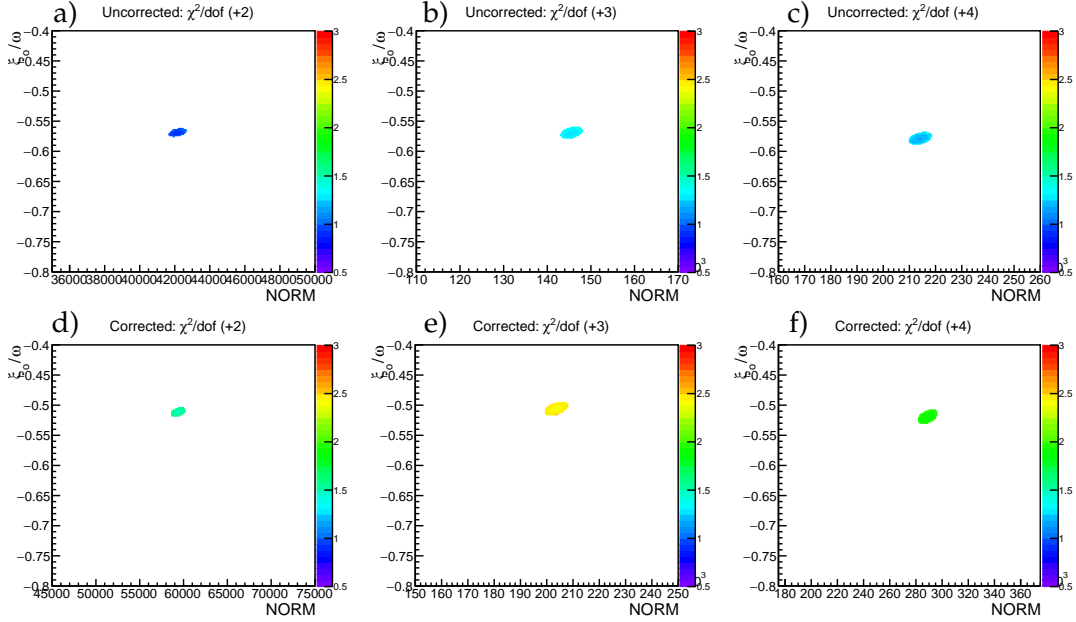
Figure 4.12: χ^2/dof distribution of equation(4.5) fit to recoil K_r spectra in Figure(4.11) after floating the nuclear matrix element ratio $\xi_o/\omega < 0$ and NORM parameters for +2, 3, 4 charge states a),b),c) without non-uniform $\vec{E}$-field corrections, and d),e),f) with non-uniform $\vec{E}$-field corrections in mapping $X' \rightarrow X$. Boundaries of these distributions represent 90 % statistical C.L. for the respective charge state. From the large first-forbidden GS branching we assume the beta-energy dependence in the correlation a_1 parameter of equation(2.22). The range in ξ_o/ω was chosen for comparison of the Recoil-SOE, and the GS isolated Recoil-SOE-SCINT coincident data to see the large change in ξ_o/ω between these channels.

transitions to excited states. Transitions to excited states would produce lower energy beta's and necessarily recoils distributed towards lower K_r. It should be noted that two solutions exist for the nuclear matrix element ratio ξ_o/ω (see supplementary section for $\xi_o/\omega > 0$ solutions) with results at 90% C.L. shown in Table(4.1).

Results from the Recoil-SOE coincident data reveal consistent values for the ξ_o/ω across each charge state at 90% statistical C.L. in Figure(4.12d,e,f) listed in Table(4.1) with mean value $(\overline{\xi/\omega_o})_{RSOE}$ for positive and negative solutions

$$(\overline{\xi_o/\omega})_{RSOE^+} = +0.437 \pm (0.005)_{stat} \pm (0.01)_{sys} \tag{4.6}$$

$$(\overline{\xi_o/\omega})_{RSOE^-} = -0.512 \pm (0.008)_{stat} \pm (0.01)_{sys}. \tag{4.7}$$

As above, this method does not account for transitions to excited states as they can't be experimentally distinguished from those decaying through the GS. A

Table 4.1: Nuclear Matrix Element ratio ξ_o/ω at 90% C.L. from fits of the recoil K_r spectrum of the specified charge state (CS) using equation(4.5) assuming the dominant transition is the First-forbidden GS branch in the Recoil-SOE coincidence. See Appendix A for fit results from $\xi_o/\omega > 0$. (*Non-linear $\vec{E}$-field corrected recoil hit coordinate.)

CS	$\xi_o/\omega < 0$	dof	$\frac{\chi^2}{dof}$	$\xi_o/\omega > 0$	dof	$\frac{\chi^2}{dof}$
+2	$-0.569 + \left(^{+0.006}_{-0.006}\right)_{stat} \pm (0.01)_{sys}$	$48 - 2$	0.91	$+0.465 + \left(^{+0.003}_{-0.003}\right)_{stat} \pm (0.01)_{sys}$	$48 - 2$	0.90
+3	$-0.569 + \left(^{+0.008}_{-0.008}\right)_{stat} \pm (0.01)_{sys}$	$48 - 2$	1.26	$+0.465 + \left(^{+0.005}_{-0.004}\right)_{stat} \pm (0.01)_{sys}$	$48 - 2$	1.24
+4	$-0.579 + \left(^{+0.010}_{-0.008}\right)_{stat} \pm (0.01)_{sys}$	$49 - 2$	1.18	$+0.471 + \left(^{+0.004}_{-0.005}\right)_{stat} \pm (0.01)_{sys}$	$49 - 2$	1.28
+2*	$-0.511 + \left(^{+0.006}_{-0.006}\right)_{stat} \pm (0.01)_{sys}$	$51 - 2$	1.48	$+0.435 + \left(^{+0.003}_{-0.004}\right)_{stat} \pm (0.01)_{sys}$	$51 - 2$	1.39
+3*	$-0.505 + \left(^{+0.008}_{-0.010}\right)_{stat} \pm (0.01)_{sys}$	$51 - 2$	2.41	$+0.434 + \left(^{+0.005}_{-0.005}\right)_{stat} \pm (0.01)_{sys}$	$51 - 2$	2.45
+4*	$-0.519 + \left(^{+0.010}_{-0.010}\right)_{stat} \pm (0.01)_{sys}$	$51 - 2$	1.88	$+0.441 + \left(^{+0.005}_{-0.005}\right)_{stat} \pm (0.01)_{sys}$	$51 - 2$	1.86

similar result was found in ^{134}Sb 0^- to 0^+ first-forbidden rank-0 decay where $\omega \cong 1.8 \cdot \xi_o$ or ($\xi_o/\omega \cong 0.56$) [26], which would have been a surprising result for light nuclei in which $|\xi_o/\omega| \gg 1/3$ with correlation parameter in equation(2.22) (assuming $\gamma_1 \cong 1$) of $a_1 \cong 1$ [17]. One explanation proposed by Siegl & Scielzo was the feeding of a continuum of highly excited states amounting to 17.2(5)% in beta decay strength to obtain a $a_1 \cong 1$ [26]. We attempt to address this question experimentally in the next section, with a preliminary analysis of the correlation parameter a_1 in Recoil-SOE-SCINT coincidence, where we can isolate the decays through the GS.

4.2 Recoil-SOE-SCINT Coincidence

4.2.1 Kinematic Observables and Constraints

Although the recoil-SOE coincident events have the advantage of accepting all recoils in 4π for charge states **+2** and higher in our case, drawbacks exist from the large coincident random backgrounds, and the hoop backgrounds as discussed above. Future position sensitivity of the eMCP/WSA coupled with the highly localized SOE distribution (from their low eV scale energy) will provide additional selection criteria to reject both of these backgrounds, but this is still being incorporated into our DAQ. Recoil-SOE-SCINT triple coincident event channels also provide additional triggers to suppress both backgrounds, though at the expense of restricting the solid angle of accepted events from the solid angle restrictions of the scintillator/collimator, and introducing additional β-detector backgrounds.
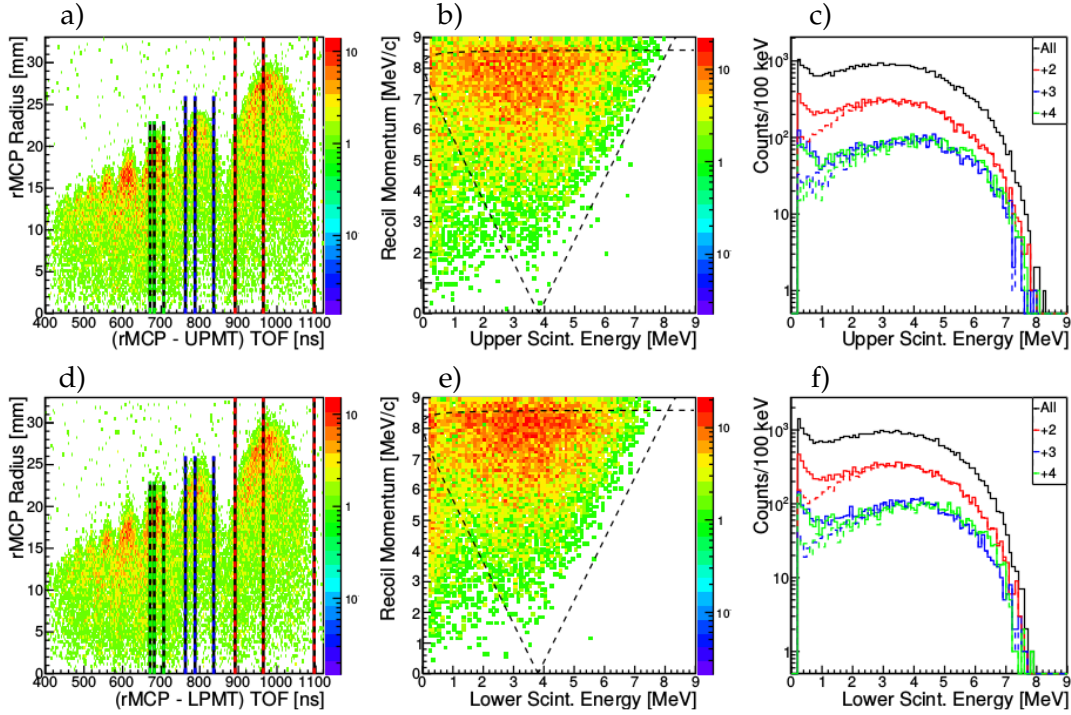
Figure 4.13: Recoil-SOE-SCINT triple coincident event a),c) drift corrected impact radius vs. TOF (Recoil-PMT) spectrum of **+2, 3, 4**, and higher charge states for coincidence with upper, and lower SCINT respectively. Overlaid are the respective TOF bounds for the *+2(red), 3(blue), 4(green)* events. (+2) Recoil momentum vs. scintillator energy are shown in b),e) with overlaid kinematic boundaries for $Q = 8.1$ MeV. Scintillator energy spectra are shown in c),f) with (dashed-line) and without (line) kinematic boundaries applied for indicated charge states.

Triple coincident Recoil-SOE-SCINT events are shown in Figure(4.13) where we have imposed recoil hit selection cuts as discussed above in Section 3.3. The trap drift corrected recoil hit radius vs Recoil-SCINT TOF is shown in Figure(4.13a,d) for coincidence with the upper, and lower scintillator detectors, respectively. Overlaid are the TOF bounds imposed on the *+2(red), 3(blue), 4(green)* charge states in this analysis. The addition of the SOE-SCINT timing gate discussed above was crucial in suppressing random coincident background events. Scintillator event thresholds were set at 200 keV to suppress false scintillator triggers from electronic noise and events which deposit the majority of their energy elsewhere in the apparatus before scattering into the scintillator volume. Again, no cut is made using the DSSD detector in this analysis due to time constraints, but this will provide additional event selection constraint in the final analysis. The non-uniform $\vec{E}$-field corrected recoil momentum plotted as a function of scintillator event energy for the *+2* charge state is shown in Figure(4.13b,e) for

coincidence with the upper, and lower scintillator, respectively. It should be noted that the recoil momentum $\vec{p}_r$ and beta-energy E_β are kinematically dependent from energy and momentum conservation. Assuming $K_r \ll E_\beta, E_\nu$ and from momentum conservation $\vec{p}_r + \vec{p}_\beta + \vec{p}_\nu = 0$ it follows

$$
\begin{aligned}
E_\beta + E_\nu &= E_o = Q + m, \\
p_r^2 &= p_\beta^2 + p_\nu^2 + 2P_\beta p_\nu \cos\theta_{\beta\nu}
\end{aligned}
\tag{4.8}
$$

where since the recoil momenta are bounded by $|p_\beta - p_\nu| < p_r < |p_\beta + p_\nu|$ it can be shown[15] the constraints on the accessible beta energy E_β are

$$
\frac{(p_r - E_o)^2 + m^2}{2(p_r - E_o)} < E_\beta < \frac{(p_r + E_o)^2 + m^2}{2(p_r + E_o)}.
\tag{4.9}
$$

Overlaid in Figure(4.13b,e) are the kinematic boundaries of equation(4.9) assuming a $Q = 8.1$ MeV endpoint for the dominant GS transition. Clearly, a significant fraction of events particularly at small E_β and recoil momenta lie outside the kinematic boundaries for the GS transition. The event population outside this region is populated both by decays to excited states, as well as incorrect evaluation of E_β from bremsstrahlung and betas scattering depositing non-negligible amounts of energy within the DSSD, or other regions of the apparatus volume.

Scintillator spectra for the upper, and lower detectors are shown in Figure(4.13c,f) for the *+2(red), 3(blue), 4(green)* charge states both with (dashed-lines) and without (solid-lines) the kinematic boundaries applied to the data. The kinematic bounds demonstrate a significant suppression of pedestal type events where low energy beta's deposit the majority of their energy in the DSSD and other volumes, with the remaining beta energy sufficient to fire the scintillator PMT. The kinematic bounds, however, assume infinite detector precision and efficiency, which is impractical where clearly a small subset of events with large recoil momentum fall just outside the boundaries from finite recoil momentum resolution. Additionally, a systematic deviation in the maximum SCINT energy from the expected kinematic bounds is seen for coincidences in both upper and lower scintillator, suggesting that their calibration is not fully optimized.
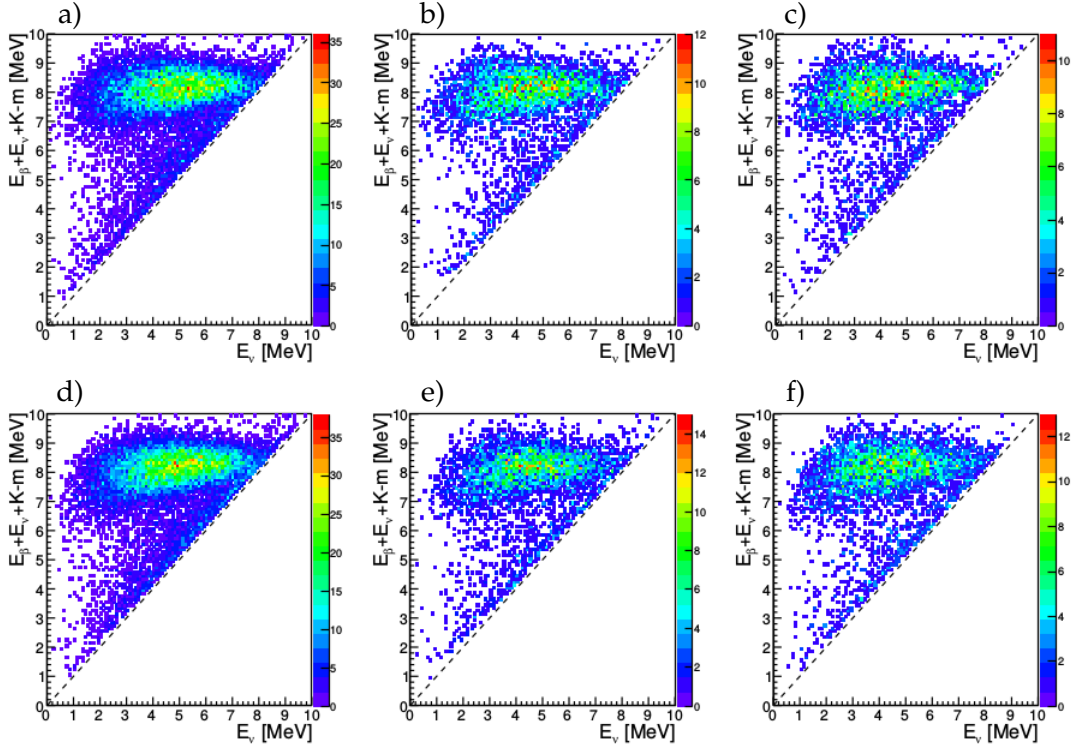
Figure 4.14: Recoil-SOE-SCINT coincident Q_{exp}-value vs. reconstructed anti-electron neutrino energy E_ν spectrum utilizing the a),b),c) Upper and d),e),f) Lower beta scintillator events within the respective +2, 3, 4 recoil charge state TOF bounds shown in Figure(4.13a,d).

4.2.2 Reconstructed E_ν and Q_{exp}-value Distributions

With the known initial recoil momentum $\vec{p}_r$ and taking the beta momentum to be entirely along either the $\pm z$-axis, the neutrino momentum and thus its energy E_ν (assuming it is massless for our purposes) can be reconstructed as per equation(3.9), along with the Q_{exp}-value in equation(3.11). The distribution of Q_{exp}-value vs. E_ν are shown for +2, 3, 4 charge states using the upper scintillator in Figure(4.14a,b,c), and lower scintillator in Figure(4.14d,e,f), respectively. The resonance like feature centered on a Q-value of 8.1 MeV correspond to nuclear β-decay transitioning through the GS branch. The sparse event distribution with smaller Q_{exp}-values, which are correlated with smaller E_ν, correspond to β-decays through the excited states since there is less energy available to the neutrino. Events along the $Q_{exp} = E_\nu$ line result from incorrectly reconstructed E_ν and thus Q_{exp} from incorrect reconstruction of the beta's energy, and incorrect selection of the recoil event. Incorrect reconstruction of the beta's energy

can result from energy deposition within the DSSD, scattering from the colli-mator or other non-active volumes, or through bremsstrahlung photons which easily escape the low Z plastic scintillators. Similarly, our event selection in this analysis accepts only the first recoil into the DAQ and thus could lead to misidentification of the recoil and its momentum. The result is a unitary corre-lated random spread of events along the line $Q_{exp} = E_\nu$. Raising the scintillator thresholds greatly suppress these events uniformly along $Q_{exp} = E_\nu$, although at the expense of losing sensitivity to the neutrinos with largest E_ν.
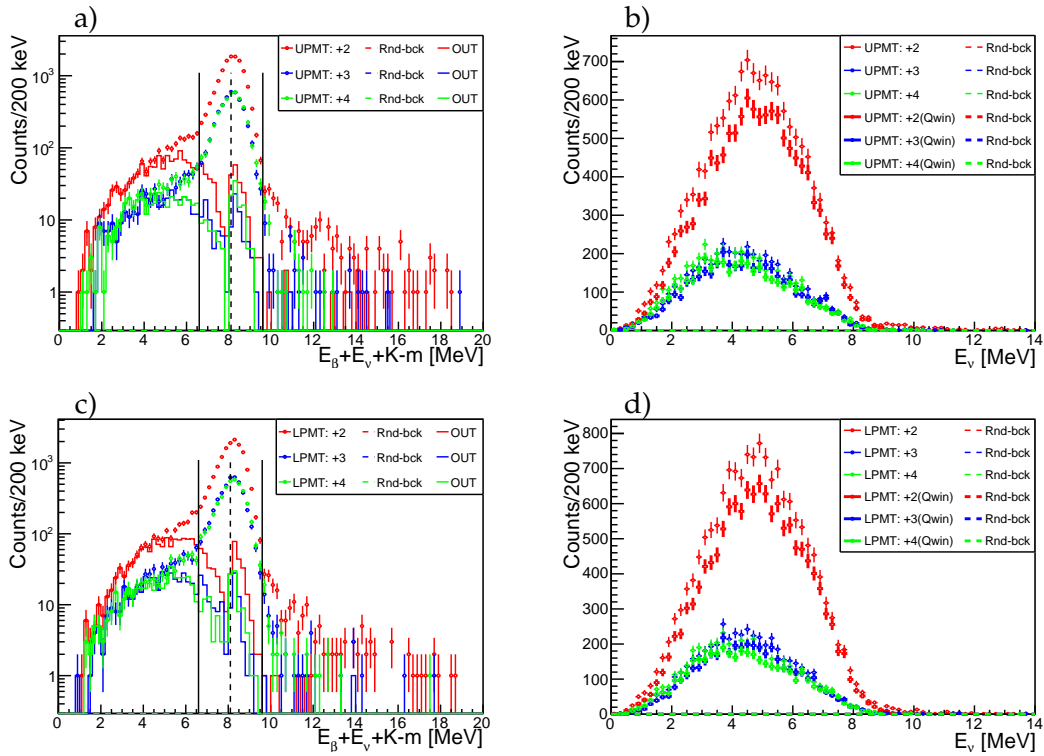
Figure 4.15: Recoil-SOE-SCINT triple coincident events with transition Q_{exp}-value distri-butions of the *+2(red), 3(blue), 4(green)* charge states with beta's coincident in the a) Upper, and c) Lower scintillators, respectively (See Appendix A for linear scaled plots). Overlaid are the time random coincident backgrounds (dashed-lines), and kinematically forbidden events assuming $Q = 8.1$ MeV (solid-lines) for the respective charge states. Correspond-ing anti-electron neutrino energy spectra E_ν are shown in b), and d) both with kinemati-cally constrained domain and events within 1.5 MeV of $Q = 8.1$ MeV GS transition (bold-markers), and without such bounds (markers) are shown for each charge state. Expected time random coincident background event distribution without the above bounds are over-laid for each charge state (dashed-lines).

Projections in Q_{exp}-value of the 2D histograms in Figure(4.14) are shown in Figure(4.15a,c) for *+2(red), 3(blue), 4(green)* charge states (markers) and time random events (dashed-lines) for coincidences with the upper, and lower scintillator, respectively. Again a sharp resonance at the $Q = 8.1$ MeV correspond to decays through the GS transition with low energy tail corresponding to transitions to excited states and otherwise incorrectly reconstructed events. The breadth of the GS resonance is in part due to the energy resolution of our plastic scintillators, but also the assumption that the beta's have their momenta entirely along the z-axis, which is only approximately true. The beta hit position (and energy deposition) in the DSSD will aid in improving the beta momentum resolution and thus the spread in the GS Q_{exp}-value distributions in the final analysis. Overlaid are the Q_{exp}-value distributions for events that fall outside of our kinematic boundaries assuming $Q = 8.1$ MeV for the GS transition, which amount to significant fractions of the low energy Q_{exp}-value tail for each charge state. The remaining events in the tail of the Q_{exp}-value distribution that are within our kinematic boundaries are dominantly populated by transitions to lower energy excited states.

Similarly, projections in E_ν of the 2D histograms in Figure(4.14) for each charge state are shown in Figure(4.15b,d) (solid-lines) with time-random coincident backgrounds (dashed-lines) for coincidence with the upper, and lower scintillators, respectively. A broad distribution in E_ν is observed out to ~ 8.7 MeV from the 3-body phase space of the weak decay kinematically constrained to $E_\nu < Q_{exp}$ (when $E_\beta \sim m$) with deviations largely due to detector resolution effects. Applying a Q_{exp}-value gate on events within 1.5 MeV of the $Q = 8.1$ MeV GS transition, along with our kinematic boundaries defined above, we can isolate the respective population in E_ν with results overlaid for each charge state (bold-lines) for coincidence with respective scintillator. Notably, in isolating the neutrinos from GS beta transition, the remaining events are correlated with lower energy E_ν as one would expect from feeding excited states, where there is less energy available to the beta's, and necessarily the neutrinos.

The transverse recoil momentum distribution of decays within our Q_{exp}-value gate and kinematic boundaries for coincidence with the upper, and lower scintillator are shown in Figure(4.16a,c), respectively. The small opening angle of the scintillator/collimator constrain, naturally, the accessible momentum space of the recoil which is dominantly ejected opposite to the respective β-scintillator.
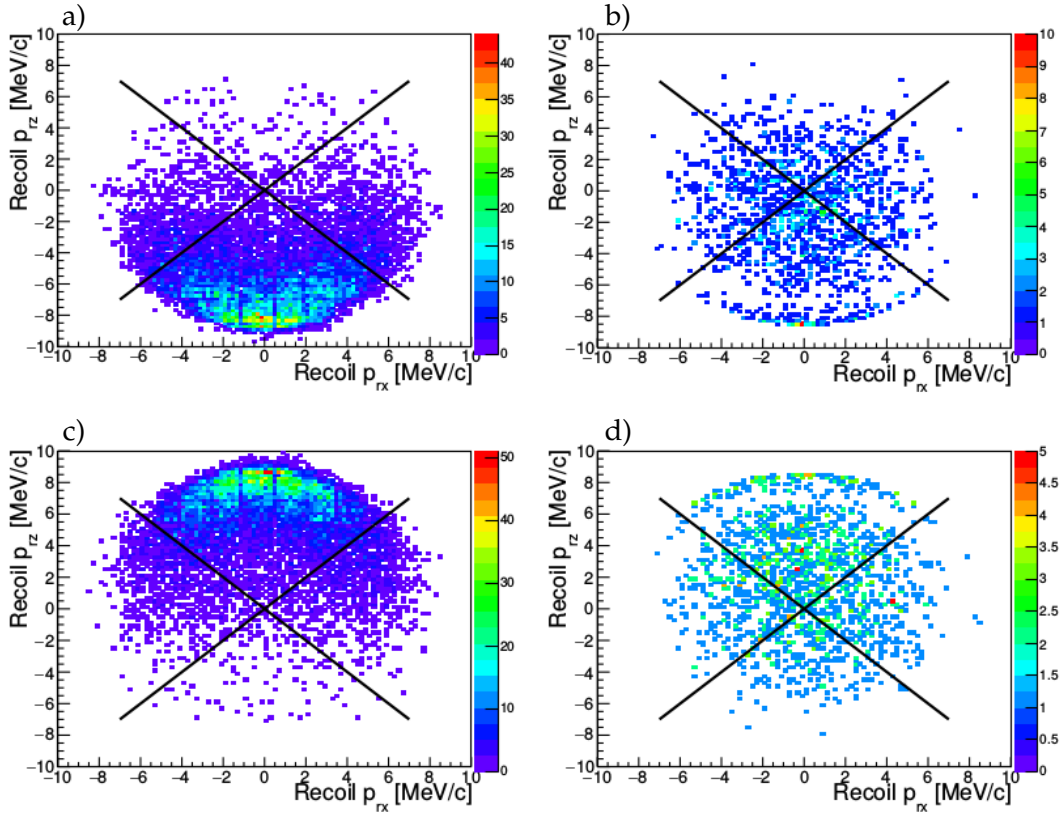
Figure 4.16: a),d) Recoil-SOE-SCINT coincident transverse recoil momentum distribution of +2 charge state within TOF bounds shown in Figure(4.13a,d) for event subset within ±1.5 MeV of the GS transition Q_{exp}-value centered at $Q = 8.1$ MeV, and within the defined kinematic boundaries. The transverse momentum distribution of events outside the kinematic boundaries are shown in b),d) for coincident events with the Upper, and Lower scintillator, respectively.

Particularly, note the absence of events with recoil momenta in the direction of the respective β-scintillators. Beta's from decays originating on the central electrostatic hoop surfaces along the $\pm z$-axis still have line-of-sight access to both the upper and lower scintillators, though slightly different solid angles. If decays from the hoops were present in this Recoil-SOE-SCINT triple coincident channel there should be a symmetric event excess at large transverse momentum along the $\pm z$-axis as we inferred above in the Recoil-SOE coincident channel. The absence of events with large transverse momenta aligned with the respective β-scintillator indicates that such a background resulting from decays off the hoops is greatly suppressed in Recoil-SOE-SCINT triple coincident channel with a timing gate applied to the SOE-SCINT TOF as above. Recall that in the Recoil-SOE-SCINT triple coincident channel the recoil TOF was taken

between the β-scintillator and the recoil, so naturally hoop backgrounds will be suppressed in this event type due to the limited solid angle of the scintillator/collimator compared to the Recoil-SOE coincidence which accepts events in 4π. The transverse recoil momentum distribution outside the kinematic bounds are shown in Figure(4.16b,d), and dominantly populate lower transverse recoil momentum (smaller K_r) resulting from feeding excited states.
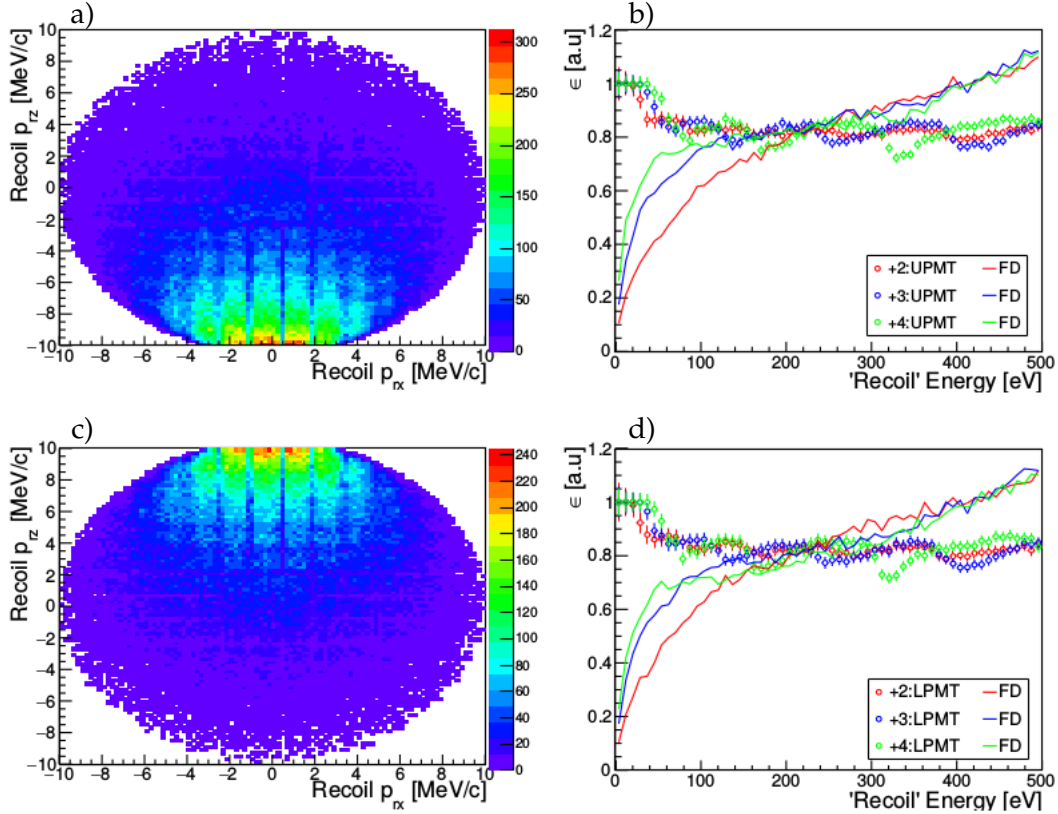
Figure 4.17: Simulated transverse recoil momentum distribution from a point-like source with encoded trap drift, within the TOF bounds, and with conical restrictions placed on the β-solid angle (22°) defined by our collimator geometry for coincidence with the a) upper, and c) lower scintillators, respectively. Corresponding mask transmission functions $\epsilon_m(K_r)$ (markers) and finite event density $\epsilon_{fd}(K_r)$ are shown for +2(red), 3(blue), 4(green) charge states for coincidence with the b) upper, d) lower scintillator, respectively.

4.2.3 GS Transition ζ_0/ω

With the GS transition isolated above we can extract the first-forbidden nuclear matrix element ratio ζ_0/ω from the recoil K_r spectrum of each charge state. In order to fit the experimental recoil K_r spectrum we similarly employ equation(4.5), but for this channel justifiably assume the background contribution

from the hoops is small. Since the recoils sample a restricted subset of momentum space due to the restrictions on the beta momentum space, we must incorporate this into the evaluation of $\epsilon_m(K_r)$, and $\epsilon_{fd}(K_r)$. To do this we perform a crude simulation of a 3-body decay from a point-like source, with the outgoing beta restricted to uniformly populate the conical momentum space accessible assuming the $22°$ opening angle restriction by the β-collimator. The 'neutrino' energy is kinematically restricted to $E_\nu = E_o - E_\beta$, but with momenta allowed to occupy 4π in this simple simulation. The recoil momentum is then generated simply from non-relativistic momentum conservation. Again, the trap drift present in the experiment is encoded in the simulated decay along with appropriate recoil TOF bounds in Figure(4.13a,d) with the transverse momentum distribution shown in Figure(4.17a,c) for coincidence with the upper, and lower scintillator, respectively. Similarly, the trap drift smears out the mask pattern in the transverse momentum space with the recoils dominantly populating the phase space opposite to the respective detector and similar to the distributions seen in our data in Figure(4.16a,c), respectively.
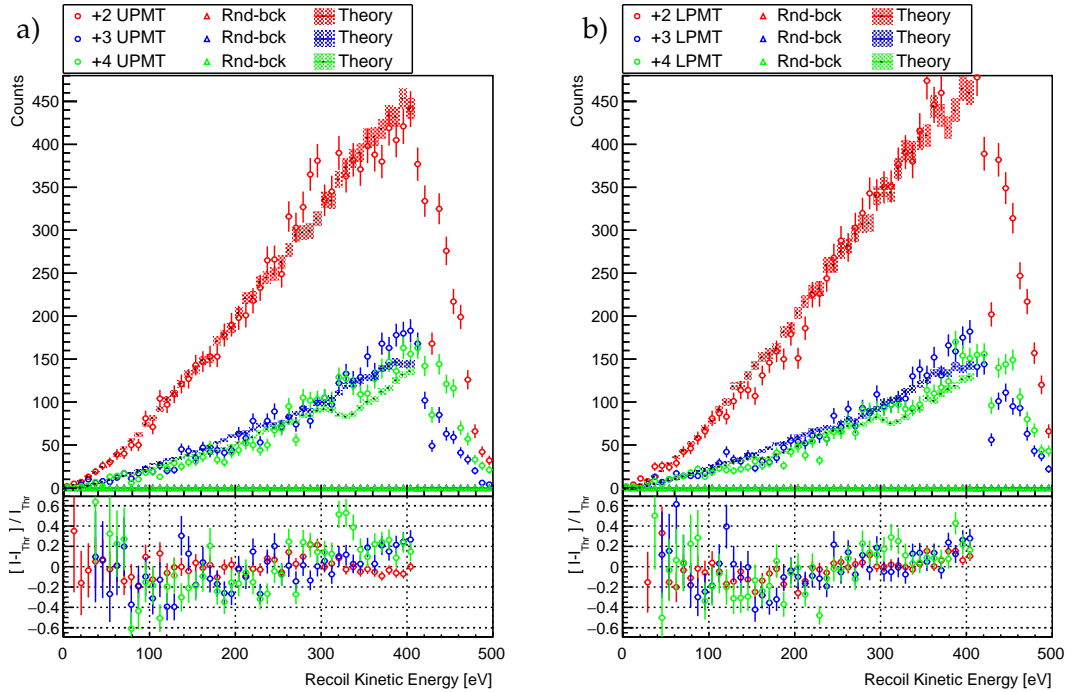
Figure 4.18: Recoil K_r spectra for GS Recoil-SOE-SCINT coincident events in charge state *+2(red), 3(blue), 4(green)* with beta's coincident with the a) upper, and b) lower scintillator, respectively. GS events were isolated after applying kinematic bounds, TOF bounds, and gating in Q_{exp}-value on the events within 1.5 MeV of the 8.1 MeV grounds state transition. Overlaid are the time random coincident background's (dashed-lines) for the respective charge states along with model fits taking $\xi_o/\omega < 0$.

The recoil transmission efficiency $\epsilon_m(K_r)$ was similarly computed as the ratio of simulated recoil K_r spectrum of events incident on the rMCP/mask to that incident rMCP alone for charge states *+2(red), 3(blue), 4(green)* (markers) shown in Figure(4.17b,d) for coincidence with the upper and lower scintillator, respectively. The trap drift requires $\epsilon_m(K_r)$ to be independently determined for coincidences with the upper and lower scintillator from the now broken symmetry of the imprinted mask pattern observed by each recoil population. The restrictions on the recoil phase space also result in extremely low event rates with transverse momenta oriented with the respective scintillator detector, which we parameterize as $\epsilon_{fd}(K_r)$ by scaling the simulated K_r spectra incident on the rMCP alone by the value obtained at maximal recoil K_r of 430 eV. The absolute scaling of $\epsilon_{fd}(K_r)$ is not relevant given that the normalization *NORM* in equation(4.5) is a floating parameter. The non-linear drop in efficiency towards zero recoil K_r, similar to those in Recoil-SOE coincidence above, again results from the finite event density at low recoil radius for each of the respective charge states. The near-linear dependence in $\epsilon_{fd}(K_r)$ out to large K_r results from the restricted phase space on the beta, and necessarily the recoil.

Given the limited statistics in the triple coincidence and the recoil solid angle restrictions above, we assume the relative rMCP efficiency functions above $\epsilon_{LR}(K_r)$ and $\epsilon_{UD}(K_r)$ determined from the Recoil-SOE coincidences to be largely intrinsic to the rMCP detector, and apply them in our evaluation of equation(4.5) for the recoil K_r spectra in Recoil-SOE-SCINT coincidence. Finally, for Recoil-SOE-SCINT coincidences within the *+2(red), 3(blue), 4(green)* TOF bounds, we apply the above kinematic boundaries and gate on events within 1.5 MeV of the 8.1 MeV *Q*-value, producing the recoil K_r spectra (markers) shown in Figure(4.18a,b) for coincidences with the upper, and lower scintillator, respectively. Random coincidence backgrounds $I_{Rnd}^{Bck}(K_r)$ were similarly computed as above for each charge state and overlaid, which were significantly reduced following the mentioned SCINT-SOE TOF cuts. Assuming negligible contributions from $I_{Hoops}^{Bck}(K_r)$ as argued above, the spectra were fit with equation(4.5) floating the nuclear matrix element ratio ξ_o/ω and arbitrary normalization *NORM* for charge states *+2, 3, 4* with resulting χ^2/dof shown in Figure(4.19a,b,c) for coincidence with the upper scintillator, and lower scintillator in Figure(4.19d,e,f), respectively. Again, the boundary of the χ^2/dof distribution defines the 90 % statistical C.L. The solutions for ξ_o/ω are tabulated in Table(4.2) with distributions and residuals shown in Figure(4.18). (See appendix for similar plots above

with positive solutions of ξ_o/ω).
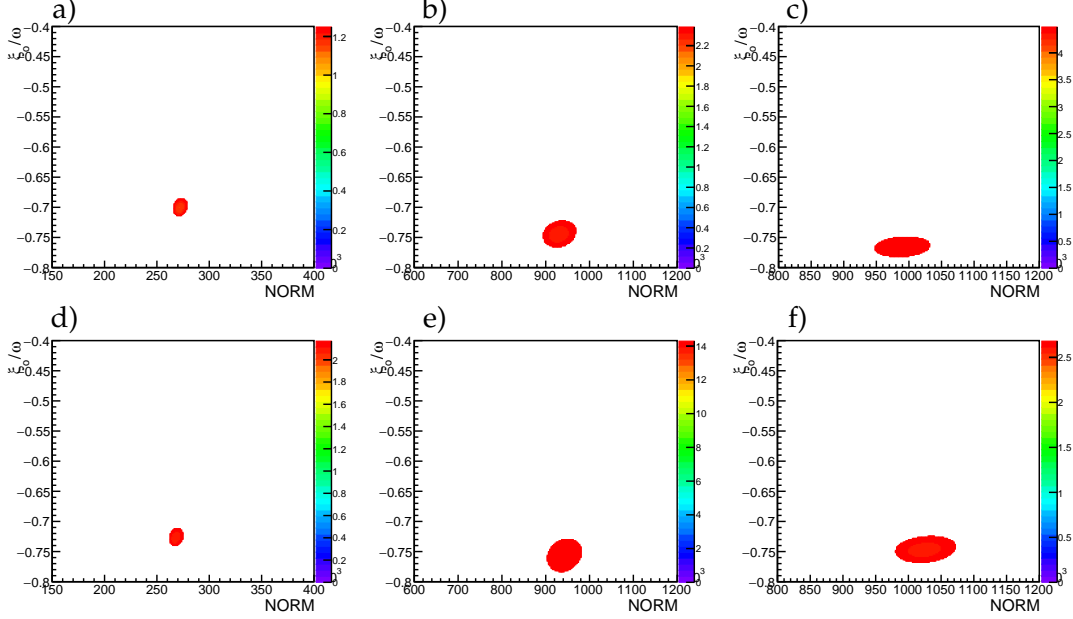
Figure 4.19: χ^2/dof distribution of equation(4.5) fit to recoil GS K_r spectra in Figure(4.18) after floating the nuclear matrix element ratio $\xi_o/\omega < 0$ and NORM parameters for +2, 3, 4 charge states with beta coincident with the a),b),c) Upper, and d),e),f) Lower, scintillators, respectively. Boundaries of these distributions represent 90 % statistical C.L. for the respective charge state. The range in ξ_o/ω was chosen for comparison of the Recoil-SOE, and the GS isolated Recoil-SOE-SCINT coincident data to see the large change in ξ_o/ω between these channels.

Consistent values for the GS isolate, first-forbidden rank-0 nuclear matrix element ratio ξ_o/ω, across each charge state and each scintillator are seen in table(4.2) with mean value using the upper scintillator (UPMT)

$$(\overline{\xi_o/\omega})_{BRSOE^+} = +0.540 \pm (0.007)_{stat} \pm (0.01)_{sys} \qquad (4.10)$$

$$(\overline{\xi_o/\omega})_{BRSOE^-} = -0.736 \pm (0.016)_{stat} \pm (0.01)_{sys}, \qquad (4.11)$$

and lower scintillator (LPMT)

$$(\overline{\xi_o/\omega})_{BRSOE^+} = +0.542 \pm (0.008)_{stat} \pm (0.01)_{sys} \qquad (4.12)$$

$$(\overline{\xi_o/\omega})_{BRSOE^-} = -0.742 \pm (0.020)_{stat} \pm (0.01)_{sys}. \qquad (4.13)$$

We note that even though the $\chi^2/dof > 1$ the 90% statistical C.L. bounds on $\xi_o/\omega > 0$ are more then half those for $\xi_o/\omega < 0$, which may suggest the true

Table 4.2: Nuclear Matrix Element ratio ξ_o/ω at 90% C.L. from fits of the recoil K_r spectrum of the specified charge state using equation(4.5) from decays through the First-forbidden GS branch in the Recoil-SOE-SCINT coincidence. See Appendix A for fit results from $\xi_o/\omega > 0$. (*Non-linear $\vec{E}$-field corrected recoil hit coordinate.)

C.S.	SCINT	$\xi_o/\omega < 0$	dof	$\frac{\chi^2}{dof}$	$\xi_o/\omega > 0$	dof	$\frac{\chi^2}{dof}$
+2*	UPMT	$-0.699 + \left(^{+0.012}_{-0.014}\right)_{stat} \pm (0.01)_{sys}$	$49-2$	1.15	$+0.525 + \left(^{+0.005}_{-0.006}\right)_{stat} \pm (0.01)_{sys}$	$49-2$	1.16
+3*	UPMT	$-0.743 + \left(^{+0.020}_{-0.022}\right)_{stat} \pm (0.01)_{sys}$	$49-2$	2.28	$+0.544 + \left(^{+0.009}_{-0.008}\right)_{stat} \pm (0.01)_{sys}$	$49-2$	2.36
+4*	UPMT	$-0.765 + \left(^{+0.014}_{-0.016}\right)_{stat} \pm (0.01)_{sys}$	$49-2$	4.38	$+0.553 + \left(^{+0.006}_{-0.006}\right)_{stat} \pm (0.01)_{sys}$	$49-2$	4.20
+2*	LPMT	$-0.725 + \left(^{+0.012}_{-0.014}\right)_{stat} \pm (0.01)_{sys}$	$49-2$	2.07	$+0.535 + \left(^{+0.006}_{-0.005}\right)_{stat} \pm (0.01)_{sys}$	$49-2$	2.00
+3*	LPMT	$-0.755 + \left(^{+0.024}_{-0.028}\right)_{stat} \pm (0.01)_{sys}$	$49-2$	14.2	$+0.548 + \left(^{+0.012}_{-0.011}\right)_{stat} \pm (0.01)_{sys}$	$49-2$	14.2
+4*	LPMT	$-0.745 + \left(^{+0.020}_{-0.022}\right)_{stat} \pm (0.01)_{sys}$	$49-2$	2.58	$+0.544 + \left(^{+0.008}_{-0.008}\right)_{stat} \pm (0.01)_{sys}$	$49-2$	2.42

value of $\xi_o/\omega > 0$. This follows from the form of the correlation parameter in equation(2.22) having an interference term between the two nuclear matrix elements, which is sensitive to their relative signs in principle. We note that this is surprisingly/coincidently consistent with the ^{134}Sb ($\xi_o/\omega \cong 0.56$) measured at ANL [26], though this experiment could not rule out contamination from transitions to excited states of the daughter. Evidently, even with the GS isolated events in ^{92}Rb, the hypothesis that $|\xi_o/\omega| \gg 1/3$ [17] is inconsistent with our results. It should be noted that even when gating on Q_{exp}-value for the GS transition, as shown in Figure(4.15a,c), there remains a population of transitions to excited states, albeit small, within such bounds with recoil K_r necessarily skewed towards small values. Such an excess of low energy recoils above an already small population from the GS events (with necessarily small uncertainties), may skew the fit to smaller magnitudes of ξ_o/ω.

4.3 Recoil-SOE-SCINT Coincidence GS Transition ξ_o/ω

The results for the nuclear matrix element ratio ξ_o/ω in the Recoil-SOE-SCINT coincidence from decays through the GS presented in Table(4.2) are notably different from the those in the Recoil-SOE coincidence in Table(4.1) assuming the first-forbidden rank-0 form of the correlation parameter $a_1(W)$ in equation(2.22). The correlation parameter $a_1(W)$ however diverges as $W \to 1$. The scaling coefficient $a_1(W) \cdot (v/c)$ of the $\cos\theta$ dependency in the convolution function equation(2.18) is bounded by ± 1, and seems more appropriate to investigate here. Assuming the values for nuclear matrix element ratio ξ_o/ω at 90 % statistical C.L. in Table(4.1) for the Recoil-SOE coincident events $a_1(W) \cdot (v/c)$ was plotted in Figure(4.20) in a) for $\xi_o/\omega > 0$, and c) for $\xi_o/\omega < 0$, respectively.

Asymptotic limits on the correlation parameter show $a_1(W \to W_o)^{RSOE^+}_{RSOE^-} \to^{0.30}_{0.36}$, respectively, over multiple charge states. The bounds on $a_1(W) \cdot (v/c)$ after gating on events decaying through the GS in Recoil-SOE-SCINT coincidences are shown in Figure(4.20) in b) for $\xi_o/\omega > 0$, and d) for $\xi_o/\omega < 0$, respectively. Asymptotic limits on the correlation parameter show $a_1(W \to W_o)^{BRSOE^+}_{BRSOE^-} \to^{0.50}_{0.58}$, respectively, over multiple charge states. Considerable deviations in the correlation a_1 are thus evident in the Recoil-SOE, and Recoil-SOE-SCINT coincident event streams. Without being able to isolate decays through the GS in the Recoil-SOE coincidence, decays to the continuum of highly excited beta transitions necessarily reduces the energy available to the recoil and populate small recoil K_r on average. In populating small values of K_r from feeding excited states in the Recoil-SOE coincidence the result will be a reduction in the average correlation parameter magnitude compared to that from decays through the GS in the Recoil-SOE-SCINT coincidence as observed here. Additionally, the excited states have unconstrained and differing correlation parameters from those of the GS transition, which will also distort the recoil K_r spectrum.

4.4 Summary of Results

We have shown consistent results for the rank-0 nuclear matrix element ratio ξ_o/ω across the +2, 3, 4 charge states in both the Recoil-SOE coincident dataset in Table(4.1), and triple coincident Recoil-SOE-SCINT dataset in Table(4.2). The corresponding first-forbidden rank-0 E_β dependent correlation parameter bounds at 90% statistical C.L. are shown in Figure(4.20) assuming the beta energy dependence $a_1(W)$ of equation(2.22). A significant deviation between the mean nuclear matrix element ratio $\overline{\xi_o/\omega}$ in Recoil-SOE coincidence

$$(\overline{\xi_o/\omega})_{RSOE^+} = +0.437 \pm (0.005)_{stat} \pm (0.01)_{sys} \tag{4.14}$$

$$(\overline{\xi_o/\omega})_{RSOE^-} = -0.512 \pm (0.008)_{stat} \pm (0.01)_{sys}. \tag{4.15}$$

and that of the Recoil-SOE-SCINT coincidence after gating on Q_{exp}-value within 1.5 MeV of the 8.1 MeV Q-value

$$(\overline{\xi_o/\omega})_{BRSOE^+} = +0.541 \pm (0.008)_{stat} \pm (0.01)_{sys} \tag{4.16}$$

$$(\overline{\xi_o/\omega})_{BRSOE^-} = -0.739 \pm (0.018)_{stat} \pm (0.01)_{sys} \tag{4.17}$$

is observed. Interestingly, the bounds on the positive solutions for $\overline{\xi_o/\omega}$ at 90% statistical C.L. appear to be a factor of 2x smaller than the negative solutions, suggesting $\xi_o/\omega > 0$, as we have sensitivity to the relative sign of the nuclear matrix elements from the interference term in $a_1(W)$ of equation(2.22).
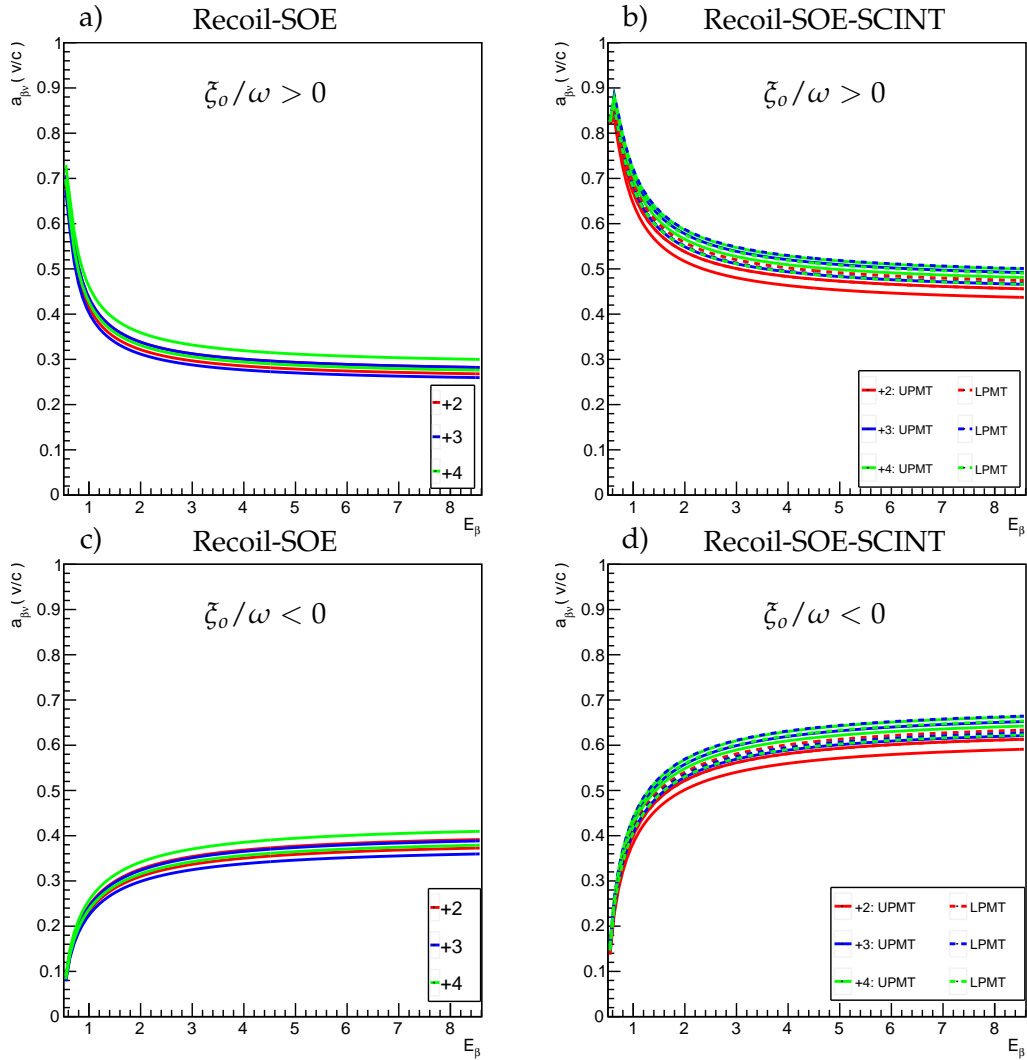
Figure 4.20: First-forbidden (rank-0) beta-neutrino correlation function product $a_1(E_\beta) \cdot (v/c)$ in equation(2.22) vs. E_β from (90 % C.L.) bounds set in Table(4.1) for Recoil-SOE events in a,c) and GS isolated Recoil-SOE-SCINT coincident events from limits set in Table(4.2) in b,d) for $\xi_o/\omega > 0$, and $\xi_o/\omega < 0$, respectively. In (b,d) the solid and dashed line bounds are from event streams coincident with the Upper and Lower scintillators.

Chapter 5

Conclusion and Outlook

5.1 Recoil-SOE Coincidence

5.1.1 Conclusion

The theoretical neutrino energy spectrum for any 0^- to 0^+ decay depends on ξ_0/ω [21], and our determination of this ratio for the GS transition might end up better defining the neutrino energy spectrum than our direct measurement. Our result would be a unique nonzero measurement of ω in these high-Z fission products, a quantity very difficult to calculate because of its dependence on the spatial tails of the wave-function. If ω is finite in general in 0^- to 0^+ decays, the neutrino energy spectrum would change for all such transitions.

In the β^- decay of ^{92}Rb it is shown that in Recoil-SOE coincidence, the positive/ negative solutions of the nuclear matrix element ratio $(\overline{\xi_o/\omega})^{RSOE^+}_{RSOE^-} = {}^{+0.437}_{-0.512} \pm \binom{0.005}{0.008}_{stat} \pm \binom{0.01}{0.01}_{sys}$ and correlation parameter $a_1(W \to W_o) \to^{0.30}_{0.36}$. With $|\overline{\xi_o/\omega}| < 1$, and $|a_1| < 1$, our results are inconsistent with theoretical predictions for rank-0 first-forbidden transitions in which $|\xi_o/\omega| \gg 1/3$, and $|a_1(W \to W_o)| = 1$ [17]. These results are similar to those obtained in the ^{134}Sb dominant first-forbidden $0^- \to 0^+$ rank-0 GS decay, in which they found $\xi_o/\omega \cong 0.56$ and $a_1 = 0.47$, but without isolating decays through the GS [26]. The authors of [26] attributed this difference to the feeding of excited states. They cite a shell model calculation in which $\xi_o >> \omega$, and cite a version of Siegerts theorem applied to forbidden decays. In the case of ^{92}Rb, the disagreement in $\overline{\xi_o/\omega}$ of the Recoil-SOE coincident data with theory would be understandable, as the excited state transitions are indistinguishable from decays through the GS. Interestingly, however, even in the Recoil-SOE-SCINT coincidence in which the GS events are isolated in Q_{exp}-value, we find $(\overline{\xi_o/\omega})^{BRSOE^+}_{BRSOE^-} = {}^{+0.541}_{-0.739} \pm \binom{0.008}{0.018}_{stat} \pm \binom{0.01}{0.01}_{sys}$ with $a_1(W \to W_o) \to^{0.50}_{0.58}$, where similarly $|\xi_o/\omega| <$

1, and $|a_1(W \rightarrow W_o)| < 1$. It should be noted there remains a small population of excited state events which are within the Q_{exp}-value gate, which may skew the fits in the Recoil-SOE-SCINT dataset to smaller magnitudes in ξ_o/ω and a_1. In the Recoil-SOE-SCINT coincident dataset we also reconstruct the anti-electron neutrino spectrum E_ν following gating on decays through the GS, which will be compared with simulations in the future.

5.1.2 Outlook

In the future analysis, the addition of the DSSD detectors will further improve our 3-momentum resolution of the betas, and correspondingly improve our energy resolution of the Q_{exp}-value and E_ν. In the analysis above we have utilized a coarse spatial calibration of the rMCP, and we will perform high-resolution spatial calibrations in the final analysis to further improve our recoil momentum resolution, and corresponding resolution of Q_{exp}-value and E_ν. GEANT-4 simulations will be necessary to model the Q_{exp}-value of decays through the GS, and expected background levels from inner, and outer bremsstrahlung, and otherwise miss-identified events. Once this is complete the population of decays to excited states can be separated from the data, allowing us to constrain the GS branching ratio.
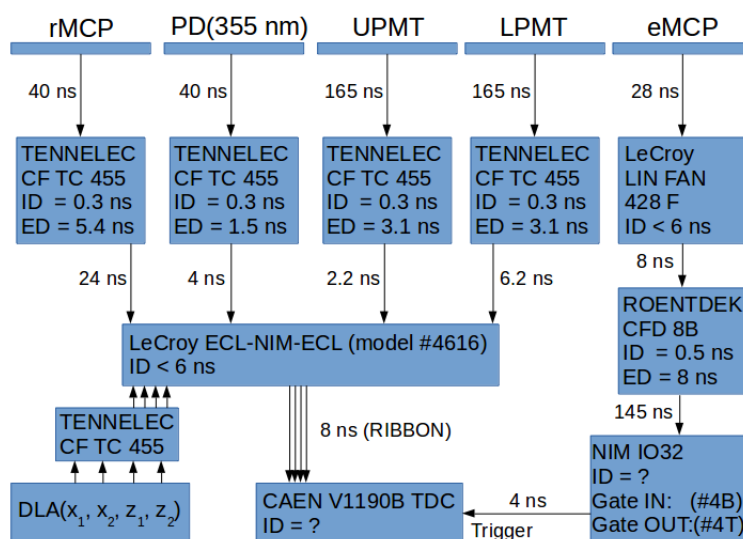
Appendix A

Appendices

Figure A.1: TRINAT DAQ timing setup with indicated delays into the acquisition. Strip detectors are not shown nor are the QDC data-streams from the rMCP, Wedge and Strip Anode (WSA) backing the eMCP, or scintillators. Only relative timing differences are needed for xz-recoil hit position reconstruction of the delay-line-anode (DLA) so delay-line lengths are not important. The 355 nm UV laser incident on the trap was split off to a photo-diode (PD) to trigger our acquisition.
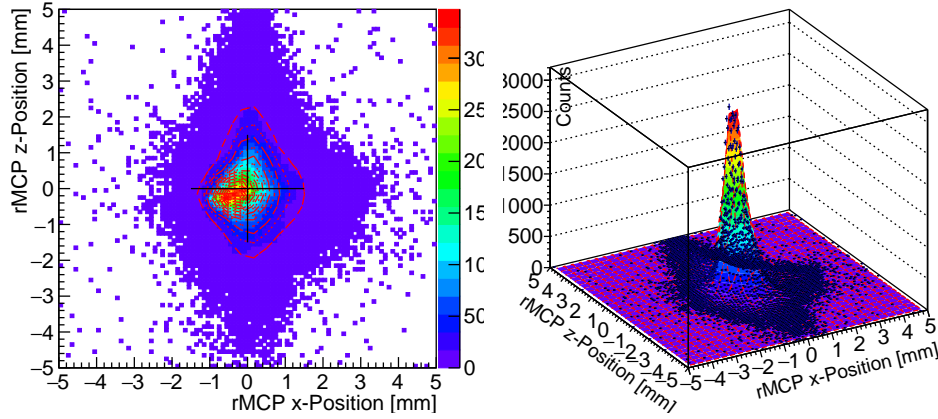
Figure A.2: Drift corrected photo-ion distribution in xz-plane over entire dataset fit with three independent elliptical-Gaussian's parameterizing populations of strongly bound atoms and those in the process of being collected in the trap along the beam-line axis.
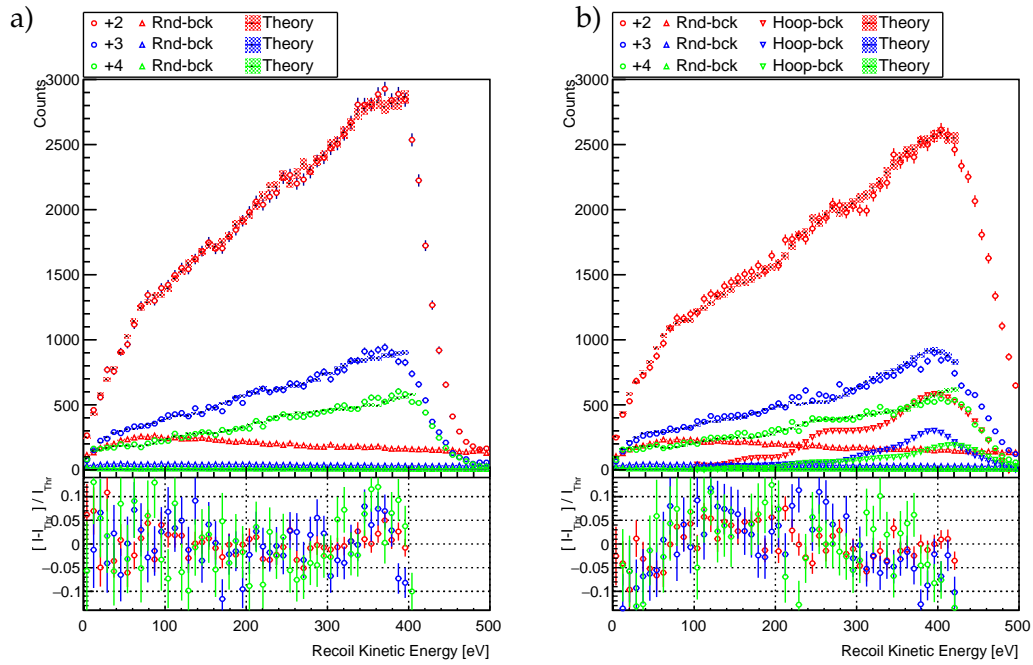

Figure A.3: Recoil K_r spectra for *+2(red), 3(blue), 4(green)* charge states a) before correction from non-uniform $\vec{E}$-field, and b) following ion impact coordinate correction in a uniform $\vec{E}$-field of 998 V/cm. Included are expected random backgrounds and projected hoop backgrounds necessary for $\xi_o/\omega > 0$ model comparison.

Figure A.4: χ^2/dof distribution of equation(4.5) fit to recoil K_r spectra in Figure(4.11) after floating the nuclear matrix element ratio $\xi_o/\omega > 0$ and NORM parameters for *+2, 3, 4* charge states a),b),c) without non-uniform $\vec{E}$-field corrections, and d),e),f) with non-uniform $\vec{E}$-field corrections in mapping $X' \rightarrow X$. Boundaries of these distributions represent 90 % statistical C.L. for the respective charge state. From the large first-forbidden GS branching we assume the beta-energy dependence in the correlation a_1 parameter of equation(2.22).

Figure A.5: Recoil K_r spectra for GS Recoil-SOE-SCINT coincident events in charge state *+2(red), 3(blue), 4(green)* with beta's coincident with the a) upper, and b) lower scintillator. GS events were isolated after applying kinematic bounds, TOF bounds, and gating in *Q*-value on the events within 1.5 MeV of the 8.1 MeV grounds state transition.

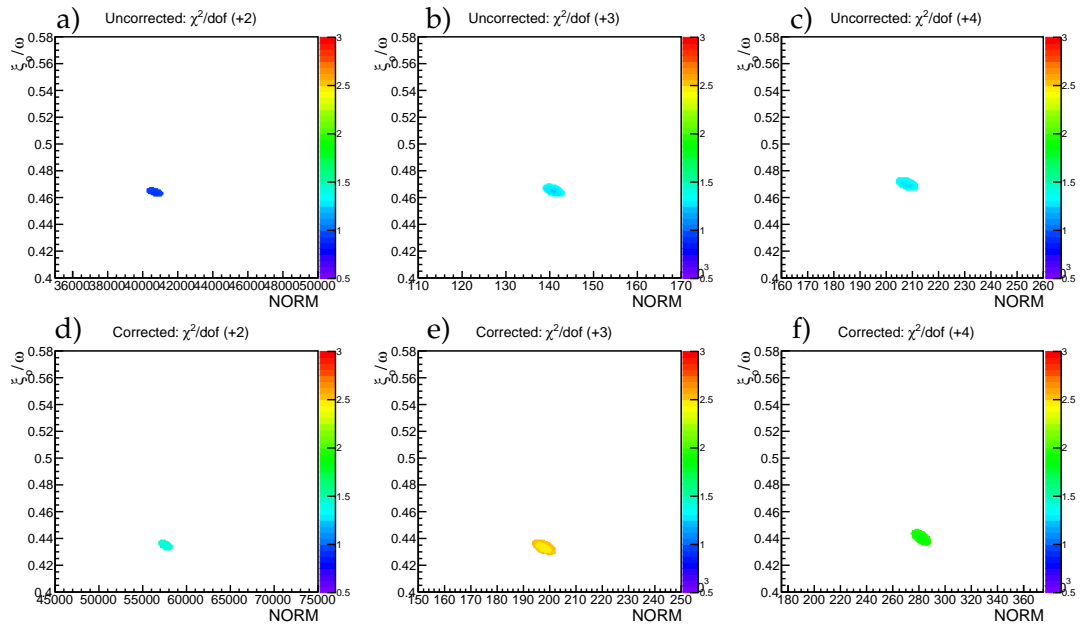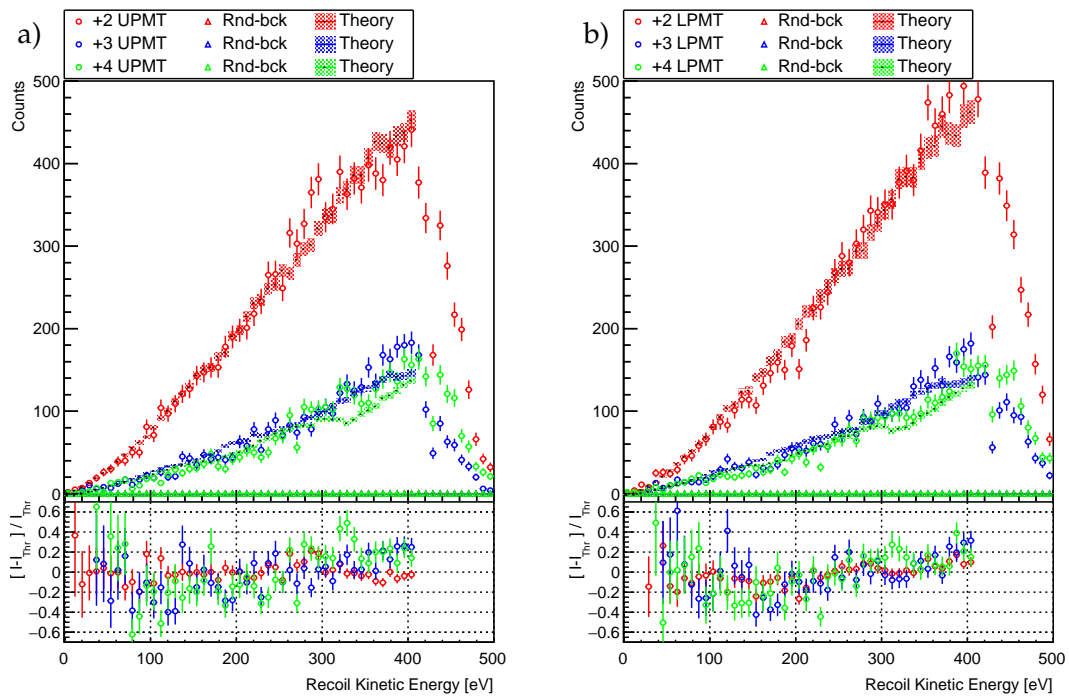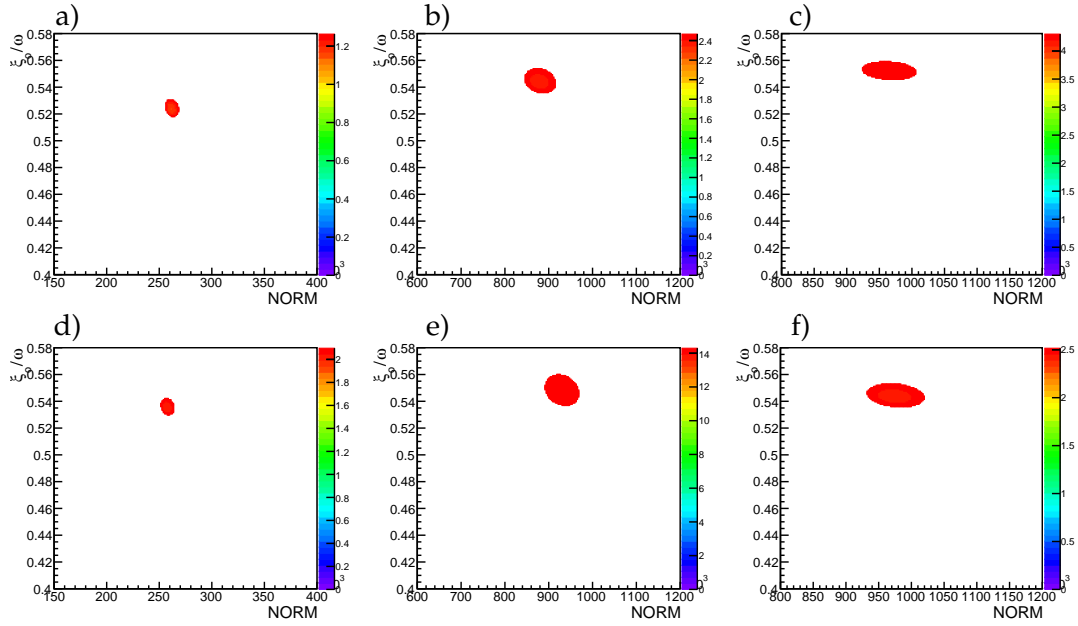**Figure A.6:** χ^2/dof distribution of equation(4.5) fit to recoil GS K_r spectra in Figure(4.18) after floating the nuclear matrix element ratio $\xi_o/\omega > 0$ and NORM parameters for +2, 3, 4 charge states with beta coincident with the a),b),c) Upper, and d),e),f) Lower, scintillators, respectively. Boundaries of these distributions represent 90 % statistical C.L. for the respective charge state. The range in ξ_o/ω was chosen for comparison of results between Recoil-SOE, and Recoil-SOE-SCINT coincidence. The range in ξ_o/ω was chosen for comparison of the Recoil-SOE, and the GS isolated Recoil-SOE-SCINT coincident data to see the large change in ξ_o/ω between these channels.

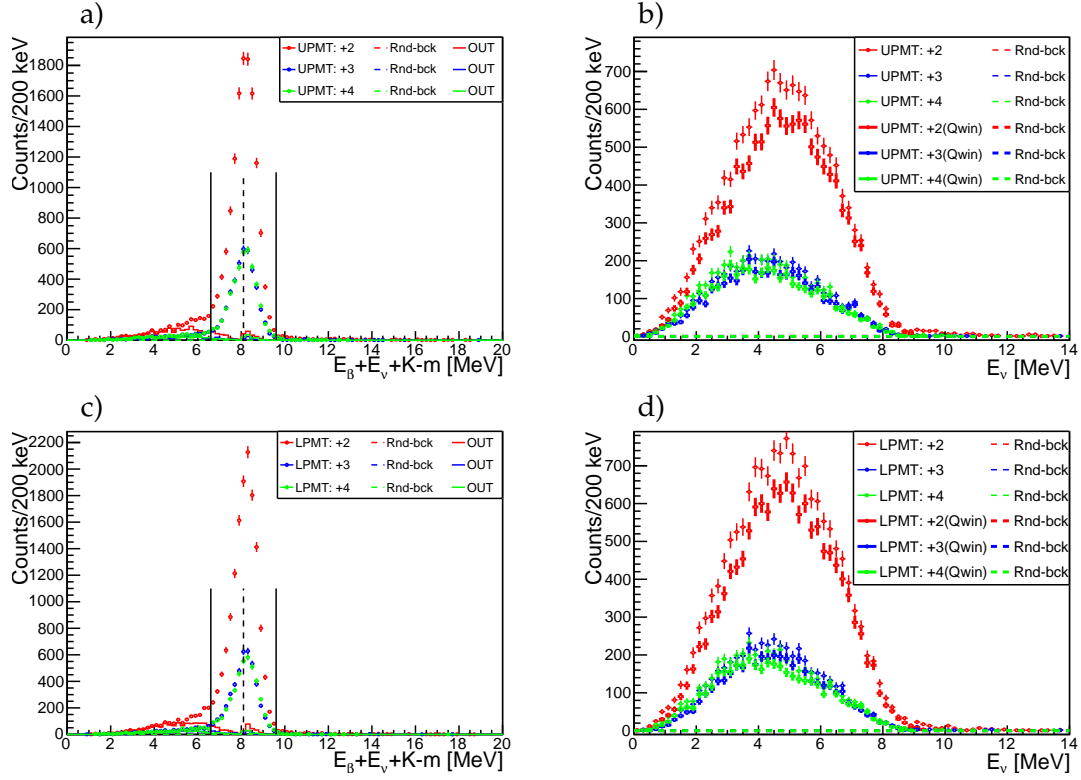**Figure A.7:** Recoil-SOE-SCINT triple coincident events with transition *Q*-value distributions of the *+2(red), 3(blue), 4(green)* charge states with beta's coincident in the a) Upper, and c) Lower scintillators, respectively. Overlaid are the time random coincident background's (dashed-lines), and kinematically forbidden events assuming $Q = 8.1$ MeV (solid-lines) for the respective charge states. Corresponding anti-electron neutrino energy spectra E_ν are shown in b), and d) both with kinematically constrained domain and events within 1.5 MeV of $Q = 8.1$ MeV GS transition (bold-markers), and without such bounds (markers) are shown for each charge state. Expected time random coincident background event distribution without the above bounds are overlaid for each charge state (dashed-lines).

Bibliography

[1] D.A. Dwyer and T.J. Langford. "Spectral Structure of Electron Antineutrinos from Nuclear Reactors". In: *PRL* 114.1 (2015), p. 12502. URL: https://journals.aps.org/prl/abstract/10.1103/PhysRevLett.114.012502 (visited on 03/15/2018).

[2] F.P. An et.al. "Measurement of the Reactor Antineutrino Flux and Spectrum at Daya Bay". In: *PRL* 116.6 (2016), p. 61801. URL: https://journals.aps.org/prl/abstract/10.1103/PhysRevLett.116.061801 (visited on 02/17/2018).

[3] J.K. Ahn et.al. "Observation of Reactor Electron Antineutrinos Disappearance in the RENO Experiment". In: *PRL* 108.19 (2012), p. 191802. URL: https://journals.aps.org/prl/abstract/10.1103/PhysRevLett.108.191802 (visited on 04/15/2018).

[4] Y. Abe et.al. "Indication of Reactor $\bar{\nu}_e$ Disappearance in the Double Chooz Experiment". In: *PRL* 108.13 (2012), p. 131801. URL: https://journals.aps.org/prl/abstract/10.1103/PhysRevLett.108.131801 (visited on 08/09/2019).

[5] P. Huber. "Determination of antineutrino spectra from nuclear reactors". In: *PRC* 84 (2011), p. 024617. URL: https://journals.aps.org/prc/abstract/10.1103/PhysRevC.84.024617 (visited on 04/10/2019).

[6] T.A. Mueller et al. "Improved predictions of reactor antineutrino spectra". In: *PRC* 83 (2011), p. 054615. URL: https://journals.aps.org/prc/abstract/10.1103/PhysRevC.83.054615 (visited on 05/13/2019).

[7] L. Hayen et al. "First-forbidden transitions in reactor antineutrino spectra". In: *PRC* 99.3 (2019), p. 31301. URL: https://journals.aps.org/prc/abstract/10.1103/PhysRevC.99.031301 (visited on 05/25/2019).

[8] A.A. Zakari-Issoufou et.al. "Total Absorption Spectroscopy Study of ^{92}Rb Decay: A Major Contributorto Reactor Antineutrino Spectrum Shape". In: *PRL* 115.10 (2015), p. 102503. URL: https://journals.aps.org/prl/abstract/10.1103/PhysRevLett.115.102503 (visited on 08/21/2018).

[9] B.C. Rasco et.al. "Decays of the Three Top Contributors to the Reactor $\bar{\nu}_e$ High-Energy Spectrum, ^{92}Rb, ^{96gs}Y, and ^{142}Cs, Studied with Total Absorption Spectroscopy". In: *PRL* 117.9 (2016), p. 92501. URL: https://journals.aps.org/prl/abstract/10.1103/PhysRevLett.117.092501 (visited on 02/20/2019).

[10] G. Bak et al. (RENO Collaboration). "Fuel-Composition Dependent Reactor Antineutrino Yield at RENO". In: *PRL* 122.23 (2019), p. 232501. URL: https://journals.aps.org/prl/abstract/10.1103/PhysRevLett.122.232501 (visited on 08/09/2019).

[11] J. Ashenfelter et.al. "First Search for Short-Baseline Neutrino Oscillations at HFIR with PROSPECT". In: *PRL* 121.25 (2018), p. 251802. URL: https://journals.aps.org/prl/abstract/10.1103/PhysRevLett.121.251802 (visited on 02/19/2019).

[12] J. Ashenfelter et.al. "Measurement of the Antineutrino Spectrum from ^{235}U Fission at HFIR with PROSPECT". In: *PRL* 121.25 (2019), p. 251801. URL: https://journals.aps.org/prl/abstract/10.1103/PhysRevLett.121.251801 (visited on 03/02/2019).

[13] E.D. Commins and P.H. Bucksbum. "Weak Interactions of Leptons and Quarks". In: *Cambridge University Press* (1983).

[14] B. Rubio a and W. Gelletly. "Beta Decay of Exotic Nuclei". In: *Lect. Notes Phys.* 764 (2009), pp. 99–151.

[15] O. Kofoed-Hansen. "Theoretical Angular Correlations in Allowed Beta Decay". In: *Dan. Mat. Fys.* 28.9 (1954).

[16] D.H. Wilkinson. "EVALUATION OF BETA-DECAY". In: *Nuclear Instruments and Methods in Physics Research* 290.2-3 (1990), p. 509. URL: https://www.sciencedirect.com/science/article/pii/016890029090570V (visited on 07/22/2017).

[17] E.K. Warburton, D.E. Alburger, and D.H. Wilkinson. "Electron-Neutrino Correlation in First-Forbidden beta decay of ^{11}Be". In: *Phys. Rev. C* 26.3 (1982), p. 7.

[18] E.K. Warburton et al. "First-Forbidden Beta Decay Near A = 40". In: *Annals of Physics* 187 (1988), pp. 471–501.

[19] Behrens and Buhring. "Nuclear Beta Decay". In: *Nuclear Physics* A162 (1971), p. 33.

[20] A.C. Hayes et al. "Systematic Uncertainties in the Analysis of the Reactor Neutrino Anomaly". In: *Phys. Rev. Lett.* 112 (2014), p. 202501.

[21] A. Hayes and P. Vogel. "Reactor Neutrino Spectra". In: *Annu. Rev. Nucl. Part. Sci.* 66 (2016), p. 219.

[22] G. Rudstam et. al. "Reactor Neutrino Spectra". In: *At. Data Nucl. Data Tables* 45 (1990), p. 239.

[23] M. Dombsky, P. Bricault, and V. Hanemaayer. "Increasing beam currents at the TRIUMF-ISAC Facility; techniques and experiences". In: *Nucl. Phys. A* 746 (2004), pp. 32–39. URL: https://www.sciencedirect.com/science/article/abs/pii/S0375947404009534 (visited on 10/01/2019).

[24] D. Melconian et al. "Release of ^{37}K from catcher foils". In: *NIM* A538 (2005), pp. 93–99.

[25] T.B. Swanson et al. "Efficient transfer in a double magneto-optical trap system". In: *J. Opt. Soc. Am. B* 15.11 (1998), pp. 2641–2645. URL: https://www.osapublishing.org/josab/abstract.cfm?uri=josab-15-11-2641 (visited on 09/15/2019).

[26] N.D. Scielzo et.al. K. Siegl. "Recoil ions from the β decay of ^{134}Sb confined in a Paul trap". In: *PRC* 97.3 (2018), p. 35504. URL: https://journals.aps.org/prl/abstract/10.1103/PhysRevC.97.035504 (visited on 01/05/2019).